Tokyo Institute of Technology

Practical Control of Leadscrew Mechanism for Ultra-Precision Positioning

Master Thesis

Department of Mechano-Micro Engineering

Supervisor: Associate Professor Dr. Kaiji Sato
Guilherme Jorge Maeda, 05M34307

2007

CONTENTS

CHAPTER 1 - INTRODUCTION

Precision positioning systems achieving accuracy of micrometric and nanometric order are essential in the optical, semiconductor, and nanotechnology industry. These positioning systems usually have one or more elements that present friction, like motors with brushes and/or bearings with mechanical contact. Friction is well known to cause steady-state error, tracking error, limit cycles and to slow the mechanism motion. Thus, it is important to consider friction compensation in the controller design. However, controller design of mechanisms with friction tends to be difficult because: (1) characteristics of mechanisms with friction are nonlinear, thus simple controllers like PID controllers do not offer the best as possible performance, and (2) friction compensation usually requires the identification of friction characteristics, which varies often.

In order to compensate for friction, efforts have been done toward the understanding of friction effects in the control performance [1] and its dynamics [2,3]. Control systems for precision/ultra-precision positioning must compensate for friction in microdynamics, which requires the understanding of the nonlinear behavior of the mechanism before the breakaway torque [4-6]. Nevertheless, friction parameters, especially in the microdynamic regime, tend to change according to time and position [7,8] and seem to behave stochastically [5], being difficult to predict exactly. Also, a complete model for macro-microdynamics has to address the transition between the two dynamics [9]. The inclusion of the friction dynamics as part of the control law do improve precision positioning [8,10-12]; but the controller design becomes time-demanding and difficult.

Besides friction, another characteristic of positioning systems which deteriorate the performance is vibration. Vibrations in positioning mechanism may arise from low stiffness connections among components, and lower the positioning accuracy. In this research, vibration is observed on the mechanism when the payload is increased, making the mechanism to behave as a two-mass mechanism. It is important to consider payload variations in positioning mechanisms. This is because in practical applications, positioning mechanisms are often used with different workpiece masses. Moreover, in order to obtain multiple degree-of-freedom motion – like XY tables – linear motion

mechanisms are stacked. As it will be shown, the variation of mass not only changes friction but also gives rise to vibration.

For the solution of vibration, the use of notch filters is common and effective when the vibration frequency is constant and well known (e.g. when the vibration is caused by electrical supply line noise or when the parameters of the mechanism do not change). However, positioning mechanisms are often used with different payloads, which changes the frequency of residual vibration; thus requiring adaptive algorithms [13] Adaptive algorithms decrease the practicality of the design method. Another approach to reduce residual vibration is based on input shaping techniques. Input shaping is noticeably applied for vibration reduction in disk drive servos [14], robot arms [15] and linear positioning mechanisms [16]. Of all the input shaping techniques, perhaps the impulse input sequences is the most widely used, due to its practical and robust characteristics. However, robustness to large resonant frequency variations also extends motion time on the order of one cycle of vibration [17].

In order to achieve ultra-precision positioning, the controller must compensate the effects of friction and eliminate vibration. However, fast speed during point-to-point (PTP) positioning must be also considered. In industrial applications, fast positioning systems reduce the processing time, increasing production output and reducing manufacturing cost. Therefore, fast PTP is the next improvement to be considered in an ultra-precision positioning controller.

Another important feature of positioning systems is high performance when following a continuous path. Continuous motion control is important in positioning systems because it determines the profile accuracy of the workpiece being machined. In this research, continuous motion control is also considered.

1.1. PREVIOUS STUDIES WITH THE NCTF CONTROL AND PURPOSES OF THIS RESEARCH

In this research, a conventional leadscrew mechanism is used as the mechanism with friction. Although some researches have achieved nanometric accuracy with a leadscrew system (e.g. [11,12,18,19]), this research differs significantly in ease of design and control structure. The controller in use, named NCTF controller, has a simple

structure and its design method does not require exact parameter identification; being easy to design, understand, and adjust.

Up to now, using different mechanisms, the NCTF control system has been designed, evaluated and compared with another types of practical controllers. With a rotary mechanism, the influence of the NCTF controller parameters and the actuator saturation were discussed in [20]. In [21,22], performance improvement by means of antiwindup integrator was presented. The performance of the NCTF controller was compared to those delivered by conventional PID's [20,23]. The NCTF controller performance was also compared to another two practical controllers which address friction compensation: a PD controller with a nonlinear proportional feedback compensator, and a PD controller with a smooth nonlinear feedback compensator [24,25]. Sato et al. [26] designed and compared the performance of the NCTF controller with that of a PID controller, using a linear motor mechanism. The mechanism is driven by a voice coil motor and has an adjustable-preload linear ball guide. Positioning accuracy better than 50 nm was achieved. A solution for residual vibration based on the NCTF control was proposed in [27] using a rotary mechanism. The proposed solution seems to be suitable when the bandwidth of the control system is higher than the frequency of vibration. As it will be shown, in the case of the leadscrew mechanism, the bandwidth of the NCTF control system is lower than the frequency of vibration, thus requiring a new solution.

The purpose of this research is to clarify the NCTF control method of a leadscrew mechanism for ultra-precision positioning. The control design method must be easy and straightforward. Also, positioning accuracy and resolution are expected to be better than 10 nm.

There are mainly four goals proposed and achieved in this research:

1. To apply the NCTF controller design method using the leadscrew mechanism under a light payload condition. Ultra-precision positioning is expected.
2. To improve the NCTF controller by finding a solution for the elimination of vibration caused by a heavy payload condition.
3. To improve the speed of PTP positioning.
4. To propose the NCTF controller for continuous motion control and evaluate its performance.

1.2. SUMMARY OF THIS THESIS

This thesis is organized as follows:

Chapter 2: the experimental setup and its dynamic model are introduced.

Chapter 3: the NCTF controller design is explained, including the derivation of the design parameters and analyses of the linear and practical stability limits. An antiwindup integrator is introduced. The NCTF controller is designed under the lightweight condition and ultra-precision positioning performance is evaluated.

Chapter 4: the NCTF controller designed in Chapter 3 is evaluated with the mechanism under a heavyweight condition. The heavy payload leads to residual vibration and a practical solution for vibration is proposed and evaluated.

Chapter 5: the NCTF controller design method is modified so that the response characteristic for PTP positioning is improved.

Chapter 6: this chapter proposes a modification of the NCTF controller so that precision continuous motion becomes possible. The proposed controller is then compared to the original NCTF controller and a PI-D controller.

Chapter 7: the proposed controller design procedure in Chapter 3 is examined under mechanisms whose viscous and Coulomb friction values vary largely. Also, the NCT controller is designed under different NCT's inclinations. The results prove that the design procedure of the NCTF controller is usable in the referred cases.

Chapter 8: the modifications and methods proposed in this research are discussed in relation to their results. Also, recommendations for the future works concerning the NCTF control and the leadscrew mechanism are made.

CHAPTER 2 - EXPERIMENTAL SETUP AND DYNAMIC MODEL

Figure 2-1 shows a picture of the leadscrew mechanisms under different payload conditions. The two mechanisms are controlled in this study. The mechanism under the heavyweight condition is referred as the X axis mechanism. The mechanism under the lightweight condition is referred as the Y axis mechanism.

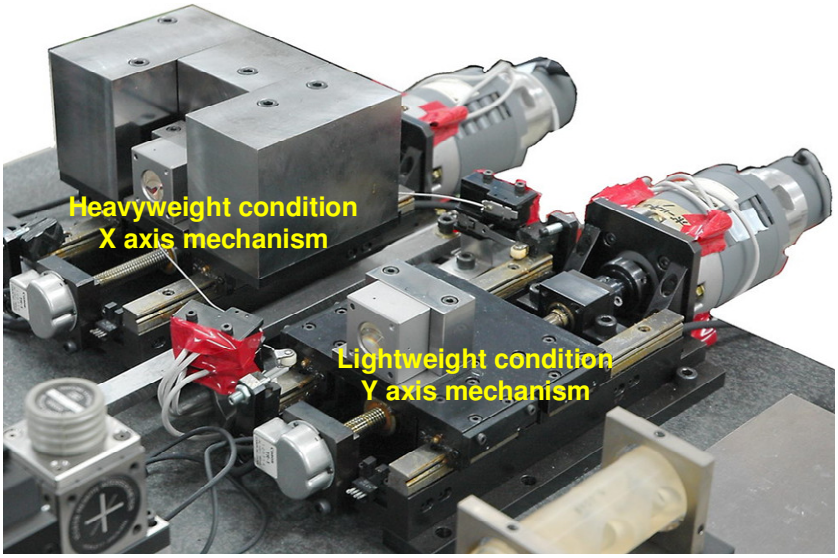

Figure 2-1. Photograph of the leadscrew mechanism.

Figure 2-2 shows a schematic representation of the experimental control system setup. The controller sampling frequency is 5 kHz and feedback position is given by a laser position sensor with resolution of 1.24 nm (Agilent: 10897B). The PWM amplifiers (Copley: 4122Z) are limited at 45 V/6 A by the power supply. The DC motors (Yaskawa: UGTMEM-06LB40E) have a back EMF constant of 0.086 Vs/rad. The maximum travel ranges of the tables are 55 mm.

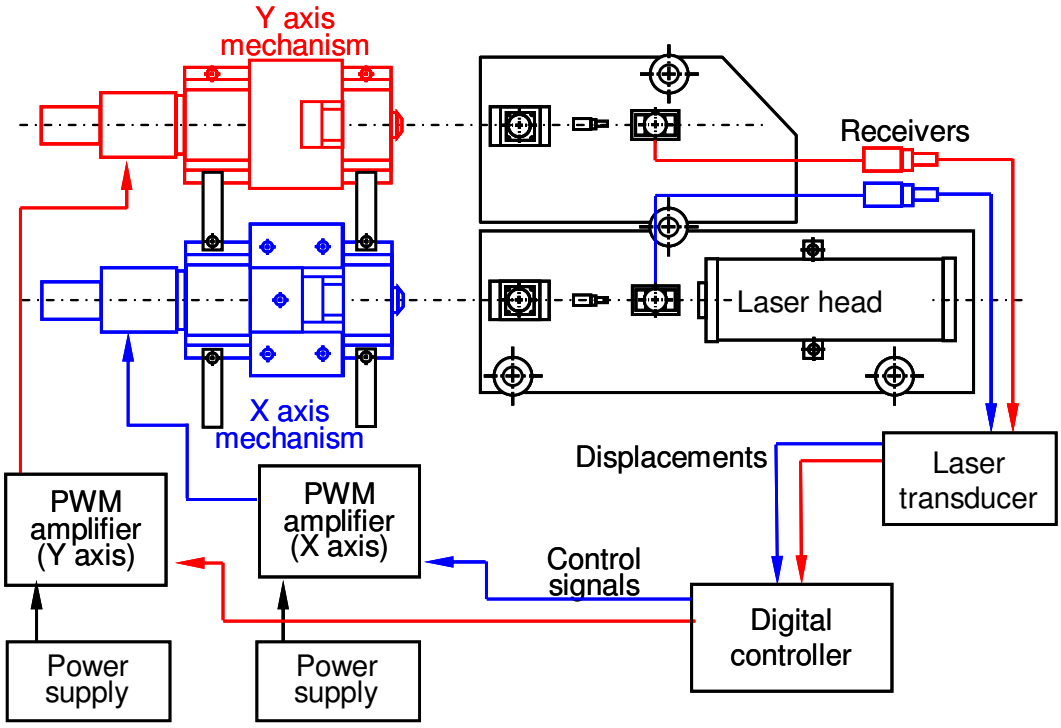

Figure 2-2. Schematic representation of the experimental setup.

Figure 2-3(a) shows the structure of the mechanism under the two payload conditions. The mechanism has several sources of friction: the DC motor, the preloaded double-nut, the linear ball guides, and the ball bearings supporting the screw shaft. The overall combination of the nonlinear friction effects are modeled as the frictional torque T_{fric} shown in Figure 2-3(b). The stiffness of the connection between the screw and the nut is represented as the spring K_n. The vibration between the screw and nut is damped by a damper of coefficient C_n. Under the heavyweight condition (X axis mechanism), the referred connection does not rigidly support the payload on the table, and, as it will be shown in Chapter 4, residual vibration is observed. The X axis mechanism has vibration characteristics of a two-mass mechanism. Table 2-1 shows the parameter values of the model for the X and Y axis mechanism.

Table 2-1. Model parameters

Symbol	Description	Value
J	Moment of inertia	1.81 X 10^{-4} kg·m^2
K_m	Torque constant of the motor	0.172 Nm/A
T_{fric}	Nonlinear friction	-
T_{app}	Applied torque to the leadscrew	-
	X axis mechanism	
M_x	Mass of the table	17.50 kg
T_{fxmax}	Maximum friction	0.090 Nm
C_{sdx}	Viscous friction	0.00100 Nms/rad
K_{nx}	Screw-nut spring constant	4.5 X 10^7 Nm
C_{nx}	Screw-nut damping coefficient	2300 Ns/m
	Y axis mechanism	
M_y	Mass of the table	3.57 kg
T_{fymax}	Maximum friction	0.046 Nm
C_{sdy}	Viscous friction	0.00097 Nms/rad
K_{ny}	Screw-nut spring constant	8.3 X 10^5 Nm
C_{ny}	Screw-nut damping coefficient	1700 Ns/m

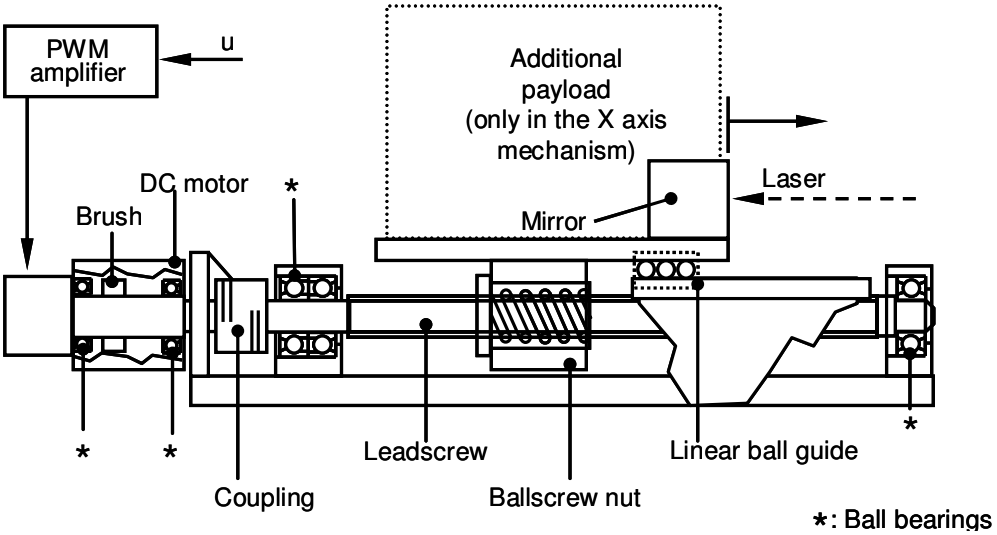

(a) Structure of the mechanism

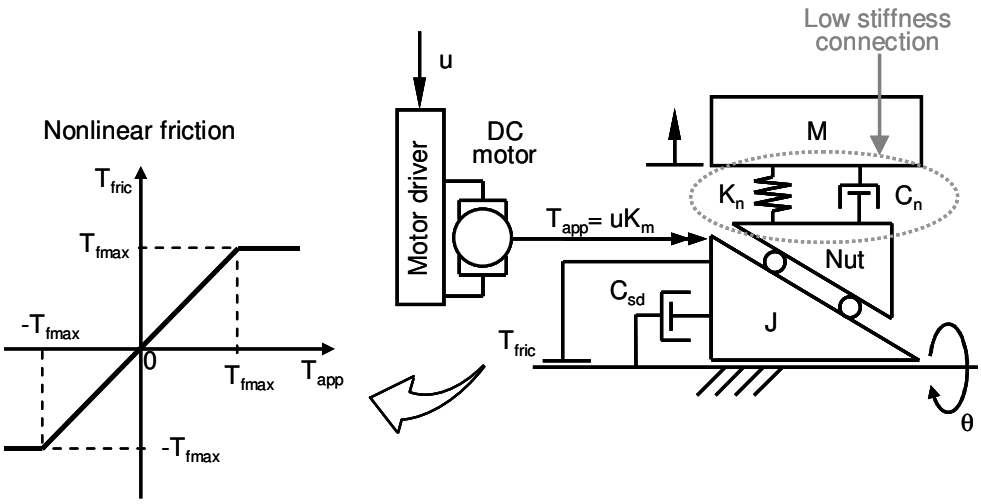

(b) Dynamic model

Figure 2-3. Structure and dynamic model of the leadscrew mechanism.

Figure 2-4 shows the dynamic model in Figure 2-3 implemented in Simulink software for simulations. The transfer function Ω(s) represents the dynamics of the rotating parts and includes the nonlinear friction model in Figure 2-3(b). The transfer function V(s) represents the dynamics of the linear motion. Notice that the dynamics represented by the model addresses the nonlinear macrodynamics of the mechanism, but does not address the microdynamics behavior.

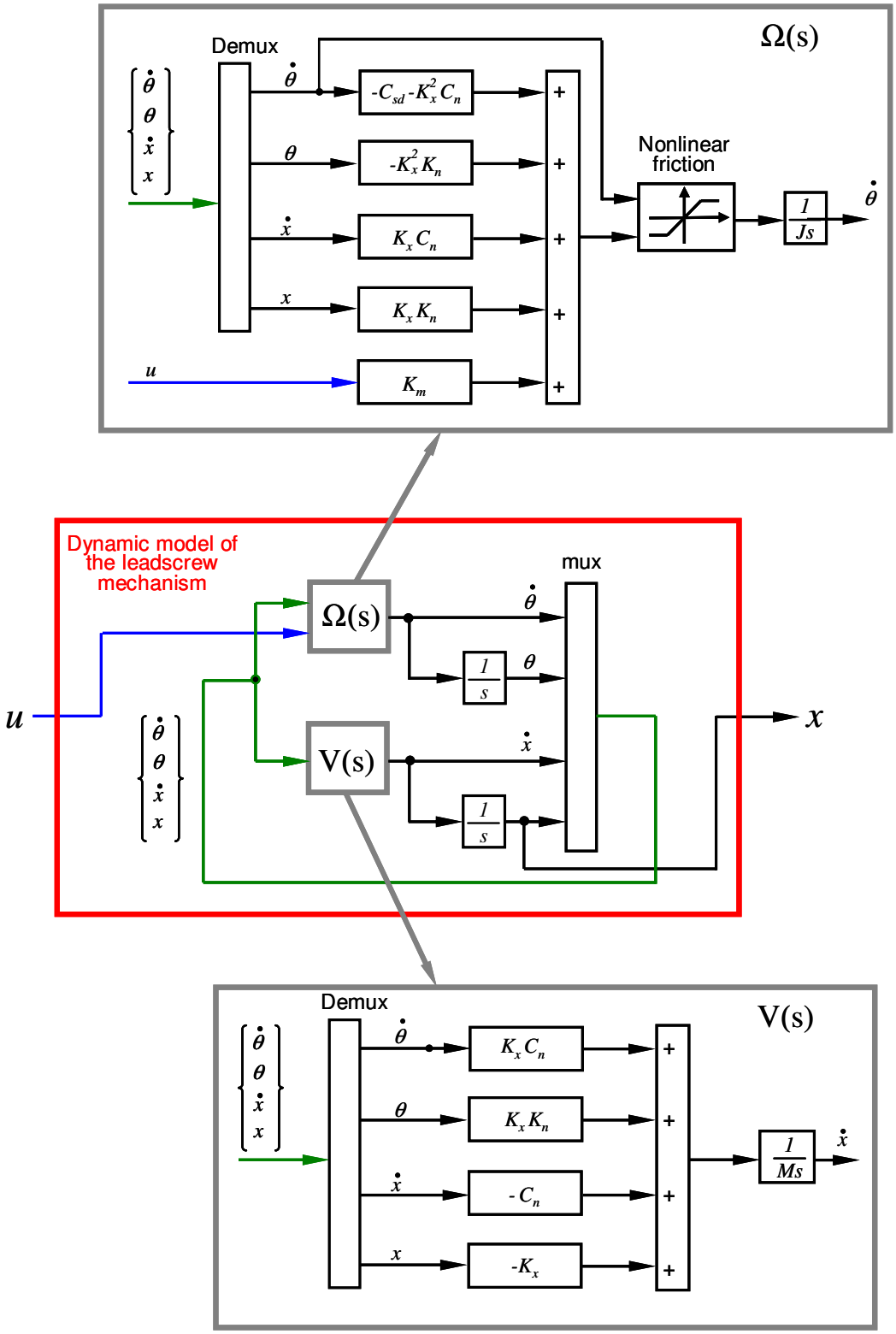

Figure 2-4. Dynamic model of the mechanism implemented in Simulink software.

CHAPTER 3 - NCTF CONTROL UNDER THE LIGHTWEIGHT CONDITION

3.1. NCTF CONTROLLER DESIGN FOR MECHANISMS WITH FRICTION

Figure 3-1 shows the structure of the NCTF control system. The controller is composed of a nominal characteristic trajectory (NCT) and a PI compensator. The objective of the PI compensator is to make the mechanism motion following the NCT trajectory, finishing at the origin of the phase-plane. The output of the NCT is a signal u_p, which is the difference between the actual error rate of the mechanism ($-\dot{x}$) and the error rate of the NCT. On the phase-plane, the table motion is divided into a reaching phase and a following phase. During the reaching phase, the compensator controls the table motion to reach the NCT trajectory. Then the following phase starts, and the PI compensator makes the mechanism motion following the NCT, leading it to the origin of the phase-plane.

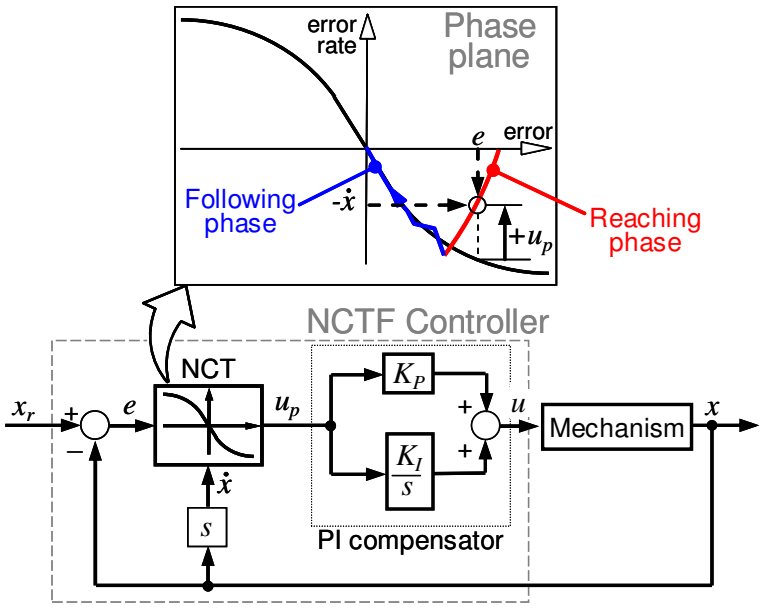

Figure 3-1. Structure of the NCTF control system.

The design of the NCTF controller comprises three steps:

1. The mechanism is driven with an open-loop step input while its displacement and velocity are measured
2. The NCT is constructed on the phase-plane by using the displacement and velocity of the mechanism during the deceleration
3. The PI compensator is designed using the open-loop response and the NCT information.

Since the NCT is constructed from the actual response of the mechanism, the actual nonlinear friction effects are included in the NCT. Thus, the actual friction characteristic is part of the control law.

3.1.1 Open-Loop Experiment and NCT Construction

Figure 3-2(a) shows the open-loop response used to construct the NCT. The Y axis mechanism (lightweight condition) is driven in order to achieve the maximum velocity within the 55 mm stroke limit. The open-loop input was set to an amplitude u_r = 5 A (83% of the actuator saturation) and duration t_r = 0.3 s, leading to a displacement of 48.5 mm.

Figure 3-2(b) shows the NCT constructed from the open-loop experiment. The vertical axis (Error rate ($\dot{e}$)) is constructed from the measured velocity during the deceleration. The horizontal axis (Error e) is constructed from the measured displacement during the deceleration. The detail shows that the spring-like behavior appears near the origin of the NCT as a circling motion. This circling motion has negative effects in positioning and should be eliminated [26,28]. In order to do so, the NCT is linearized with a straight line close to the origin. The inclination of the line is chosen to be the same as the tangential line of the NCT just before the spring-like behavior starts showing. Thus, the experimental results yield an inclination of $m = -505$ s^{-1}. The limits of the NCT, are extrapolated with horizontal lines.

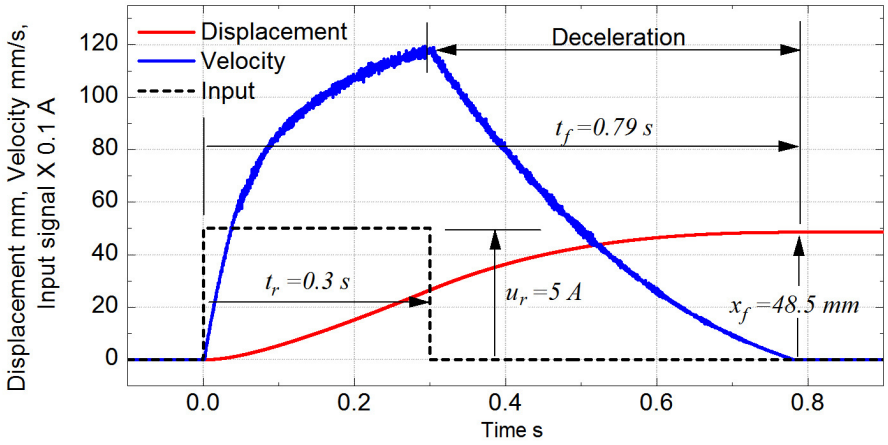

(a) Open-loop response

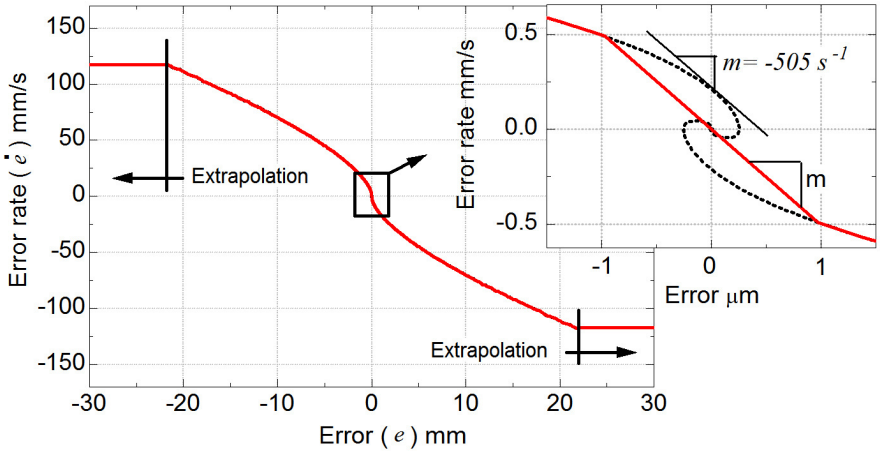

(b) NCT constructed from the open-loop response

Figure 3-2. Open-loop response and construction of the NCT using the mechanism under the lightweight condition.

3.1.2 Open-Loop Response and Simplified Object Parameters

The derivation of the NCTF controller parameters are based on a linear macrodynamic model, named simplified object model. The parameters of the model, named simplified object parameters, are determined from the open-loop experiment and the NCT construction. It is assumed that the mechanism comprises a damped mass and a DC or an AC servo motor. This generic configuration is the same as those of a large number of positioning mechanisms used in industry. The dynamic model of the mechanism is given as

$$M\ddot{x} + c\dot{x} = K_{motor}u \tag{3-1}$$

where M is the mass, c is the damping coefficient, and K_{motor} is the force constant of the motor. Considering $\alpha = c/M$ and $K\alpha = K_{motor}/M$, Eq. (3-1) is rewritten as

$$\ddot{x} + \alpha\dot{x} = K\alpha u \tag{3-2}$$

which leads to the transfer function of the simplified object model

$$\frac{X}{U} = K\frac{\alpha}{s(s+\alpha)} \tag{3-3}$$

The inclination of the NCT near the origin *(m)* is constructed when the input to the mechanism is zero, which is represented by Eq. (3-2) as

$$\ddot{x} + \alpha\dot{x} = 0 \quad \rightarrow \quad \frac{\mathrm{d}\dot{x}}{\mathrm{d}x} = -\alpha \tag{3-4}$$

Considering point-to-point positioning, the derivative of the reference is zero so that $e = x_r - x$ becomes $\dot{e} = -\dot{x}$ and Eq. (3-4) is rewritten as

$$\frac{\mathrm{d}\dot{e}}{\mathrm{d}e} = -\alpha \tag{3-5}$$

The left term in the previous equation also represents the inclination of the NCT close to the origin *m* in Figure 3-2 (b). Thus

$$\alpha = -m \tag{3-6}$$

The parameter K is found by integrating Eq. (3-2) from $0 \le t \le t_f$, where t_f is the time in which the mechanism stops

$$x_f = K\int_0^{t_f} u\mathrm{d}t$$

Since the value of u is constant with amplitude u_r, and zero after t_r (see Figure 3-2 (a)), the previous integral becomes

$$x_f = Ku_r t_f \quad \rightarrow \quad K = \frac{x_f}{u_r t_f} \tag{3-7}$$

In the case of the leadscrew mechanism, using the information from the open-loop experiment of Figure 3-2(a) and Eq. (3-7)

$$K = \frac{48.5}{5 \times 0.3} = 32.3 \text{ mm/As} \tag{3-8}$$

Thus, the actual mechanism is expressed by two simplified object parameters, K and α which are identified by the open-loop step response and the NCT inclination. In the case of the Y axis mechanism, K = 32.3 mm/As and α = 505 s^{-1}.

3.1.3 Compensator Parameters

Figure 3-3 shows the block diagram of the continuous closed-loop NCTF control system with the simplified object model near the NCT origin (where the NCT is linear and has an inclination $\alpha = -m$).

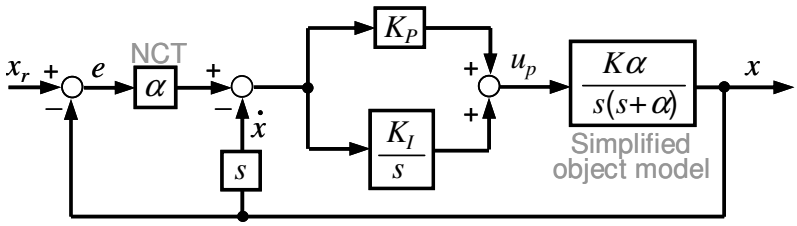

Figure 3-3. NCTF control system with the simplified object model.

Defining:

$$2\zeta\omega_n = \alpha K K_P \tag{3-9a}$$

$$\omega_n^2 = \alpha K K_I \tag{3-9b}$$

The closed-loop transfer function of the system shown in Figure 3-3 is

$$\frac{X}{X_r} = \left(\frac{\alpha}{s+\alpha}\right)\left(\frac{2\zeta\omega_n s + \omega_n^2}{s^2 + 2\zeta\omega_n s + \omega_n^2}\right) \tag{3-10}$$

The proportional and integral compensator gains are calculated from the definitions in Eq. (3-9), as

$$K_P = \frac{2\zeta\omega_n}{\alpha K} \tag{3-11a}$$

$$K_I = \frac{\omega_n^2}{\alpha K} \tag{3-11b}$$

For the choice of ζ and ω_n, the designer must consider the stability of the control system.

3.1.4 Stability Analysis

Linear stability limit

From Eq. (3-10), it is seen that the continuous control system is always stable. Regarding the digital system, a linear stability analysis is carried out with the sampled-data system shown in Figure 3-4. The compensator includes one sampling controller delay. The mechanism motion is assumed to be inside the linear range of the NCT.

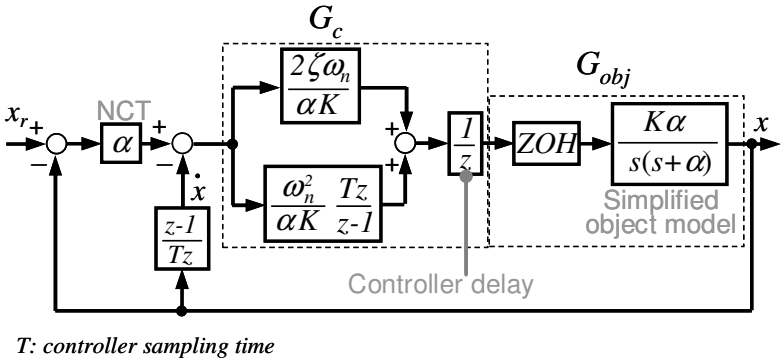

Figure 3-4. Sampled-data system used for a linear stability analysis.

The sampled transfer function of G_{obj} is readily available in the literature [29, p. 795] and given as

$$G_{obj}(z) = \beta\frac{K}{\alpha}\left[\frac{z+b}{(z+1)\left(z-\mathrm{e}^{-\alpha T}\right)}\right] \tag{3-12}$$

where:

$$\beta = \alpha T - 1 + \mathrm{e}^{-\alpha T}$$
$$b = \frac{1 - \mathrm{e}^{-\alpha T} - \alpha T \mathrm{e}^{-\alpha T}}{\beta}$$

The digital closed-loop transfer function $G_{NCTF}(z)$ is T_{fmax} / K_x whose expanded form is

$$\begin{aligned} G_{NCTF}(z) = & \\ = & \frac{\alpha T \beta \left(\mu_1 z^3 + \mu_2 z^2 + \mu_3 z \right)}{} \\ & + (\alpha T)^2 z^5 \\ & - (\alpha T)^2 \left(2 + \mathrm{e}^{-\alpha T} \right) z^4 \\ & + \left[(\alpha T + 1) \beta \mu_1 + (\alpha T)^2 \left(1 + 2\mathrm{e}^{-\alpha T} \right) \right] z^3 \\ & + \left[-\beta \mu_1 + (\alpha T + 1) \beta \mu_2 - (\alpha T)^2 \mathrm{e}^{-\alpha T} \right] z^2 \\ & + \left[-\beta \mu_2 + (\alpha T + 1) \beta \mu_3 \right] z \\ & - \beta \mu_3 \end{aligned} \qquad (3\text{-}13)$$

where:

$$\mu_1 = \omega_n T \left(2\zeta + \omega_n T \right)$$
$$\mu_2 = \omega_n T \left[(2\zeta + \omega_n T) b - 2\zeta \right]$$
$$\mu_3 = -2\zeta \omega_n T b$$

Eq. (3-13) shows that the stability of the linear digital NCTF control system is dependent of the parameters αT, $\omega_n T$, and ζ. Applying the Jury's test [29, p. 35] to Eq. (3-13), a numerical plot of the stability limit is shown in Figure 3-5(a). Figure 3-5(b) shows the case in which the stability analysis is made with the integral gain set to zero. Comparing both surfaces, it is observed that the integral gain has little effect in the linear digital stability analysis. The linear stability limit has negligible variations in the αT axis.

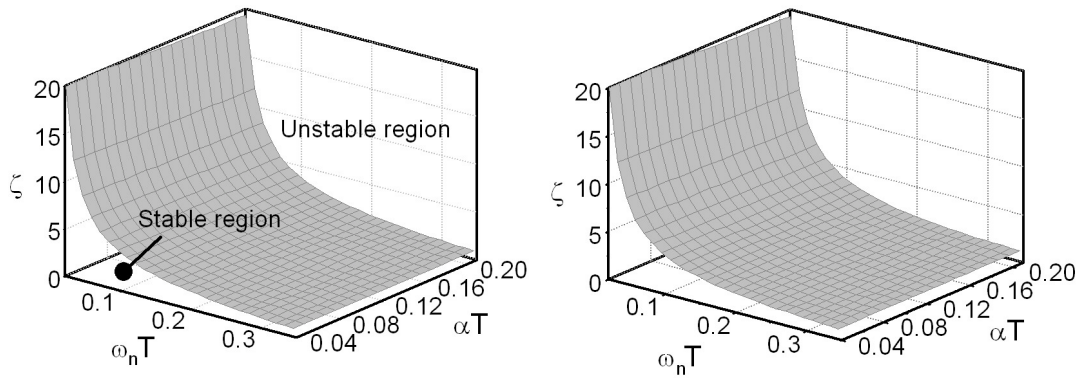

(a) Stability limit of the linear digital system with integral element

(b) Stability limit of the linear digital system without integral element

Figure 3-5. Linear stability limit of the linear digital system by the Jury's test.

Practical stability limit

In the previous analysis, the stability of the control system was based on the simplified object model which is linear; thus the analysis neglects nonlinear effects like Coulomb friction. However, the Coulomb friction is known to increase the stability of the system [1], allowing the use of higher gains than the ones predicted by a linear analysis. This section introduces a simple method to find the practical stability limit of the NCTF control system.

From Figure 3-5, it is observed that the integral element has negligible influence on the stability of the linear system. For the following analysis, it will also be assumed that the integral element has negligible influence on the stability of the actual system. Experiments and simulations will show that this assumption is valid.

The practical stability limit is found by driving the mechanism with the NCTF controller using only the proportional gain. The proportional gain is increased until continuous oscillations start showing. The determined proportional gain is named as K_{Pu}, which stands for the actual ultimate proportional gain (K_{Pu}= 2.4 As/mm in the case of the leadscrew mechanism). Using Eq. (3-11a), the practical stability limit – referred as ζ_{prac} – is given as

$$\zeta_{prac} = K_{Pu}\left(\frac{\alpha K}{2\omega_n}\right) \qquad (3\text{-}14)$$

Eq. (3-14) represents the maximum values allowed for the choice of ζ, before the control system becomes unstable. In the case of the Y axis mechanism, Eq. (3-14) becomes:

$$\zeta_{prac} = 2.4\left(\frac{505\times 32.3}{2\omega_n}\right) \qquad (3\text{-}15)$$

In order to prove the suitability of ζ_{prac}, the NCTF controller (using the proportional and integral gains), is designed as follows: for a fixed value of $\omega_n T_k$ (where k = 1...7), the compensator gains are calculated from Eq. (3-11). The parameter ζ_k is increased until the system achieves instability. The points defined by ζ_k and $\omega_n T_k$ are plotted in Figure 3-6. The procedure is made experimentally and by simulations using the model of the mechanism in Figure 2-3(b). As the results show, ζ_{prac} fits closely all the points representing the NCTF control stability limit. In addition, it is observed that ζ_k represented by the linear stability limit curve is much smaller than ζ by the practical stability limit.

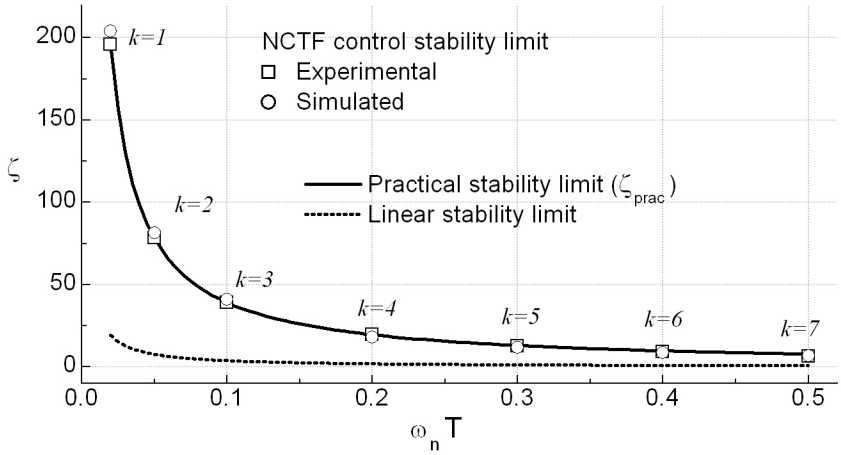

Figure 3-6. Practical stability limit (ζ_{prac}) compared to experimental and simulated results.

3.1.5 Choice of the Design Parameters $\omega_n T$ and ζ

Figure 3-7 shows three different compensators A, B and C and their respective gains. The three compensators are chosen to have 40 % of the values of ζ_{prac} calculated from Eq. (3-15), so that the margin of safety of the design is 60 %.

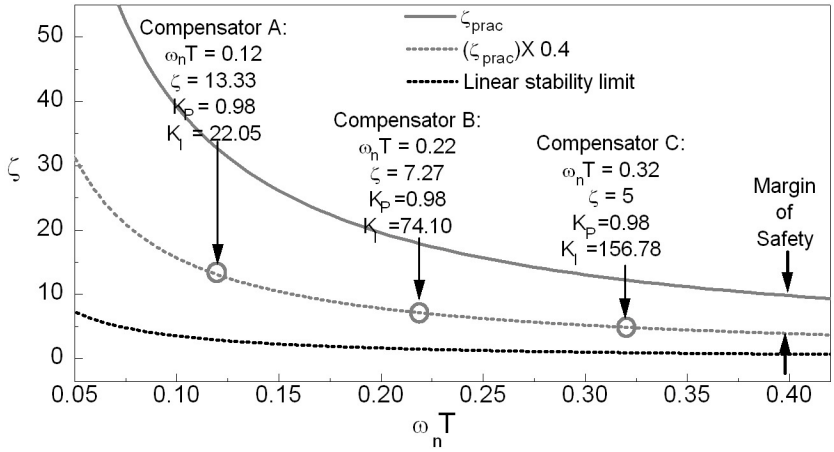

Figure 3-7. Three different compensators respecting a margin of safety of 60 %.

Figure 3-8 shows that the positioning resolution improves as $\omega_n T$ increases. Since the compensator C produces the best performance, it is chosen as the final controller for performance evaluation.

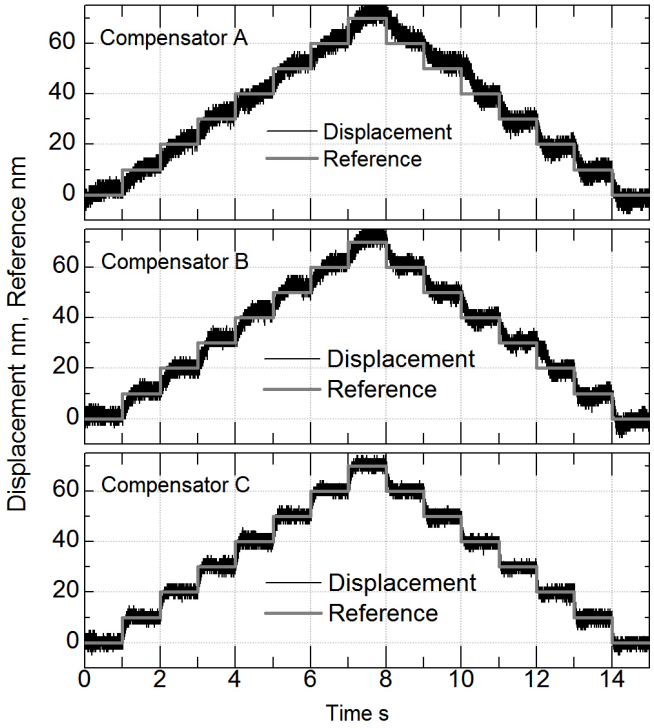

Figure 3-8. Response of the compensators A, B, and C for a 10 nm stepwise input.

During the choice of the design parameters, the designer may be tempted to use large values of $\omega_n T$ in order to improve the performance. However, from Eq. (3-11) it is observed that as $\omega_n T$ increases, K_I increases exponentially while K_P is kept constant. Excessive large values of $\omega_n T$ will cause the controller to behave as a pure integral controller, which may lead to instability. Therefore, the choice of $\omega_n T$ should start from small values to large ones, but never the opposite.

3.1.6 Controller Design Procedure

As a practical design method, the NCTF controller design procedure is accomplished by the few following steps:

1. From the open-loop experiment, the NCT trajectory is constructed and linearized close to the origin, with an inclination m.
2. The parameters α (from Eq.(3-6)) and K (from Eq.(3-7)) are obtained.
3. The mechanism is driven with the NCTF controller using only the proportional gain. The proportional gain is increased in order to determine the ultimate proportional gain (K_{Pu}).
4. The practical stability limit (ζ_{prac}) is obtained by using K_{Pu} with Eq. (3-14).
5. The design parameters $\omega_n T$ and ζ are chosen within the stable region delimited by ζ_{prac}.
6. The PI compensator gains are calculated by using the parameters $\omega_n T$ and ζ with Eq. (3-11).

Notice that the procedure is completed regardless any information about model parameters already known.

3.2. IMPROVING THE PERFORMANCE WITH AN ANTIWINDUP INTEGRATOR

The use of high integral gain is a key factor to improve positioning resolution. However, the integral gain also causes undesirable overshoot during step input responses because of the integrator windup effect. Thus, antiwindup integrators are useful to improve the performance. Up to now antiwindup integrators with the NCTF controller were applied to a rotary positioning system: a tracking antiwindup [21] and a conditionally freeze integrator [22]. Both methods are proven to improve robustness. Although the tracking antiwindup method has only one design parameter, there are no clear rules on how to determine a proper parameter value, except for rules of thumb. The conditionally freeze integrator rule requires only the maximum control output signal as a design parameter, which is easy to determine. Due to the ease of implementation, in this research, the conditionally freeze integrator [22] is used. The antiwindup element controls the input of the integrator as shown in Figure 3-9 with the following rule:

$$\Delta u_i = \begin{cases} 0, & \text{if } |u_o + u_i| > u_s \text{ and } e \cdot u_i \geq 0 \\ e, & \text{otherwise} \end{cases} \qquad (3\text{-}16)$$

where u_o is the proportional control signal, u_i is the integrated control signal, $\triangle u_i$ is the change rate of u_i, and u_s is the maximum value of the control signal.

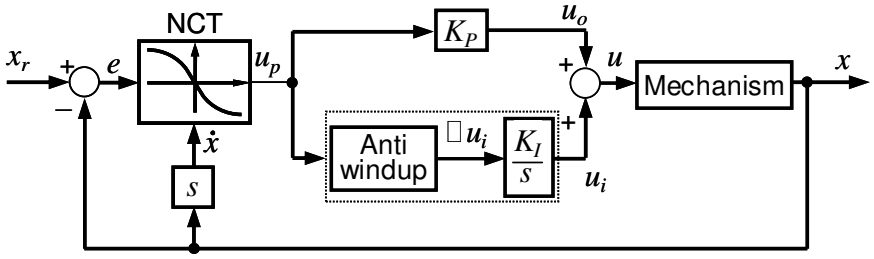

Figure 3-9. NCTF controller structure with the conditionally freeze antiwindup.

The maximum output control signal (which defines the saturation of the actuator) of the leadscrew mechanism is 6 A. The effect of the antiwindup on positioning performance is shown in Figure 3-10, where the compensator C is used. For a step input of 20 mm, the overshoot was reduced from 9.3 % to less than 0.01 %. Furthermore, the positioning time (to reduce the error to 10 nm) did not change. The control signal plot shows that the antiwindup makes better use of the driving force, saturating only during the reaching phase.

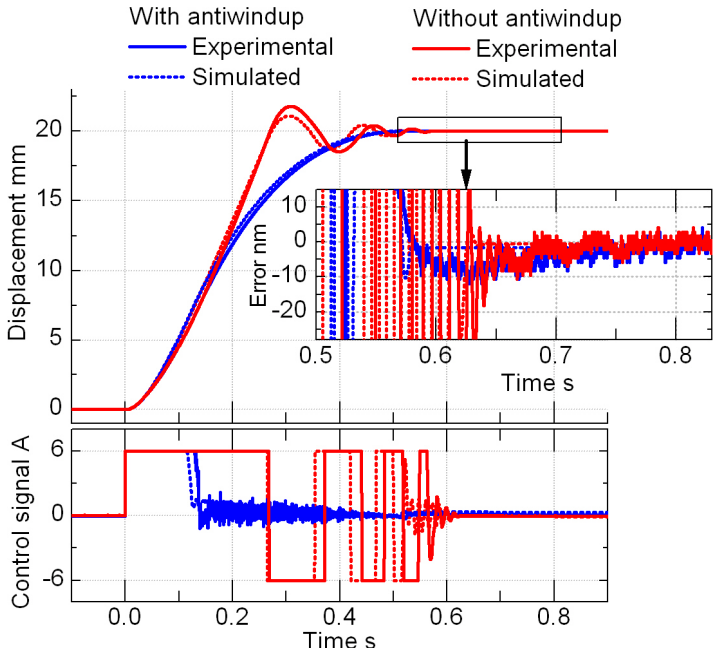

Figure 3-10. Improvement of the performance with the antiwindup.

3.3. PERFORMANCE EVALUATION

In this section, the PTP positioning performance of the NCTF controller using the Y axis mechanism is evaluated. The compensator C, whose parameters are shown in Figure 3-7 is used. The controller also includes the conditionally freeze integrator.

Figure 3-11 shows the positioning performance to a small step of 10 μm and Figure 3-12 shows the positioning performance to a large step input of 20 mm. The step input height of the second case is 2000 times larger than the one used in the first case. In spite of the difference between step input heights, both cases achieve the same positioning accuracy of less than 10 nm. The simulated results agree relatively well with the experimental ones.

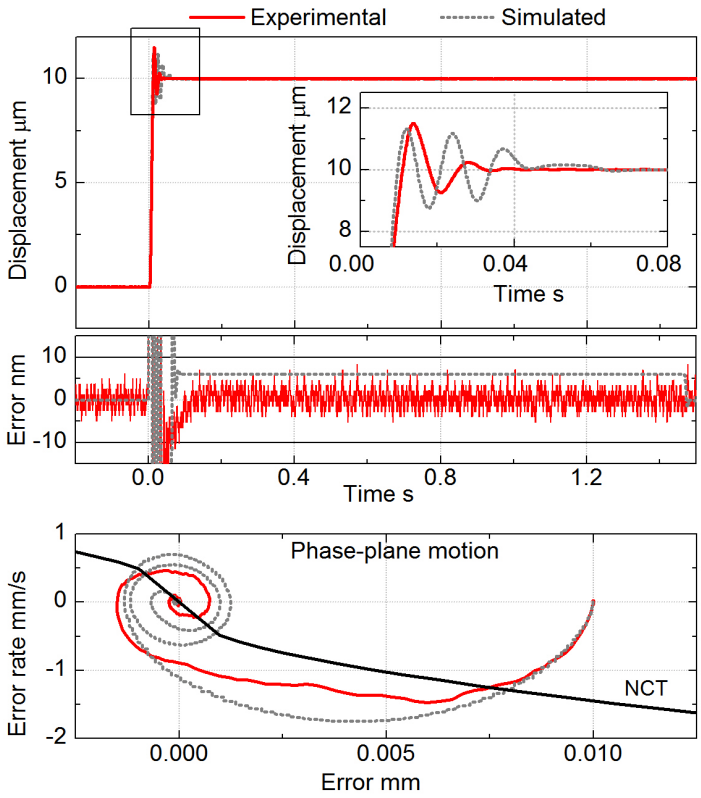

Figure 3-11. Response to a reference input of 10 µm.

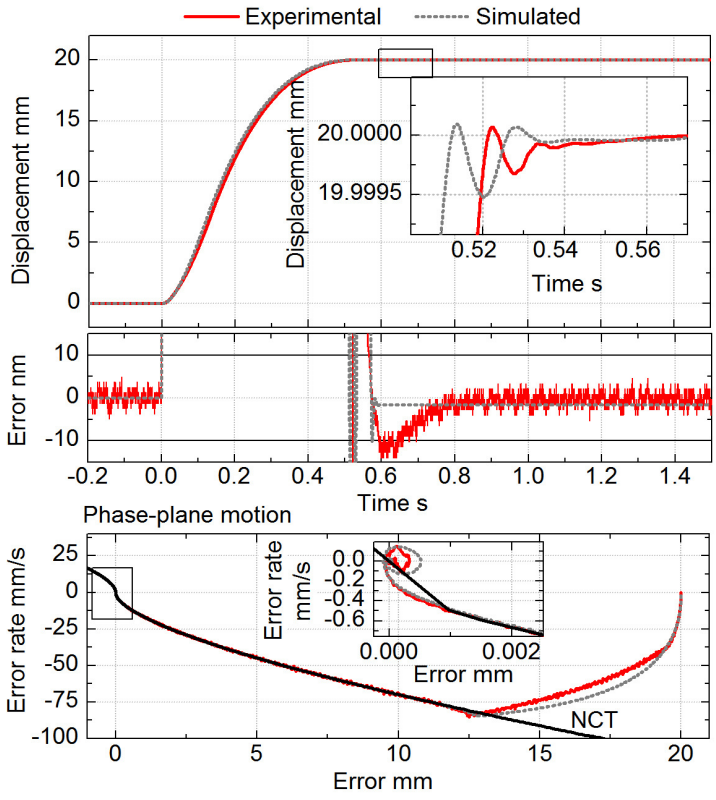

Figure 3-12. Response to a reference input of 20 mm.

Figure 3-13 shows the PTP performance for step inputs of 100 nm, 1 µm, 10 µm, 100 µm, 1 mm, 10 mm, and 20 mm. The figures at the top show the displacements normalized with their respective step input heights. The lower figures show their respective errors (actual values, not normalized), proving that positioning accuracy is better than 10 nm independent of the step height.

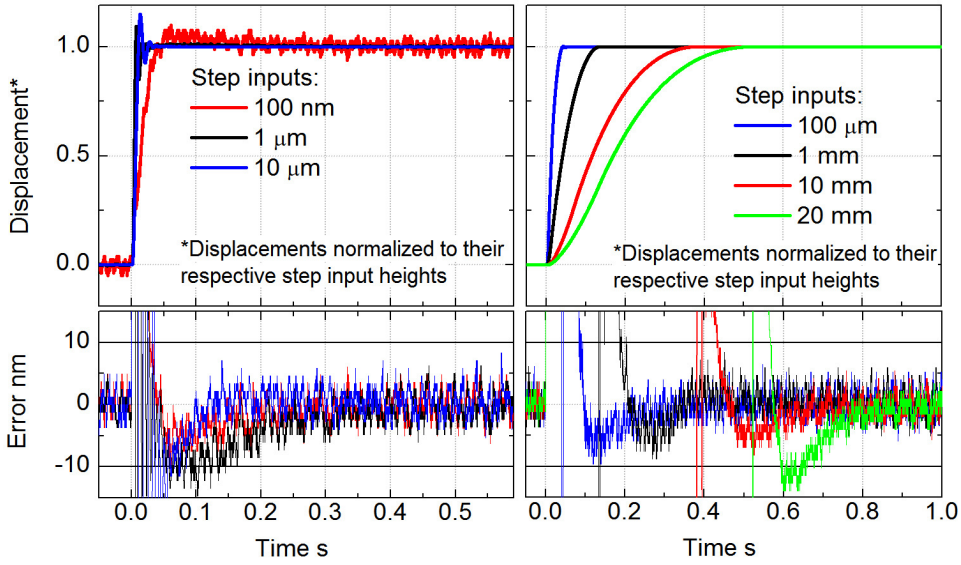

Figure 3-13. Response to several step input heights.

Figure 3-14(a) shows the positioning resolution of the control system. Stepwise inputs of 5 nm are used as reference, and the experiment is repeated in two different frictional conditions: before and after warming up. The warm-up condition is achieved by driving the mechanism with a sinusoidal reference of 20 mm of amplitude and frequency of 0.6 Hz during 40 seconds. Friction parameters were measured before and after the warm-up by the method described in the appendix (Fast Friction Measurement Method). After the warm-up, the Coulomb friction and viscous friction were reduced by 13 % and 24 %, respectively. In spite of the changes in friction, positioning resolution of 5 nm is still kept, as a proof that the designed NCTF controller is robust against friction variations. Figure 3-14 (b) shows the sensor output under the open-loop condition. The input signal to the motor is zero. The amplitude of the measurement noise is the same as the positioning resolution achieved by the NCTF control system. Thus, the achieved positioning performance of the control system is on the limit of the measurement resolution.

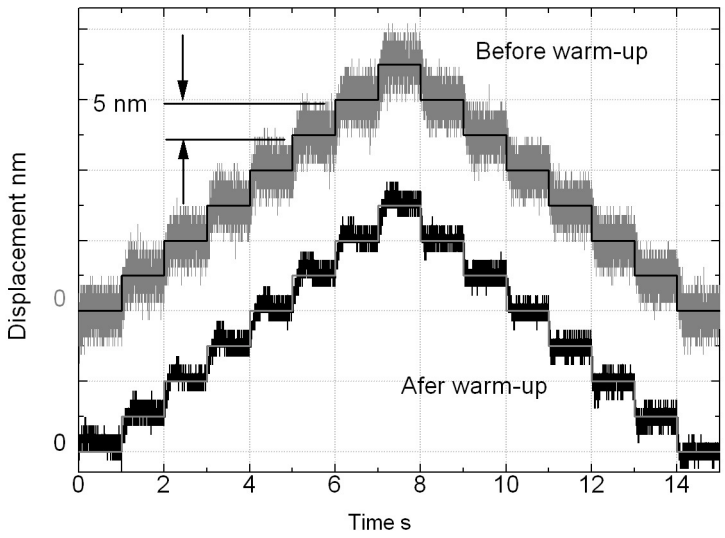

(a) Positioning performance under two frictional conditions

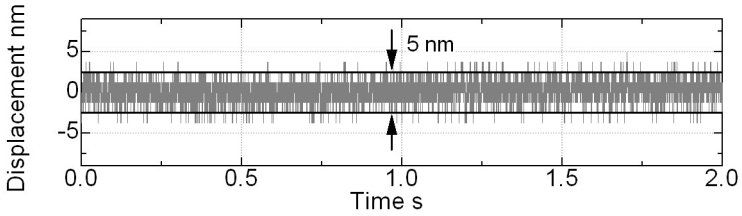

(b) Sensor output in open-loop (motor off)

Figure 3-14. Positioning resolution and sensor output (motor off) have same resolution.

CHAPTER 4 - NCTF CONTROL UNDER THE HEAVYWEIGHT CONDITION

In this chapter, it will be shown that residual vibration is observed on the response of the NCTF control system under the heavyweight condition (X axis mechanism). A solution for residual vibration on NCTF control systems was proposed in [27] using a rotary mechanism. The proposed solution seems to be suitable when the bandwidth of the control system is higher than the frequency of vibration. As it will be shown, in the case of the leadscrew mechanism, the bandwidth of the NCTF control system is lower than the frequency of vibration, requiring a new solution.

Figure 4-1 shows the responses of the NCTF controller under the heavyweight condition and lightweight condition. Both controllers are identical and use the NCT and controller parameters designed in Chapter 3 under the lightweight condition. It is clearly observed that under the heavyweight condition the mechanism presents residual vibration in steady-state, which deteriorates positioning accuracy.

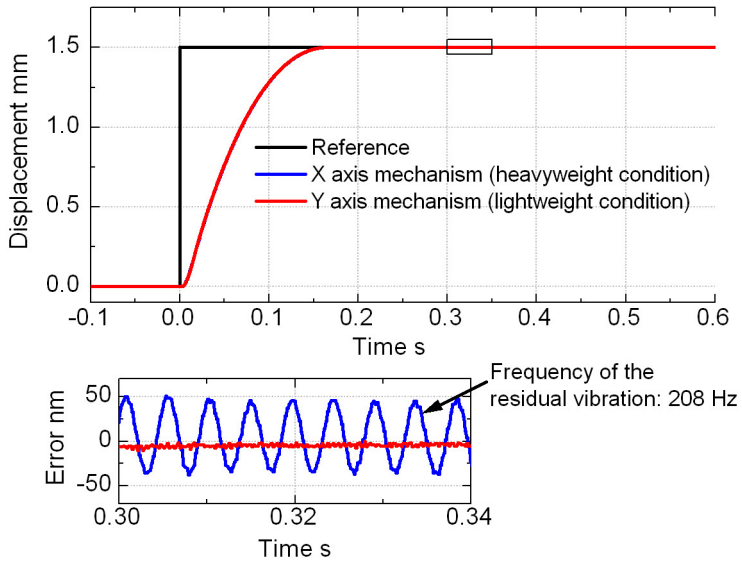

Figure 4-1. Residual vibration on the X axis mechanism after a step input of 1.5 mm.

For the solution of residual vibration, microdynamics and vibration characteristics are examined in open and closed-loop in the following sections. By

identifying the referred characteristics, a simple solution using a second-order notch filter is proposed.

4.1. MICRODYNAMICS AND VIBRATION IN OPEN-LOOP

Figure 4-2 (a) and (b) show the magnitude of the open-loop frequency response of the mechanism under the heavy and lightweight condition, respectively. In both conditions, three sine wave input amplitudes were used: 1 A, 0.5 A, and 0.1 A. For each sine wave amplitude, the frequency of the input signals ranged from 0.5 Hz to 500 Hz. The output gains were normalized to 0 dB at 0.5 Hz. As the results show, both payload conditions present a resonant peak close to 100 Hz, referred as peak 1. The peak 1 is observed only with the sine wave input of amplitude 0.1 A. Under this input, the amplitude of the displacement is of nanometer order (15 nm under the heavyweight condition and 54 nm under the lightweight condition). A resonant peak observed only with small sine wave input amplitudes was clarified as being caused by the nonlinear spring-like behavior [6] of microdynamics. In Figure 4-2(a), the frequency response under the heavyweight condition shows a second resonant peak close to 220 Hz, referred as peak 2. Different from the peak 1 (observed only in microdynamics), the peak 2 is present in the three input amplitude cases, which is a characteristic of two-mass mechanisms.

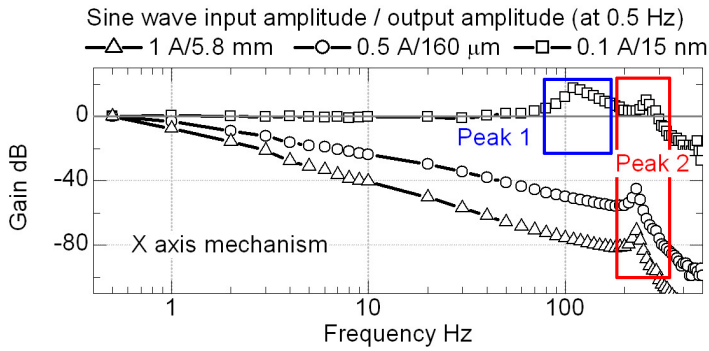

(a) X axis mechanism (heavyweight condition)

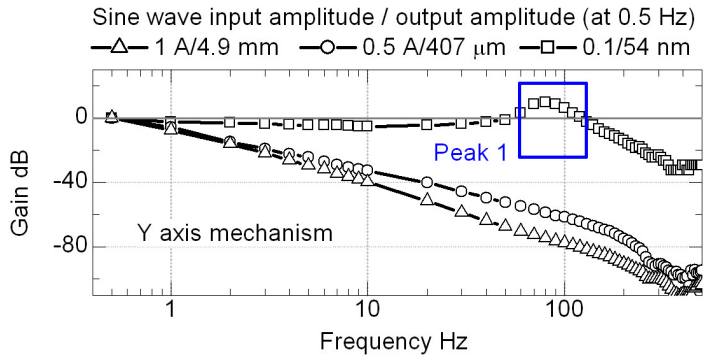

(b) Y axis mechanism (lightweight condition)

Figure 4-2. Open-loop frequency response under the heavy and lightweight conditions.

Figure 4-3 shows the open-loop response of the X axis mechanism (heavyweight condition) with three different step inputs. In the first experiment, the input has amplitude of 2 A and duration of 0.1 s, leading to a final displacement of 4 mm. In the second experiment, the input has amplitude of 3 A and duration of 0.15 s, leading to a displacement of 14 mm. In the third experiment, the input has amplitude of 6 A and duration of 0.3 s, leading to a displacement of 35 mm. Their zoomed views show the behavior of the table immediately before stopping (the origin is shifted to the final displacement). The final displacements of the three experiments are different. However, the three results show a similar displacement retraction caused by the microdynamic spring-like behavior (294 nm in Figure 4-3(a), 290 nm in Figure 4-3(b), and 271 nm in Figure 4-3(c)). Thus, the displacement range of the microdynamics can be identified by observing the spring-like behavior just before the mechanism motion stops, even when different inputs are used (it is assumed that microdynamics characteristics does not change). It is also observed similar frequencies of vibration at the end of the movement: 226 Hz, 215 Hz, and 223 Hz. These frequencies are close to the frequency of the peak 2 in Figure 4-2(a), caused by the vibration of the second mass. Therefore, from a simple

open-loop experiment with a step input, two parameters are easily identified: the range of the microdynamics and the frequency of vibration of the second mass.

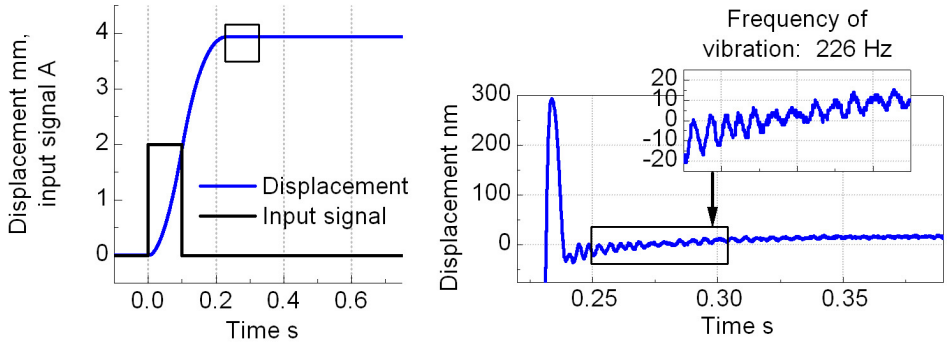

(a) Experiment 1

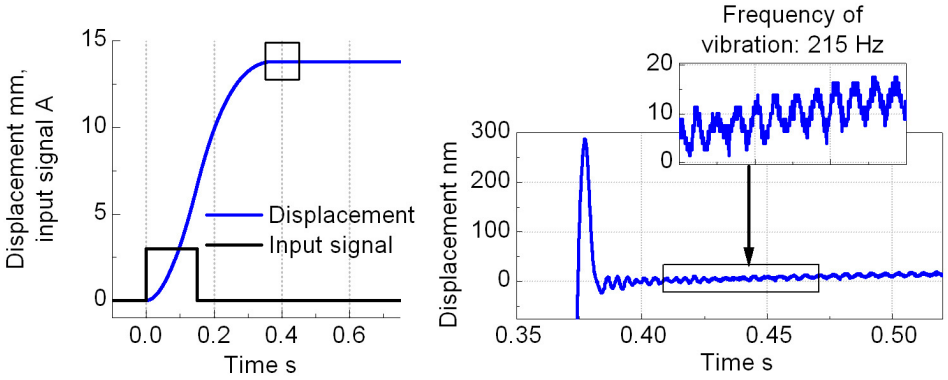

(b) Experiment 2

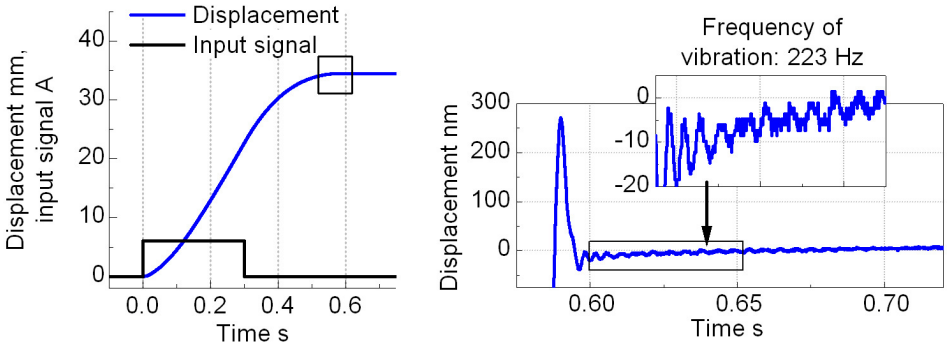

(c) Experiment 3

Figure 4-3. Identification of the microdynamic range and frequency of vibration by an open-loop experiment under the heavyweight condition.

4.2. VIBRATION IN CLOSED-LOOP

In Figure 4-4, the X axis mechanism is driven in close-loop with the NCTF controller designed in Chapter 3. Step input heights of 50 µm, 100 µm, 5 mm, and 10 mm were used as references. For each step height, the experiments were repeated 50 times. The step input was applied at the time 0 s and the frequency and amplitude of residual vibration were measured between 1 to 1.25 s, assuring that the data being analyzed is part of the steady-state response and not part of the transient motion. It is seen that the frequency of the residual vibration varies largely, from 160 Hz to 250 Hz, and that the amplitude of the vibrations are within the rage of microdynamics (from 10 nm to 105 nm). In some cases, no residual vibration is observed, showing that it occurs unpredictably. The large variation of frequency is an indication that a robust solution is necessary.

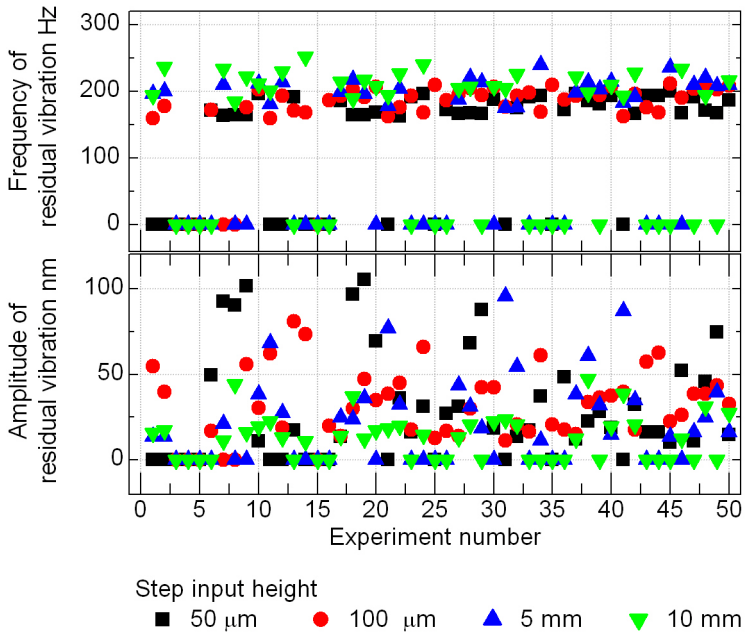

Figure 4-4. Frequency variation of residual vibration with the NCTF control system under the heavyweight condition.

Figure 4-5 shows the gains of the closed-loop frequency response of the NCTF control system. The amplitude of the sine wave references ranged from 100 nm to 10 mm. For each amplitude, the frequency of the reference ranged from 0.5 Hz to 500 Hz. The frequency response shows that, as the amplitude of the sine wave reference decreases, the bandwidth of the control system increases. The maximum bandwidth – achieved with the reference amplitude of 1 µm – is 143 Hz under the heavyweight condition and 93 Hz

under the lightweight condition. However, when the reference amplitude is 100 nm, the bandwidth decreases to 4 Hz under both payload conditions, due to effects of the microdynamics. Under the heavyweight condition, the frequency response in microdynamics shows a resonant peak between 150 and 213 Hz. This range of frequency agrees relatively well with the range of frequency variation in Figure 4-4. In order to solve the residual vibration problem, the resonant peak of the microdynamics under the heavyweight condition must be eliminated.

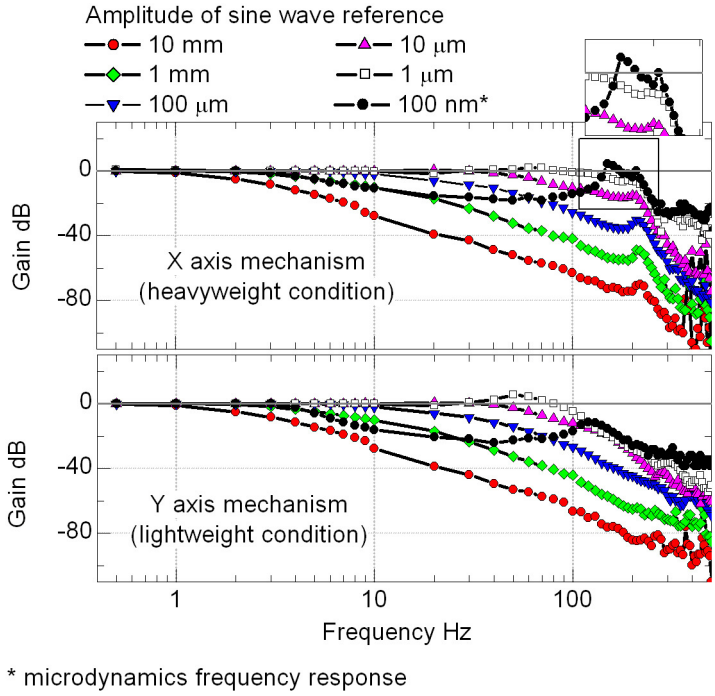

Figure 4-5. Closed-loop frequency response.

4.3. FILTERING THE CONTROL SIGNAL AT THE RESONANT FREQUENCY

A second-order filter is considered as a simple and practical solution, since its design requires only two parameters: a damping coefficient and natural frequency. Two possibilities for the filter are a low-pass and a notch filter, whose transfer functions are respectively given as

$$G_{lp} = \frac{\omega_{lp}^2}{s^2 + 2\zeta\omega_{lp}s + \omega_{lp}^2} \tag{4-1a}$$

$$G_{notch} = \frac{s^2 + \omega_{notch}^2}{s^2 + 2\zeta\omega_{notch}s + \omega_{notch}^2} \tag{4-1b}$$

Figure 4-6 shows the gains of the low-pass and notch filter with several damping ratios. The natural frequency was set to the measured frequency of the open-loop experiment in Figure 4-3(b) ($\omega_{lp} = \omega_{notch} = 2\pi \times 215$ rad/s). A low-pass filter is not convenient because the gain at $\omega_{lp} = 2\pi \times 215$ rad/s changes according to the damping ratio. On the other hand, the notch filter assures that the minimum gain of the filter is always "notched" at ω_{notch} facilitating the design.

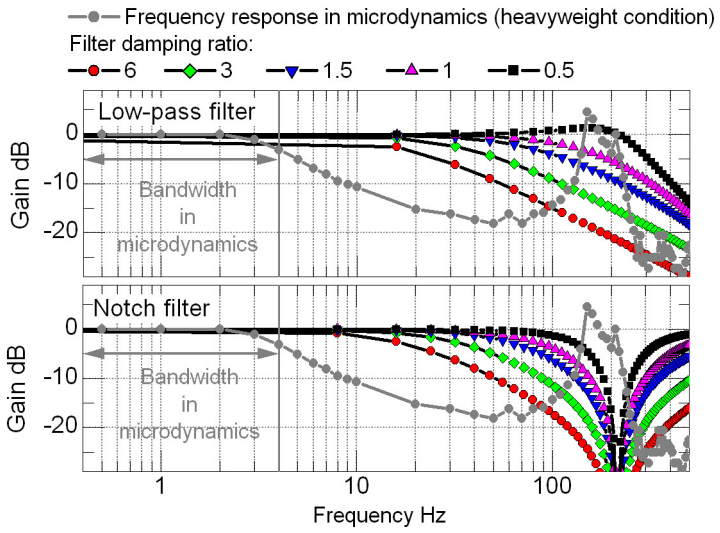

Figure 4-6. Low-pass and notch filter compared to the microdynamic frequency response under the heavyweight condition.

Table 4-1 shows the cutoff frequencies of the notch filter according to different values of ζ_{notch}. All cutoff frequencies are higher than the bandwidth of the control system in microdynamics, which goes until 4 Hz. Thus, the filters do not reduce the bandwidth of the control system under the microdynamics. However, Figure 4-5 shows that the frequency response in macrodynamics has a bandwidth of 143 Hz under the heavyweight condition. If used under such condition, the notch filter decreases the bandwidth in macrodynamics. Therefore, when the mechanism motion is under the macrodynamics

regime, the notch filter is set to be inactive, preserving the macrodynamics frequency characteristics of the control system. The notch filter is set to be active when the mechanism motion falls within the microdynamics range.

Table 4-1. Cutoff frequencies of the notch filter according to the damping ratio

ζ_{notch}	Cutoff frequency (Hz)
0.5	135
1	89
1.5	64
3	34
6	17

Figure 4-7 shows the proposed NCTF controller structure with the notch filter. The notch filter is set to be active only when the error is equal or less than the microdynamics range, thus being referred from now as conditional notch filter.

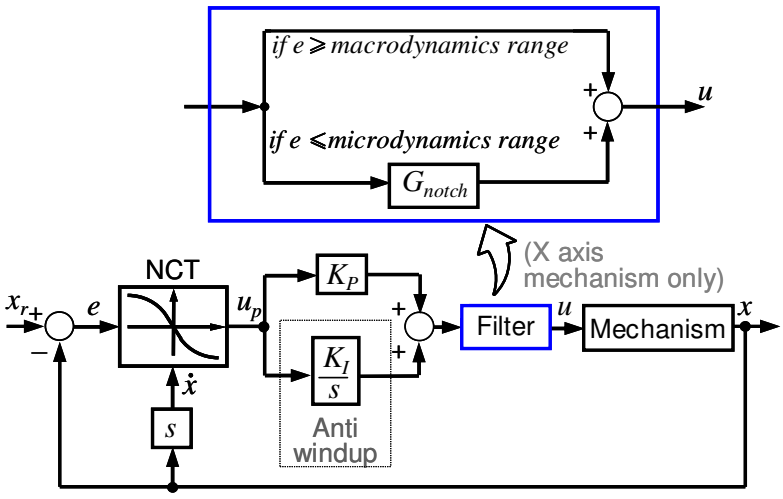

Figure 4-7. Structure of the controller with the conditional notch filter.

Figure 4-8 exemplifies a typical ultra-precision PTP motion and the use of the notch filter according to the conditional rule. In ultra-precision PTP motion, the error is within the microdynamics range whenever the mechanism is in steady-state. The error becomes larger than the microdynamics range when the reference changes to a new set-point. As the mechanism position approaches the new set-point, the error is reduced within the microdynamics range again.

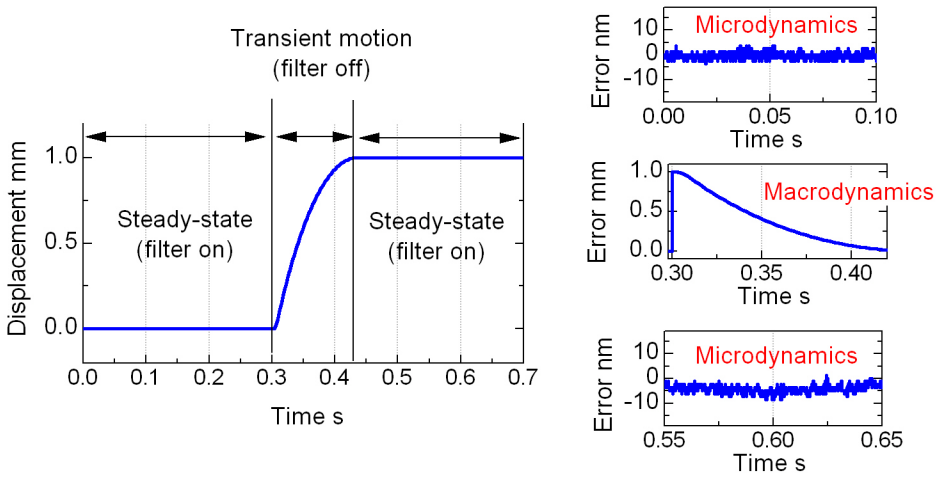

Figure 4-8. Example of a typical ultra-precision PTP motion and the use of the notch filter according to the conditional rule.

4.4. NOTCH FILTER DESIGN PROCEDURE

The design procedure of the conditional notch filter requires only an open-loop experiment with a step input. As shown in Figure 4-3, the amplitude and duration of the open-loop step input can be chosen freely. Because it has little effect in the microdynamics and vibration characteristics. Furthermore, as it will be shown, the robustness of the design method to uncertainties of the parameters (identified from the open-loop experiment) is increased by using large ζ_{notch} values. Referring to the results of the experiment in Figure 4-3(b), it is found that the microdynamics range is 290 nm and the vibration frequency is 215 Hz. The range of 290 nm is used to activate the notch filter as shown in Figure 4-7. ω_{notch} is set to the same value of the vibration in open-loop: $\omega_{notch} = 2\pi \times 215$ rad/s.

Although the parameter ζ_{notch} cannot be identified from the open-loop experiment, its value does not need to be determined exactly. As shown in Table 4-2, the design method allows a wide range of choices of ζ_{notch} which lead to the elimination of residual vibration. The results in Table 4-2 are obtained with the NCTF control system plus the conditional notch filter (microdynamic range = 290 nm and $\omega_{notch} = 2\pi \times 215$ rad/s). For each value of ζ_{notch}, step input experiments using a reference of 100 μm were repeated 100 times and the steady-state responses with residual vibration were counted. From ζ_{notch}

= 1.5, the incidence of responses with residual vibration were reduced to zero. It is important to notice that independent of the value of ζ_{notch}, the transient performance of the control system is not affected since the filter is not active during this period (refer to Figure 4-8). Thus, the advantage of the conditional rule is that the transient performance (rise time, overshoot and positioning time) are the same and not affected, regardless of the choice of the notch filter parameters.

Table 4-2. Increase of the control system robustness to residual vibration according to ζ_{notch}

ζ_{notch}	Responses with residual vibration (%)
0.5	90
1	37
1.5	2
2	0
3	0
6	0

Figure 4-9 shows a comparison of the NCTF control system under the heavyweight condition with and without the conditional notch filter. Figure 4-9(a) shows the gains of the frequency response using a sine wave with amplitude of 100 nm as reference. It is observed that the notch filter completely eliminates the resonant peak caused by the second-mass, while preserving the same bandwidth. Figure 4-9(b) shows the time response of the control system. Residual vibration is not observed with the use of the filter, proving the effectiveness of the proposed method.

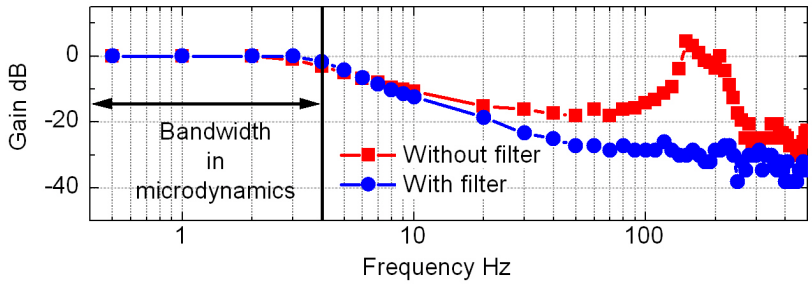

(a) Gains of the frequency response of the NCTF control system in microdynamics

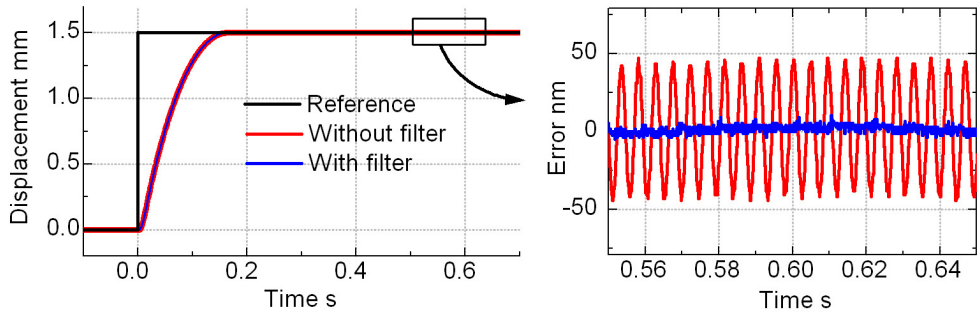

(b) Time response

Figure 4-9. Frequency and time response of the NCTF control system under the heavyweight condition.

4.5. PERFORMANCE EVALUATION

For performance evaluation, the NCTF controller designed in Chapter 3 is used under both payload conditions. The controller for the X axis mechanism (heavyweight condition) includes the conditional notch filter. The notch filter is active for an error less than 290 nm, with $\zeta_{notch} = 3$ and $\omega_{notch} = 2\pi \times 215$ rad/s.

Figures 4-10 to 4-12 shows step input responses of 10 μm, 1 mm, and 20 mm heights. As it can be seen, both payload conditions show very similar performance. The notable difference is observed during the transient response (easily seen in the phase-plane plots). The Y axis mechanism does not show vibration during the transient motion. The X axis mechanism has a vibrating transient motion caused by the second-mass. The vibration is eliminated during steady-state because the filter becomes active. The NCTF controller shows robustness to payload variation (4.9 times higher in the X axis

mechanism) and also robustness to friction variation (two times larger in the X axis mechanism).

Figure 4-13 shows the PTP performance for step inputs of 100 nm, 10 μm, 100 μm, 1 mm, 10 mm, and 20 mm. The figures at the top show the displacements normalized with their respective step input heights. The lower figures show their respective errors (actual values, not normalized), proving that positioning accuracy is better than 10 nm independent of the step height. No residual vibration is observed under the heavyweight condition, independent of the step input height.

Finally, Figure 4-14 shows that positioning resolution of 5 nm is achieved under the heavyweight condition. This is the same positioning resolution of the NCTF controller under the lightweight condition (Figure 3-14(a)). The experiment is repeated before and after warm-up, whose purpose is to change the friction condition. The friction condition is changed and measured in the same way as explained in Subsection 3.3. After the warm-up, the Coulomb friction and viscous friction were reduced by 12 % and 26 %, respectively. In spite of the changes in friction, positioning resolution of 5 nm is still kept, showing that the designed NCTF controller with the conditional notch filter is robust against friction variations.

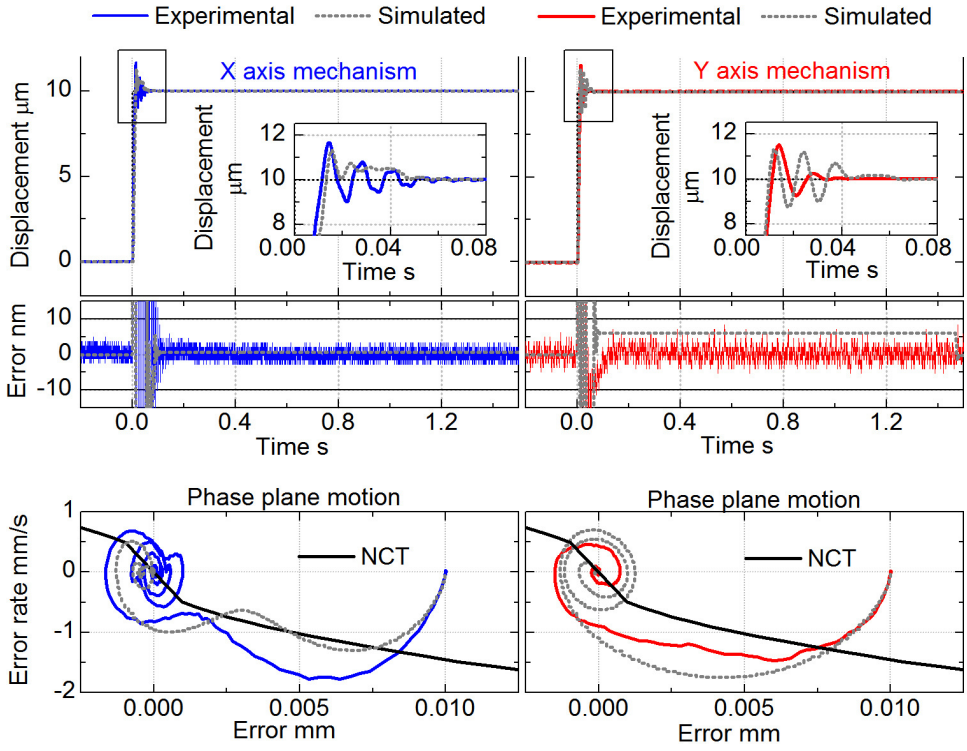

Figure 4-10. Experiments and simulations with a step input reference of 10 µm.

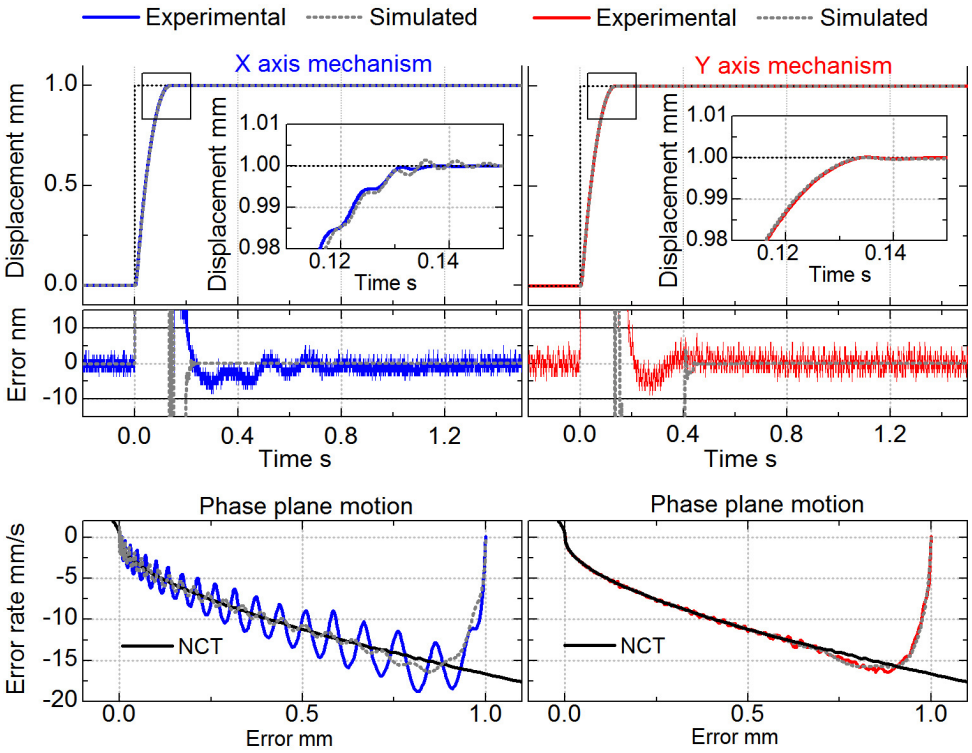

Figure 4-11. Experiments and simulations with a step input reference of 1 mm.

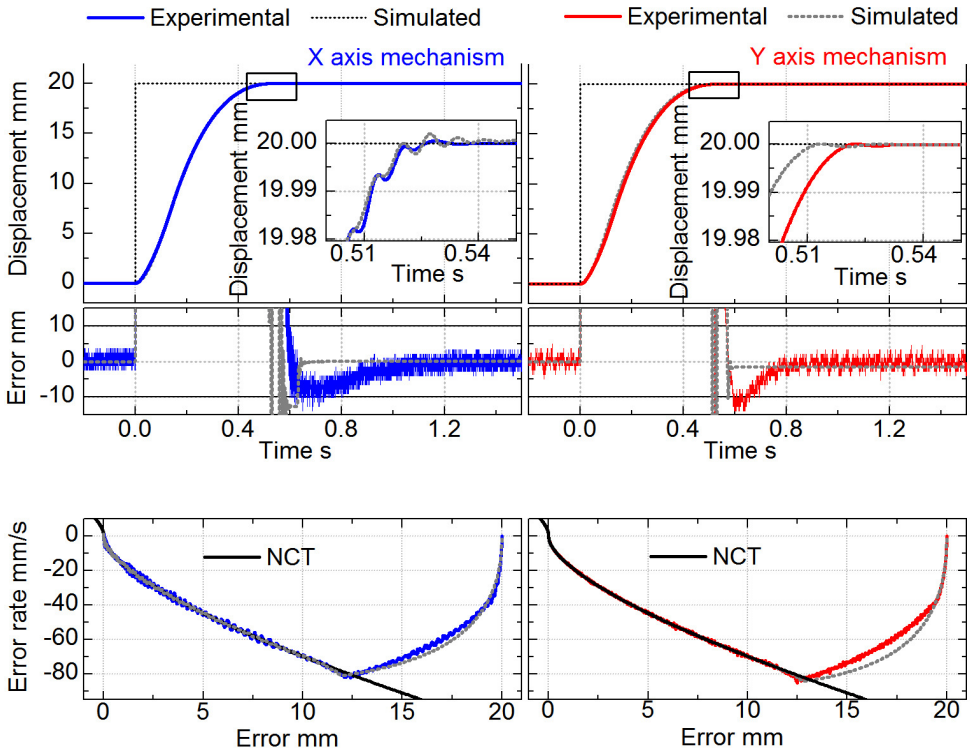

Figure 4-12. Experiments and simulations with a step input reference of 20 mm.

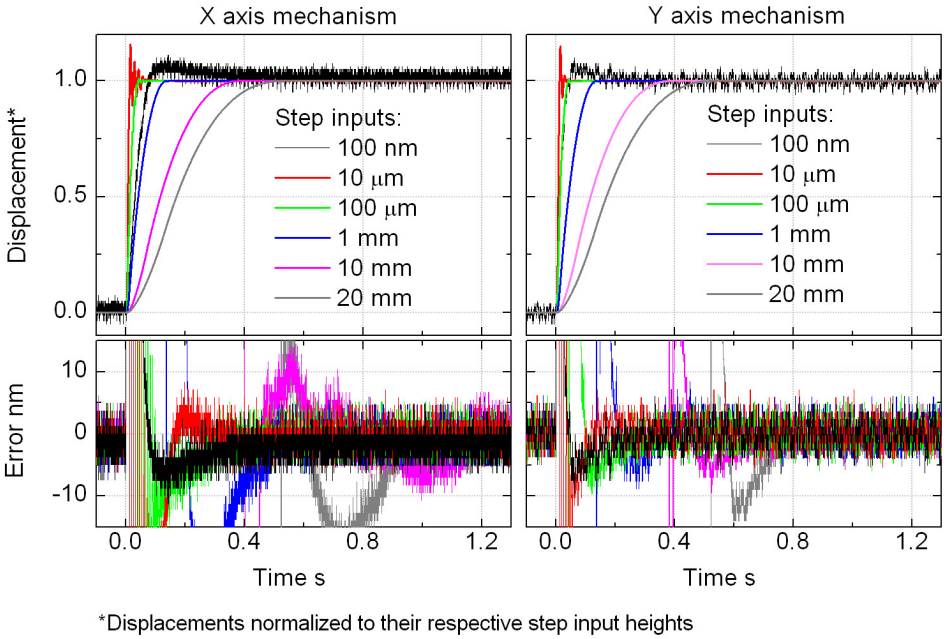

Figure 4-13. Performance comparison between both payload conditions with steps from 100 nm to 20 mm.

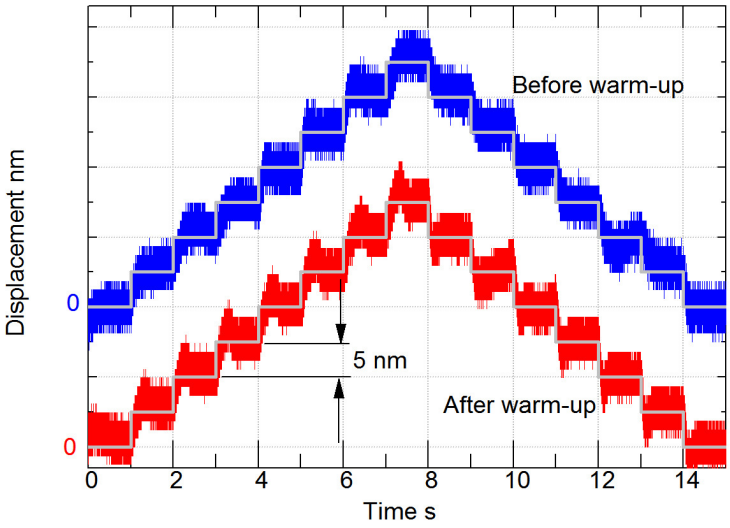

Figure 4-14. X axis mechanism (heavyweight condition) driven by stepwise inputs of 5 nm under two friction conditions.

CHAPTER 5 - FAST POINT-TO-POINT POSITIONING

In most applications of point-to-point positioning, not only high accuracy and robustness are important, but also high speed motion. In industrial applications, fast positioning systems reduce the processing time, increasing production output and reducing manufacturing cost. In this chapter, the speed of the mechanism motion for PTP positioning is improved. The method proposed aims to improve positioning time without increasing overshoot.

In order to compare the performances of different controllers, three performance indexes are used in this research: rise time, overshoot and positioning time. The rise time criteria adopted is the time the mechanism takes to go from 10% to 90% of the total movement (as defined in [30]). The positioning time indicates the time the control system takes to reduce the error to less than 100 nm.

The method for fast PTP proposed in [28] for a rotary mechanism, was evaluated in this research using the leadscrew mechanism. As Figure 5-1 shows, although rise time is reduced, the response shows excessive overshoot. Also, oscillations before steady-state extends the positioning time. The very inclined profile of the MFNCT [28] makes the decelerating motion too fast close to the origin. On the phase-plane, the mechanism motion overshoots the MFNCT.

As a solution for the leadscrew mechanism, the nominal characteristic trajectory should be similar to the MFNCT when the mechanism motion is far from the origin of the phase-plane. This leads to fast movement for long strokes. On the other hand, the same trajectory should softly attenuate the mechanism motion as it approaches the origin of the phase-plane. This is useful to avoid overshoot and it is a characteristic of the NCT designed in subsection 3.1.1 (referred in this chapter as the conventional NCT).

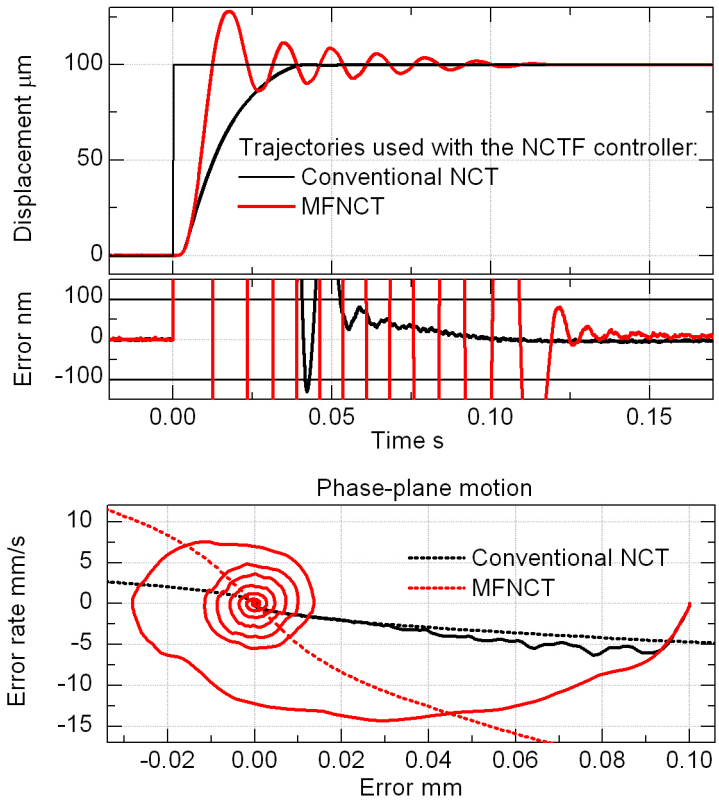

Figure 5-1. Excessive overshoot and long positioning time with the MFNCT trajectory.

5.1. Modified Open-Loop Experiment and Construction of a Fast Trajectory

Figure 5-2(a) shows the simulated response of the lightweight mechanism when decelerated by a derivative controller (D controller). The beginning of the deceleration is intense, saturating the actuator. As velocity reduces, the control signal attenuates softly until the mechanism completely stops. This behavior approaches the desired solution for the leadscrew mechanism.

The control signal profile of the D controller is relatively close to a normalized sine wave, whose amplitude is the actuator saturation. The period T of the sine wave is adjusted by try–and-error so that the velocity approaches zero without becoming

negative. Figure 5-2(b) shows the modified open-loop response (simulation) with the normalized sine wave, which approaches closely to the response of the D controller.

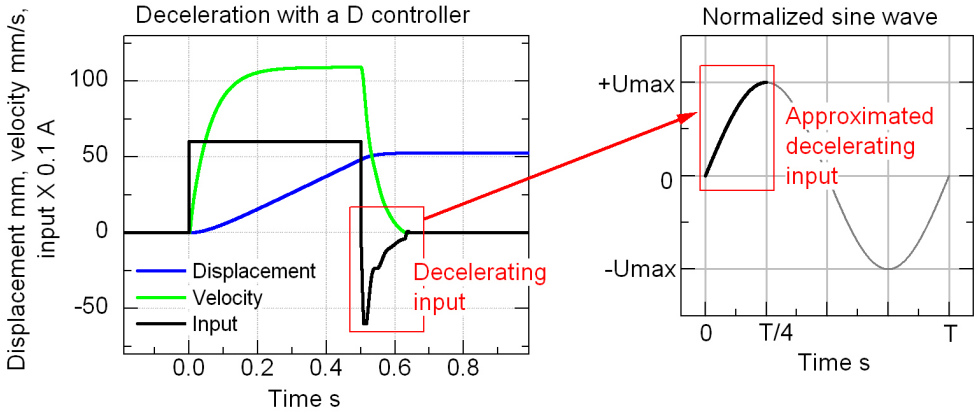

(a) Control signal of the D controller approximated to a sine wave input

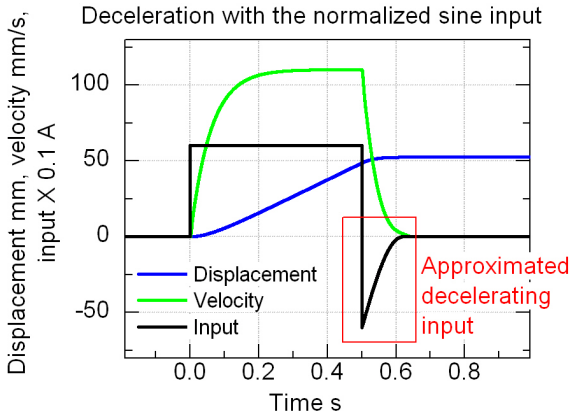

(b) Open-loop response of the mechanism with the normalized sine wave input

Figure 5-2. Modified open-loop experiment for the construction of a fast trajectory.

Figure 5-3 shows the experimental open-loop response using the normalized sine wave input with the Y axis mechanism. The period of the sine was adjusted so that the velocity approaches softly to zero, without becoming negative (zoomed view).

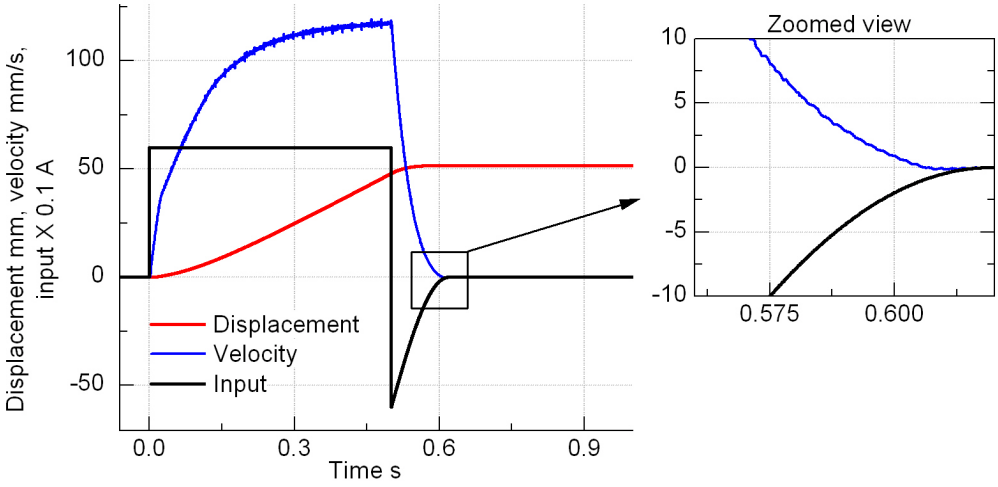

Figure 5-3. Experimental result with the Y axis mechanism using the normalized sine wave input.

The construction of the new trajectory, from now being referred as MFNCTS (which stands for Modified Fast Nominal Characteristic Trajectory by Sine wave), is identical to the construction of the conventional NCT, described in Subsection 3.1.1. Figure 5-4 shows a comparison among the conventional NCT, the MFNCT and the MFNCTS trajectories. As it is observed, the MFNCTS is almost similar to the MFNCT when the error is large. The zoomed view shows that as the error becomes small (close to the origin), the MFNCTS profile becomes similar to the conventional NCT profile, but not similar to the MFNCT one. From the profile of the MFNCTS, it is expected that the mechanism motion stops without overshooting. At the same time, positioning time is expected to be reduced.

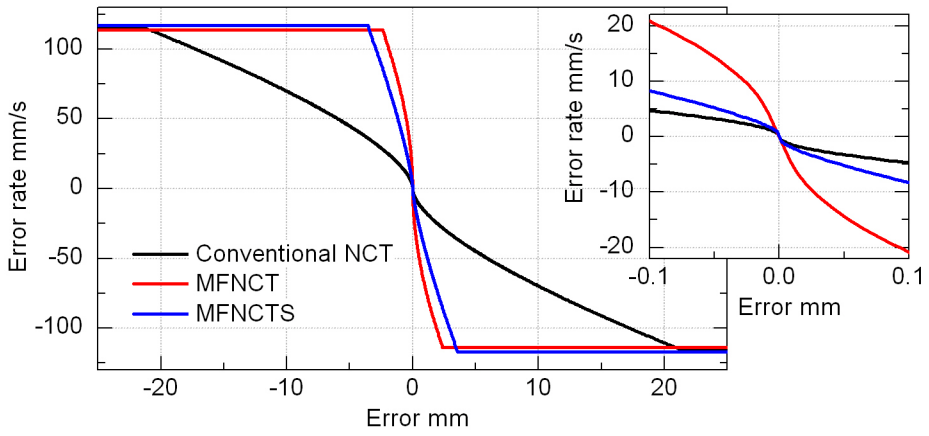

Figure 5-4. Comparison among the conventional NCT, MFNCT, and MFNCTS.

Figure 5-5 shows a comparison among NCTF controllers using the conventional NCT, MFNCT, and MFNCTS trajectories. The three trajectories are linearized to have the same inclination α of 505 s^{-1}. As it is observed, although the controller with the MFNCT has the shortest rise time, the oscillations before stopping yield longer positioning time than the controller with the MFNCTS. Moreover the controller with the MFNCT presents increased overshoot, while the MFNCTS does not increase the overshoot.

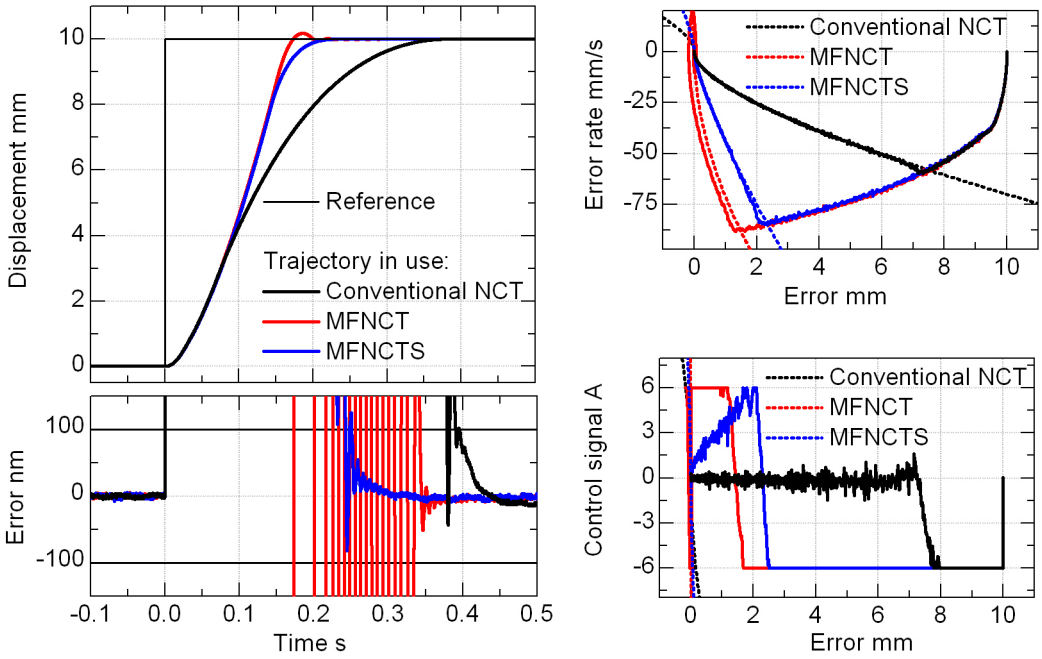

Figure 5-5. Comparison among the conventional NCT, MFNCT, and MFNCTS with a step input reference of 10 mm.

5.2. PERFORMANCE EVALUATION

As shown in Figures 5-1 and 5-5, the NCTF controller using the MFNCT does not achieve good performance with the leadscrew mechanism, except short rise time. In the case of short step input (Figure 5-1), the mechanism motion vibrates leading worse positioning time than the conventional NCT. For large step input (Figure 5-5), little improvement was obtained. Therefore, the performance evaluation of the NCTF controller with the MFNCTS will be made by comparing it against the NCTF controller

with the conventional NCT. The controller with the MFNCT will not be compared since its implementation was not successful.

In order to evaluate the performance of the proposed method, two controllers are defined according to Table 5-1.

Table 5-1. Controllers used to evaluate the performance of the fast PTP method

	Trajectory type	Inclination of the trajectory close to the origin (s^{-1})	Design parameters	
			ζ	$\omega_n T$ (rad)
Controller 1	Conventional NCT	505	5	0.32
Controller 2	MFNCTS	600	6	0.28

The Controller 1 is the same controller designed in Chapter 3. The parameters and inclination of the MFNCTS of the Controller 2 were initially based on Controller 1 and fine-tuned experimentally.

Figures 5-6 to 5-9 show the experimental and simulated step responses from 100 μm to 20 mm of the heavyweight condition (X axis mechanism) and the lightweight condition (Y axis mechanism). In the case of a small step input of 100 μm (Figure 5-6), although rise time is reduced with Controller 2, positioning time is practically the same. This is because of the little difference between the MFNCTS and the conventional NCT close to the origin of the phase-plane trajectory. However, as the step input reference increases to 1 mm, 10 mm and 20 mm, it becomes clear the advantage of the MFNCTS over the conventional NCT for the improvement of positioning time. Furthermore, overshoot does not increase.

For a quantitative comparison, Table 5-2 and Table 5-3 show the averaged response of 20 experiments under each payload condition. The average of all results show that rise time under the heavyweight condition was reduced by 42%, while positioning time was reduced by 19%. Under the lightweight condition, rise time was reduced by 43% and positioning time was reduced by 24%. Considering only milimetric step input heights (1, 10 and 20 mm) and excluding the results from the 100 μm step input, rise time and positioning time were reduced respectively by 32% and 26% under the heavyweight condition. Under the lightweight condition, rise time and positioning time were reduced respectively by 32% and 31%. In both payload conditions, overshoot did not change significantly.

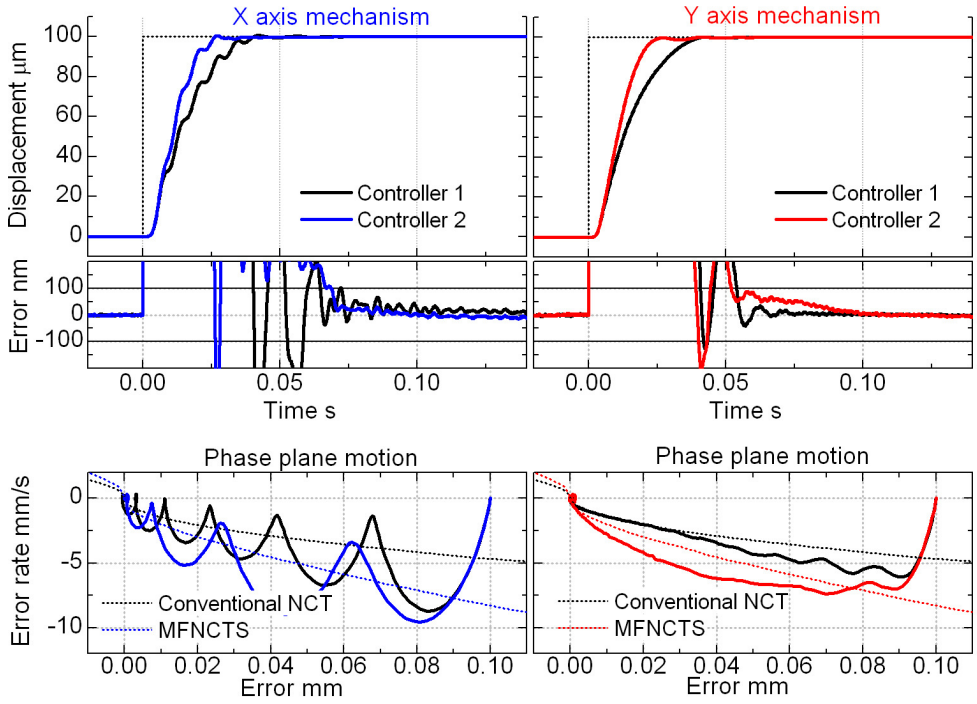

(a) Experiments

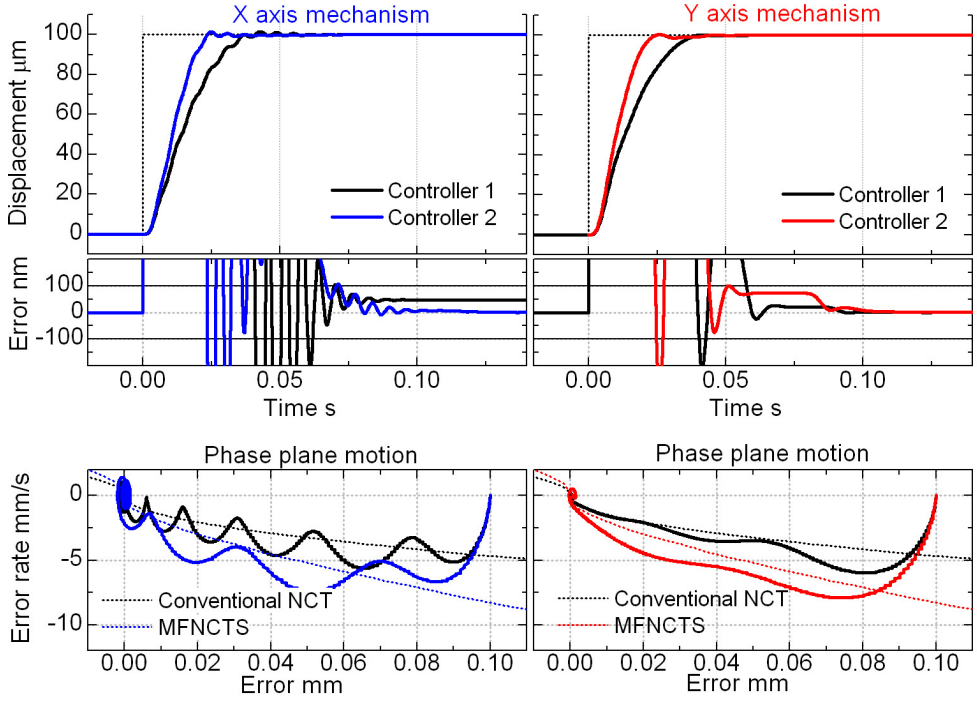

(b) Simulations

Figure 5-6. Comparison between controllers using the conventional NCT and MFNCTS. 100 µm step input.

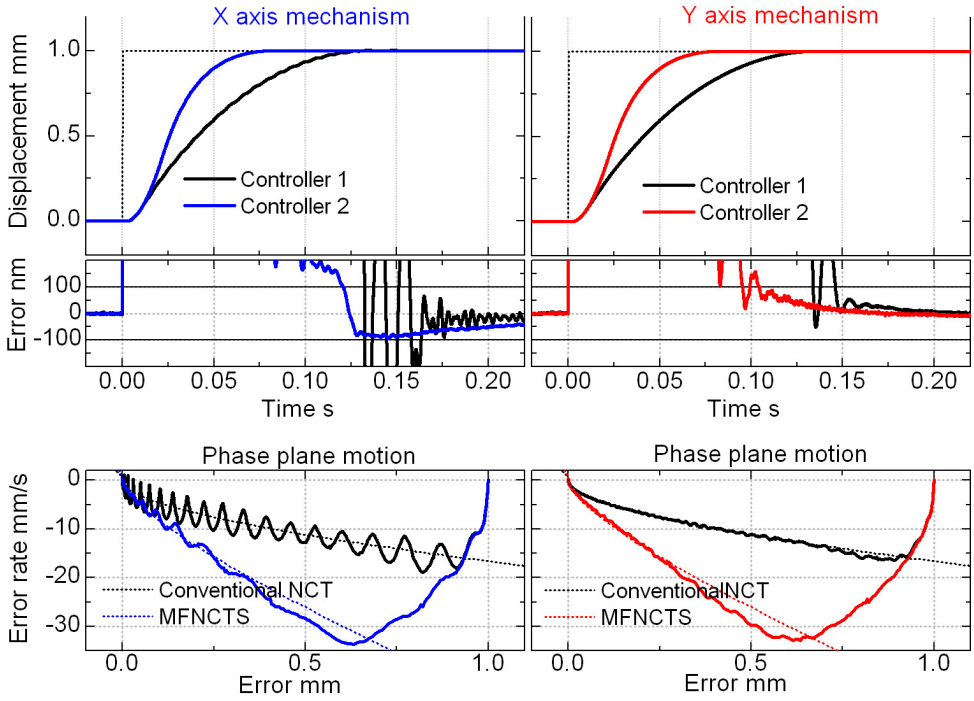

(a) Experiments

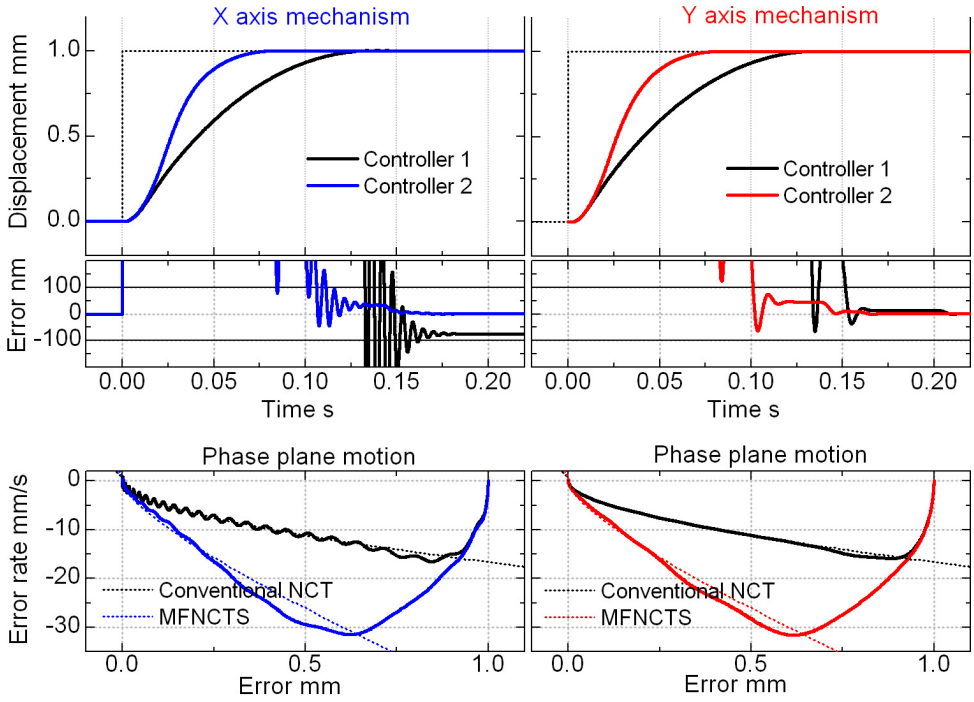

(b) Simulations

Figure 5-7. Comparison between controllers using the conventional NCT and MFNCTS. 1 mm step input.

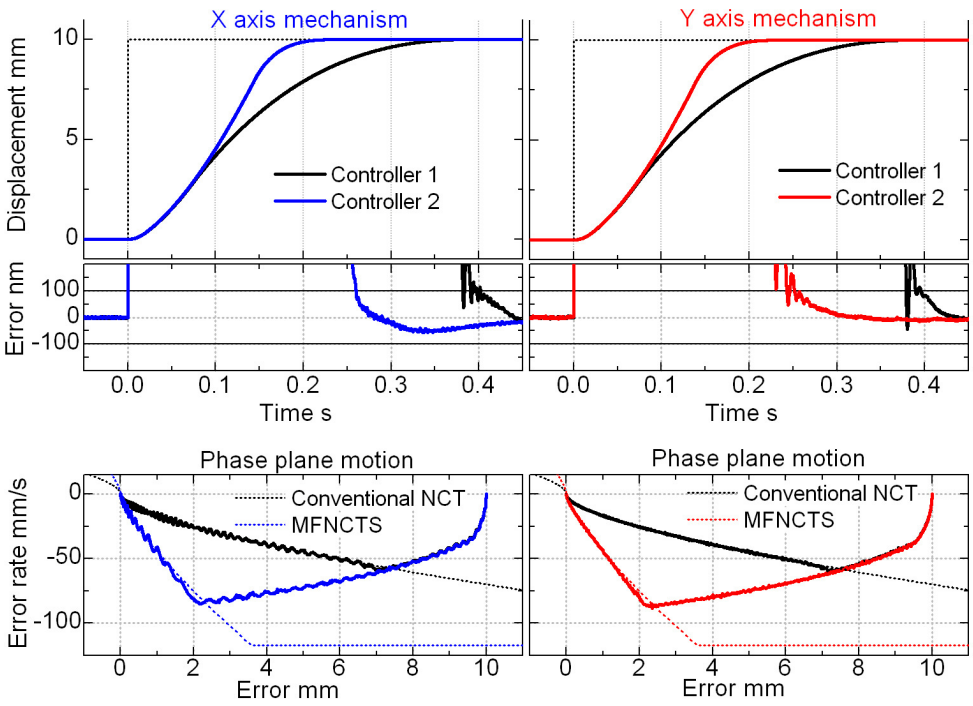

(a) Experiments

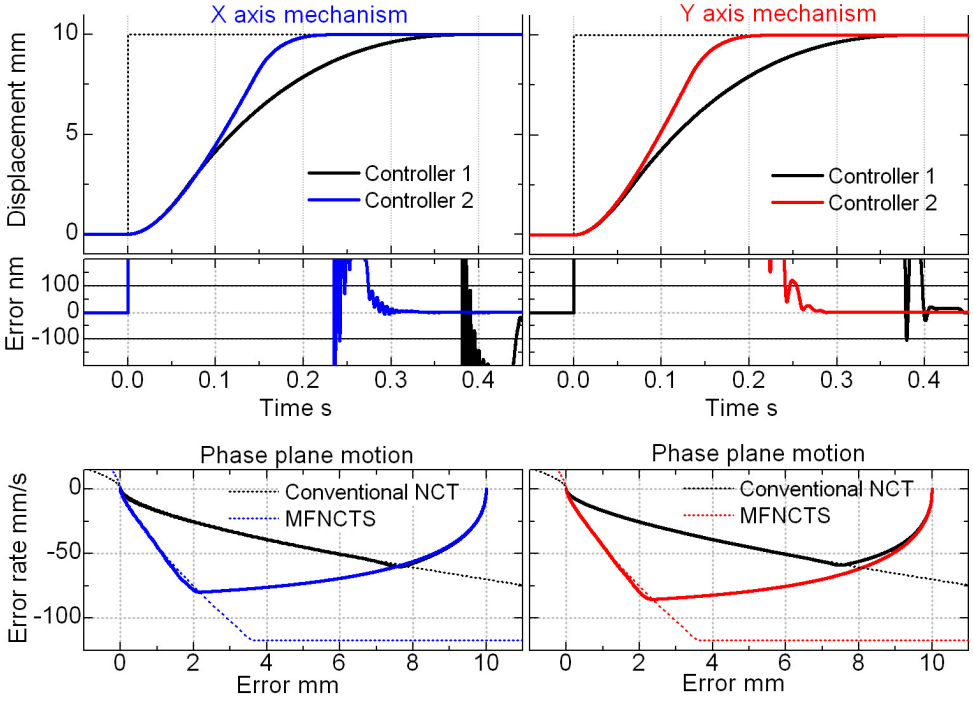

(b) Simulations

Figure 5-8. Comparison between controllers using the conventional NCT and MFNCTS. 10 mm step input.

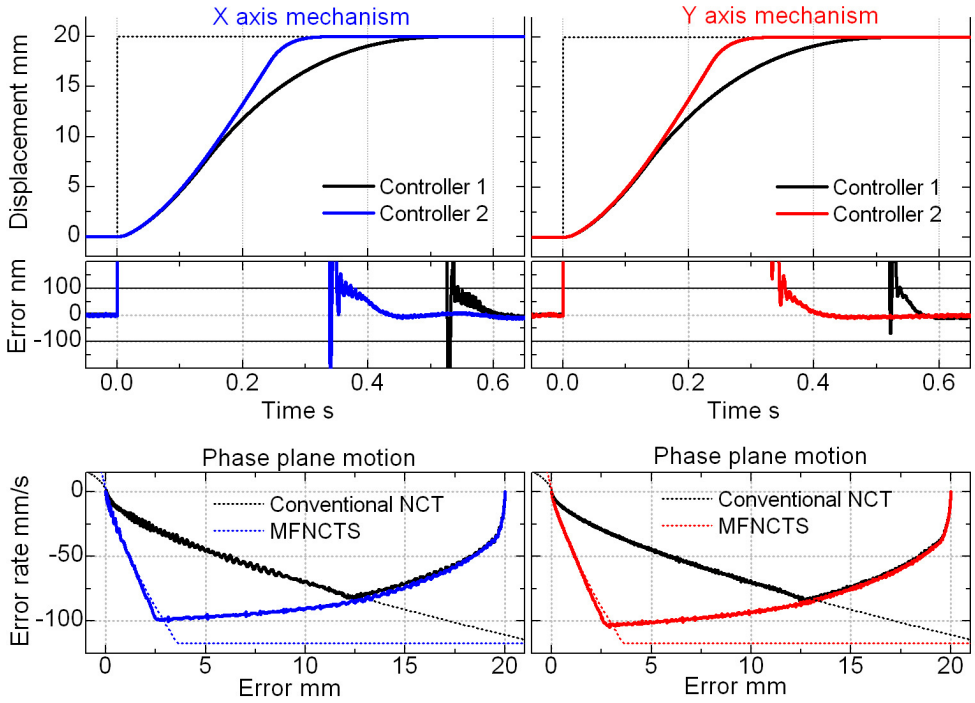

(a) Experiments

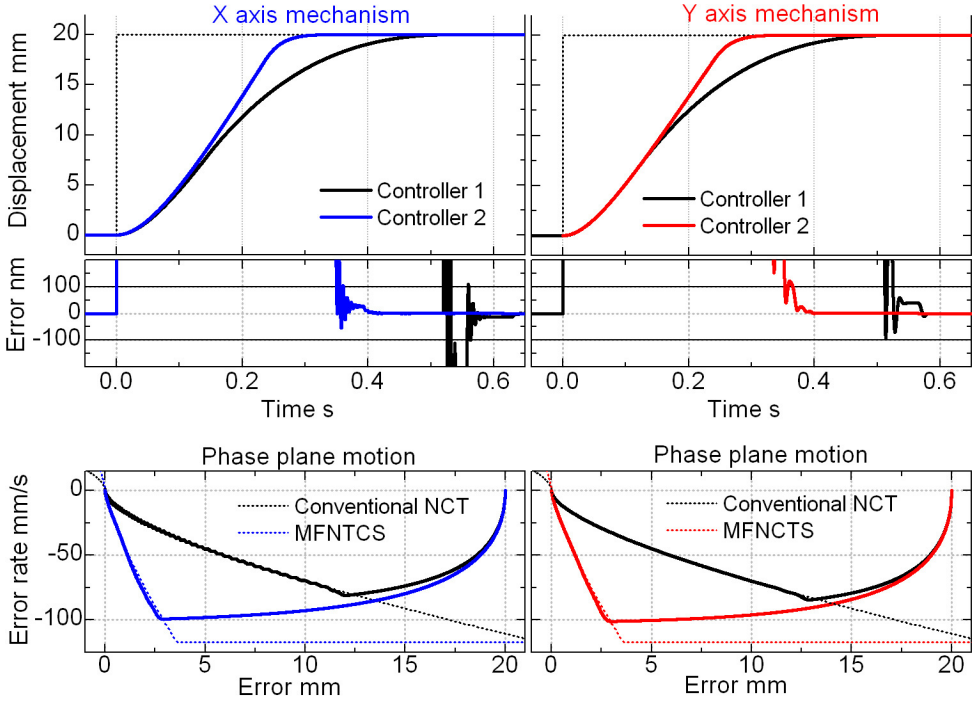

(b) Simulations

Figure 5-9. Comparison between controllers using the conventional NCT and MFNCTS. 20 mm step input.

Table 5-2. Average of 20 experiments with the X axis mechanism (heavyweight condition)

Step height	Performance Index	Controller 1		Controller 2	
		Average	Standard deviation	Average	Standard deviation
100 μm	Rise time (s)	0.023900	0.001427	0.014540	0.000114
	Overshoot (%)	0.55	0.17	0.11	0.125467
	Positioning time (s)	0.062490	0.007464	0.064150	0.015014
1 mm	Rise time (s)	0.080700	0.000501	0.039030	0.000187
	Overshoot (%)	0.05	0.03	0.01	0.004103
	Positioning time (s)	0.162400	0.011777	0.128890	0.009655
10 mm	Rise time (s)	0.213390	0.000210	0.123150	0.000430
	Overshoot (%)	0.00	0.00	0.00	0.000727
	Positioning time (s)	0.395430	0.013668	0.274840	0.023988
20 mm	Rise time (s)	0.288400	0.000754	0.191780	0.000713
	Overshoot (%)	0.00	0.00	0.00	0.000571
	Positioning time (s)	0.536520	0.007360	0.384740	0.020059

Table 5-3. Average of 20 experiments with the Y axis mechanism (lightweight condition)

Step height	Performance Index	Controller 1		Controller 2	
		Average	Standard deviation	Average	Standard deviation
100 μm	Rise time (s)	0.024210	0.000045	0.014370	0.000175
	Overshoot (%)	0.11	0.01	0.24	0.071576
	Positioning time (s)	0.054120	0.002083	0.052620	0.000440
1 mm	Rise time (s)	0.080550	0.000089	0.038960	0.000105
	Overshoot (%)	0.01	0.00	0.00	0.004267
	Positioning time (s)	0.145820	0.001299	0.107960	0.003832
10 mm	Rise time (s)	0.212120	0.000177	0.120010	0.000571
	Overshoot (%)	0.00	0.00	0.00	0.000072
	Positioning time (s)	0.391590	0.002705	0.257790	0.005526
20 mm	Rise time (s)	0.285080	0.000442	0.186480	0.001049
	Overshoot (%)	0.00	0.00	0.00	0.000028
	Positioning time (s)	0.534080	0.003102	0.360850	0.004667

CHAPTER 6 - CONTINUOUS MOTION CONTROL

Continuous motion control is important in positioning systems because it determines the profile accuracy of the workpiece being machined. However, friction in positioning mechanisms slows the motion, affecting the tracking performance. The NCTF controller structure for PTP does not address continuous motion, and, as a consequence, the controller performance is poor for continuous path tracking. This chapter proposes a modification of the NCTF controller for continuous motion.

The controller structure modification proposed in this chapter is based on the original NCTF controller for PTP studied in the previous chapters. The implementation is simple and does not increase the complexity of the controller structure. Moreover, in the case of PTP positioning, the modified structure has the same control law of the original NCTF controller for PTP position.

6.1. PROPOSED CONTROLLER STRUCTURE MODIFICATION FOR CONTINUOUS MOTION CONTROL

The original NCTF controller for PTP assumes that the reference rate ($\dot{x}_r$) is always zero. From this assumption, the structure of the NCTF controller for PTP (Figure 6-1) is designed so that the actual error rate ($\dot{e}_{act}$) does not include the information of the reference rate. This controller will be referred from now as PTP NCTF controller.

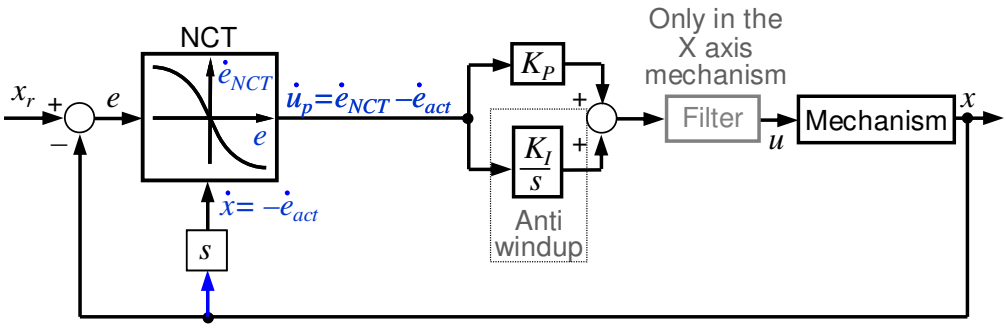

Figure 6-1. Structure of the NCTF controller for PTP positioning.

Based on the PTP NCTF controller structure in Figure 6-1, the continuous controller structure is obtained by considering the value of $\dot{x}_r$ as part of the actual error rate ($\dot{e}_{act}$). The proposed controller structure is given in Figure 6-2 and will be referred as Continuous Motion NCTF controller.

Notice that the complexity of the controller does not increase. At the same time, when $\dot{x}_r$ is zero, the structure in Figure 6-2 is identical to the structure in Figure 6-1. Therefore, the Continuous Motion NCTF controller has the same control law of the PTP NCTF controller during PTP positioning.

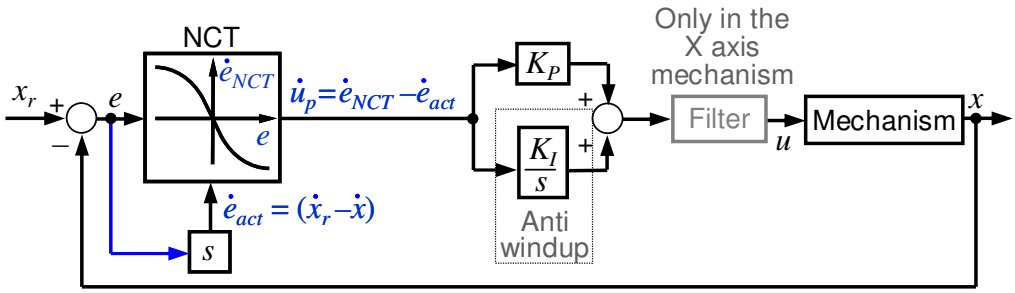

Figure 6-2. Structure of the NCTF controller for continuous motion.

6.2. PI-D CONTROLLER FOR PERFORMANCE COMPARISON

For the purposes of comparison, a PI-D controller, whose structure is given in Figure 6-3, was designed. The gains of the PI-D controller are based on the Continuous

Motion NCTF controller when the mechanism motion is within the linear range of the NCT. Similarly to the NCTF controller, the PI-D controller has an antiwindup integrator.

The gains of the PI-D controller were then fine-tuned, so that the PI-D controller achieves comparable performance with the Continuous Motion NCTF controller under two references: a step input of 1 mm, and a circular motion of 5 mm of radius and 1 Hz. The PI-D controller gains are K_P = 296.94 A/mm, K_I = 15829.05 A/mm·s, and K_D = 1.47 A·s/mm.

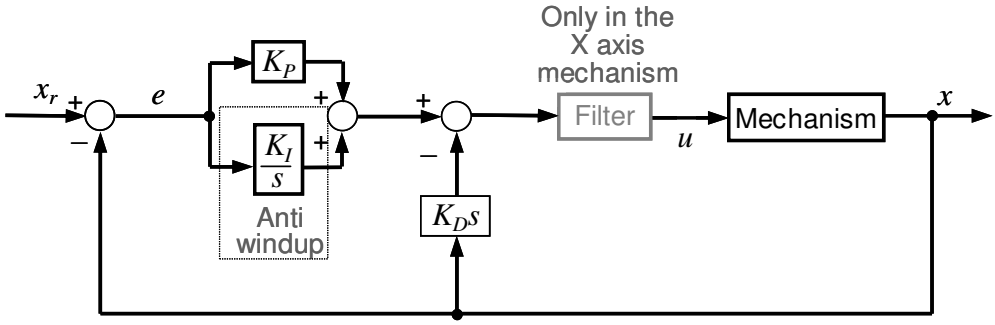

Figure 6-3. PI-D controller structure designed for comparison with the Continuous Motion NCTF controller.

6.3. PERFORMANCE EVALUATION

The NCT and the compensator gains of the Continuous Motion NCTF controller are the same as the ones designed in Chapter 3 for PTP. Also, the same controller parameters are used with the X axis mechanism (heavyweight condition) and Y axis mechanism (lightweight condition). For the performance evaluation of continuous motion, the experiments are realized as if the two axis mechanisms were conceptually stacked like in an XY table configuration. Thus, using a sine wave reference with the X axis mechanism, and a cosine wave reference with the Y axis mechanism, the resulting contour is a circle. Each experiment was repeated twenty times, and the average error and standard deviation were calculated.

6.3.1 Convention for Error Measurement

In order to compare the performances of different controllers, two error measurements are used. The first error measurement is calculated as:

$$\max \left| x_r - x \right| \qquad (6\text{-}1)$$

and refers to the maximum reference tracking error. The second error measurement is used to evaluate the contour accuracy and is represented graphically for the circular and square motion in Figure 6-4. In the case of circular motion, the maximum radial error is the absolute value of e_{out} or e_{inn}, whichever is larger.

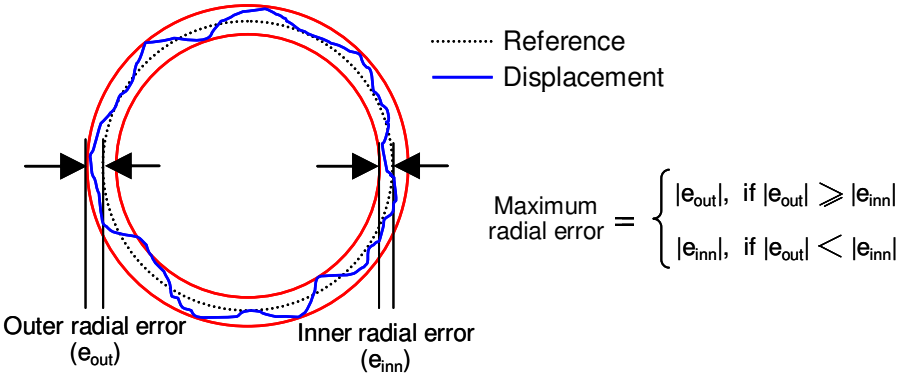

(a) Contour error in circular motion

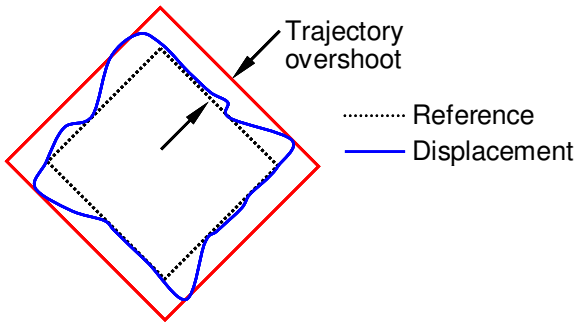

(b) Contour error in square motion

Figure 6-4. Contour error measurement.

6.3.2 PTP NCTF Controller vs. Continuous Motion NCTF Controller

Figures 6-5 and 6-6 show the PTP positioning performance comparison between the original PTP NCTF controller and the Continuous Motion NCTF controller. As expected, the performance is identical in both PTP and Continuous Motion NCTF controllers.

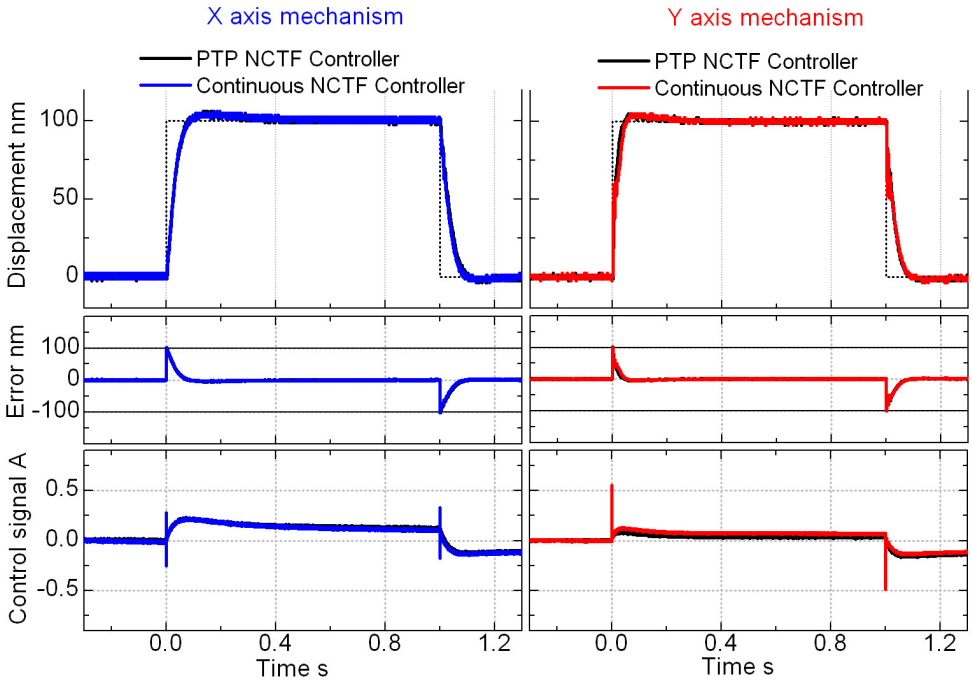

Figure 6-5. Comparison between the PTP and Continuous Motion NCTF controllers for PTP positioning with a 100 nm step input reference.

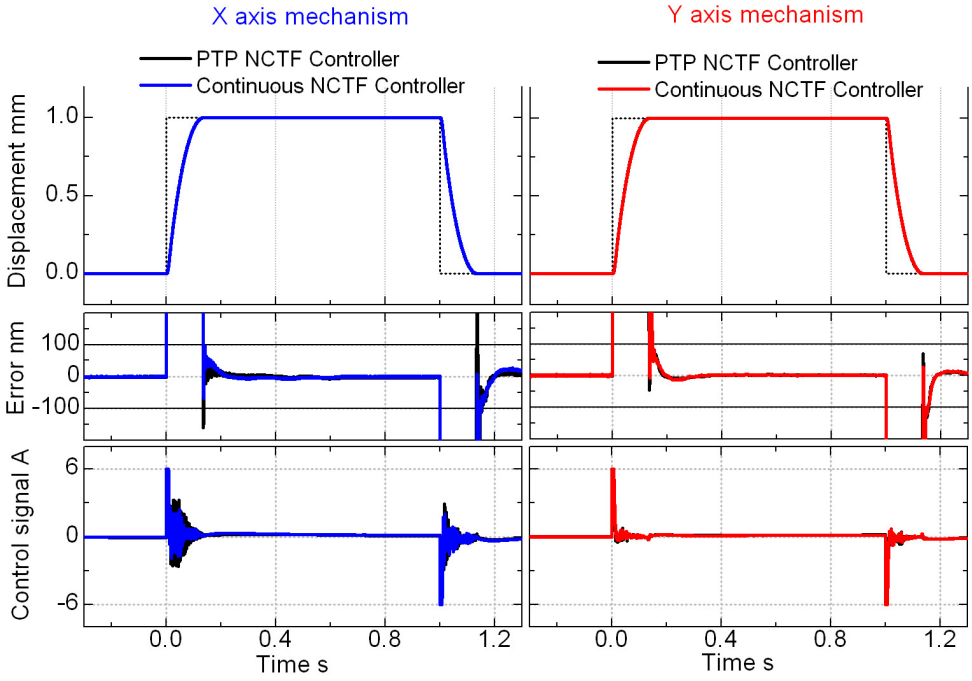

Figure 6-6. Comparison between the PTP and Continuous Motion NCTF controllers for PTP positioning with a 1 mm step input reference.

Figures 6-7 and 6-8 show the continuous motion performance of the PTP and Continuous Motion NCTF controller, respectively. The reference used is a circle radius of 5 mm and peripheral velocity of 15.708 mm/s (frequency of 0.5 Hz). The same experiments were repeated twenty times and the average of the errors are shown in Table 6-1.

Table 6-1. PTP vs. Continuous Motion NCTF controller. Averaged values. (Figures 6-7 and 6-8)

Controller	$\max\|x_r - x\|$		$\max\|y_r - y\|$		Maximum radial error	
	Average (μm)	Standard deviation (μm)	Average (μm)	Standard deviation (μm)	Average (μm)	Standard deviation (μm)
PTP NCTF	855.362	0.308	853.154	0.085	206.435	0.141
Continuous Motion NCTF	4.468	0.230	1.626	0.108	3.891	0.191

As shown in Table 6-1, the differences in performance between the two controllers are very large. The radial error with the Continuous Motion NCTF controller is reduced by more than 50 times, proving the suitability of the proposed controller structure for continuous motion.

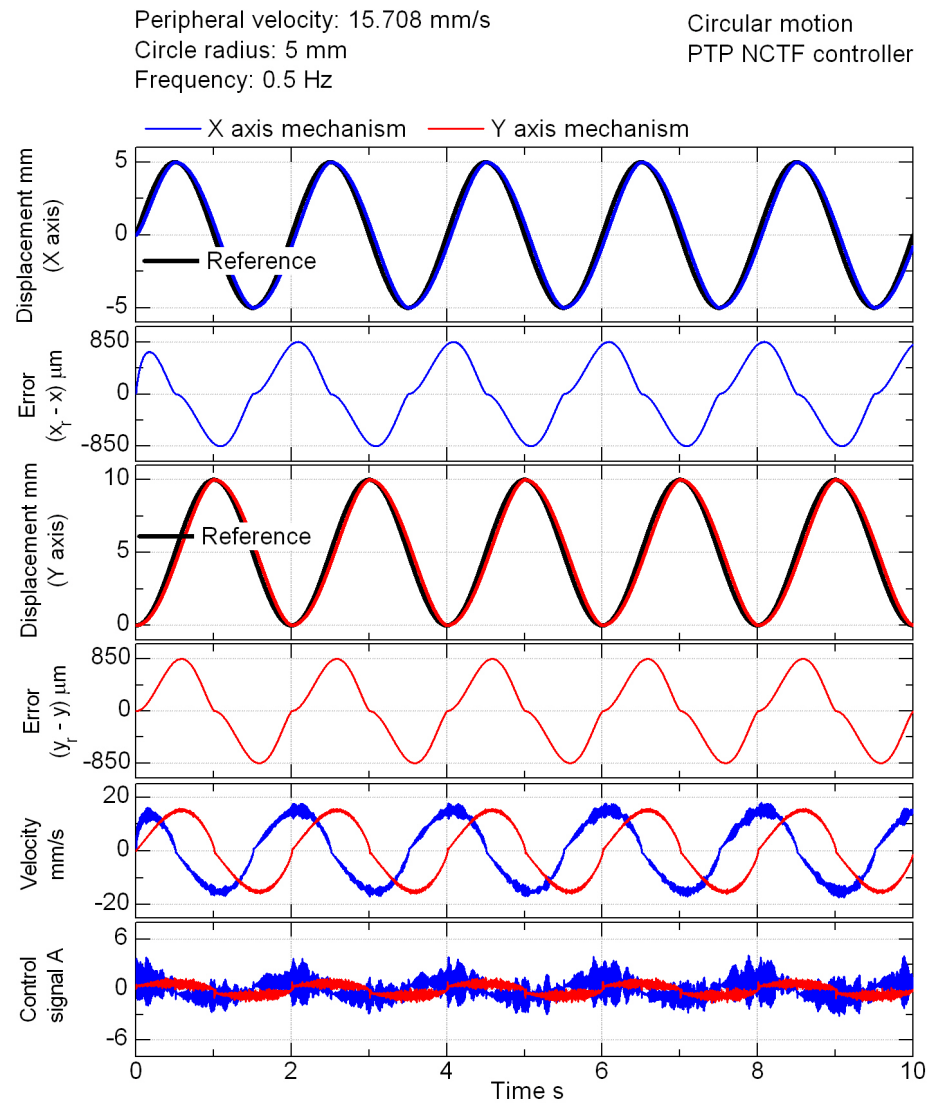

(a) Time response

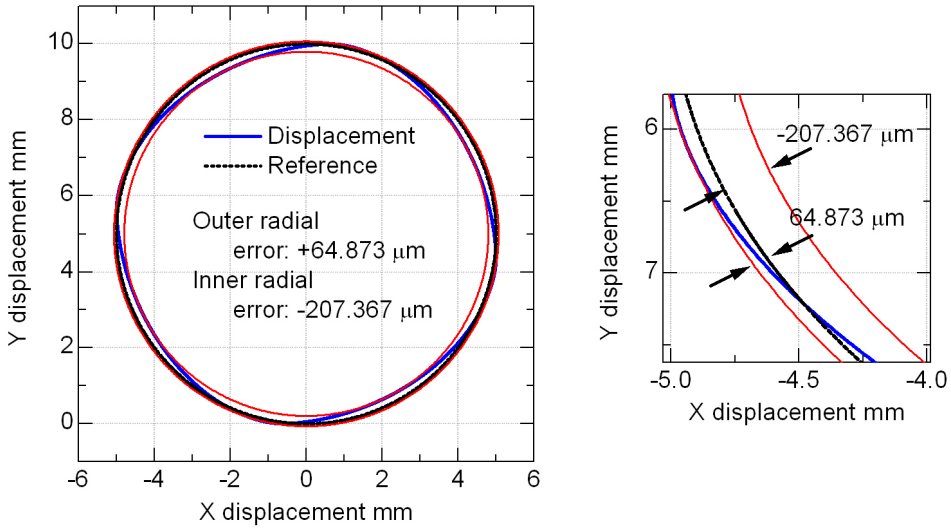

(b) Circular contour

Figure 6-7. PTP NCTF controller: radius of 5 mm and peripheral velocity of 15.708 mm/s.

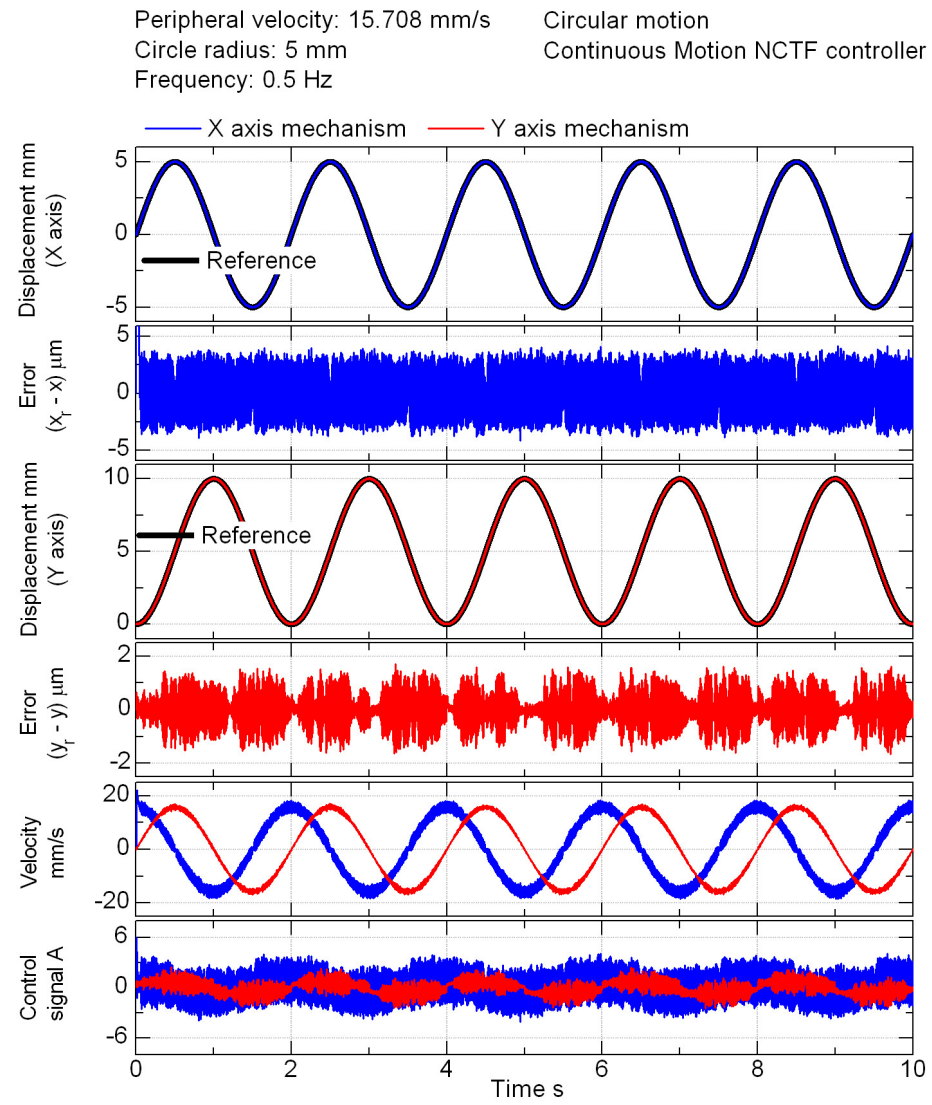

(a) Time response

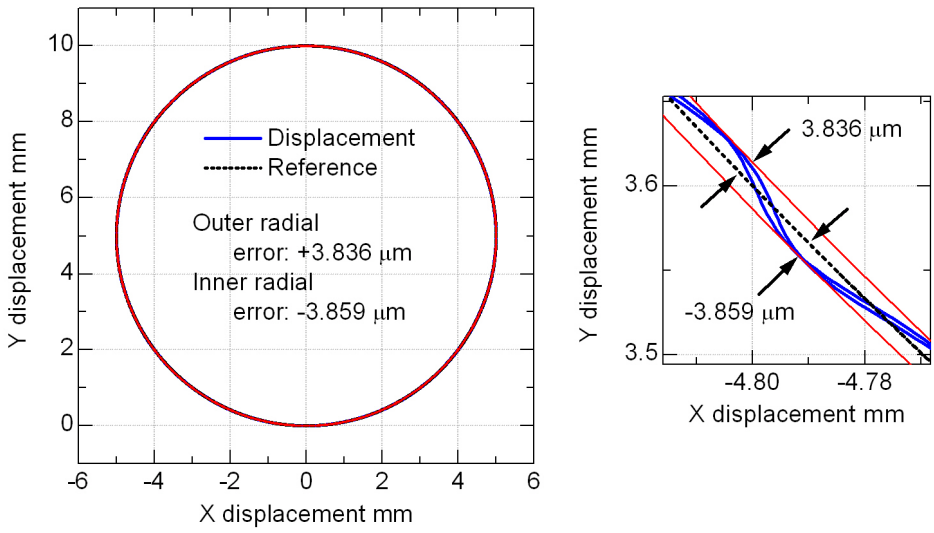

(b) Circular contour

Figure 6-8. Continuous Motion NCTF controller: radius of 5 mm and peripheral velocity of 15.708 mm/s.

6.3.3 Velocity of 31.416 mm/s. PI-D Controller vs. Continuous Motion NCTF Controller.

Figures 6-9 and 6-10 show a comparison between the PI-D and the Continuous Motion NCTF controller with a circular reference input of radius 5 mm and peripheral velocity of 31.416 mm/s (frequency of 1 Hz). The averaged errors of twenty experiments are summarized in Table 6-2. As Table 6-2 shows, the maximum radial error is more than six times lower with the Continuous Motion NCTF controller.

Table 6-2. PI-D vs. Continuous Motion NCTF. Averaged values of circular motion. (Figures 6-9 and 6-10)

Controller	$\max\|x_r - x\|$		$\max\|y_r - y\|$		Maximum radial error	
	Average (μm)	Standard deviation (μm)	Average (μm)	Standard deviation (μm)	Average (μm)	Standard deviation (μm)
PI-D	25.119	0.175	19.946	0.030	25.058	0.174
Continuous Motion NCTF	4.242	0.284	1.765	0.092	3.814	0.293

Figures 6-11 and 6-12 show a comparison between the PI-D and the Continuous Motion NCTF controller under a square reference input whose diagonal length is 10 mm and same velocity of the circular motion case. Notice from Figures 6-11(a) and 6-12(a) that the control signals saturate at 6 A. Averaged motion errors of twenty experiments are summarized in Table 6-3. The values in the table show that the PI-D has a slight better performance and more actuator saturation than the Continuous Motion NCTF controller. The errors of the X axis mechanism motion have negligible difference but on the Y axis mechanism the PI-D control system has 1.9 % less error. Trajectory overshoot of the PI-D control system is 1.6 % lower than that of the Continuous Motion NCTF control system. A possible reason is the presence of the derivative element of the PI-D controller, which has the effect of damping the mechanism motion, thus decreasing overshoot.

Table 6-3. PI-D vs. Continuous Motion NCTF. Averaged values of square motion. (Figures 6-11 and 6-12)

Controller	$\max\|x_r - x\|$		$\max\|y_r - y\|$		Trajectory overshoot	
	Average (μm)	Standard deviation (μm)	Average (μm)	Standard deviation (μm)	Average (μm)	Standard deviation (μm)
PI-D	530.111	15.372	539.185	3.512	539.930	7.548
Continuous Motion NCTF	530.877	20.796	549.266	9.412	548.723	5.654

In Figures 6-8 and 6-10, both experimental results come from the Continuous Motion NCTF controller. They have the same circle radius but the peripheral velocity differs by two times (15.708 mm/s in Figure 6-8 and 31.416 mm/s in Figure 6-10). Despite the differences in velocity, the errors are relatively similar.

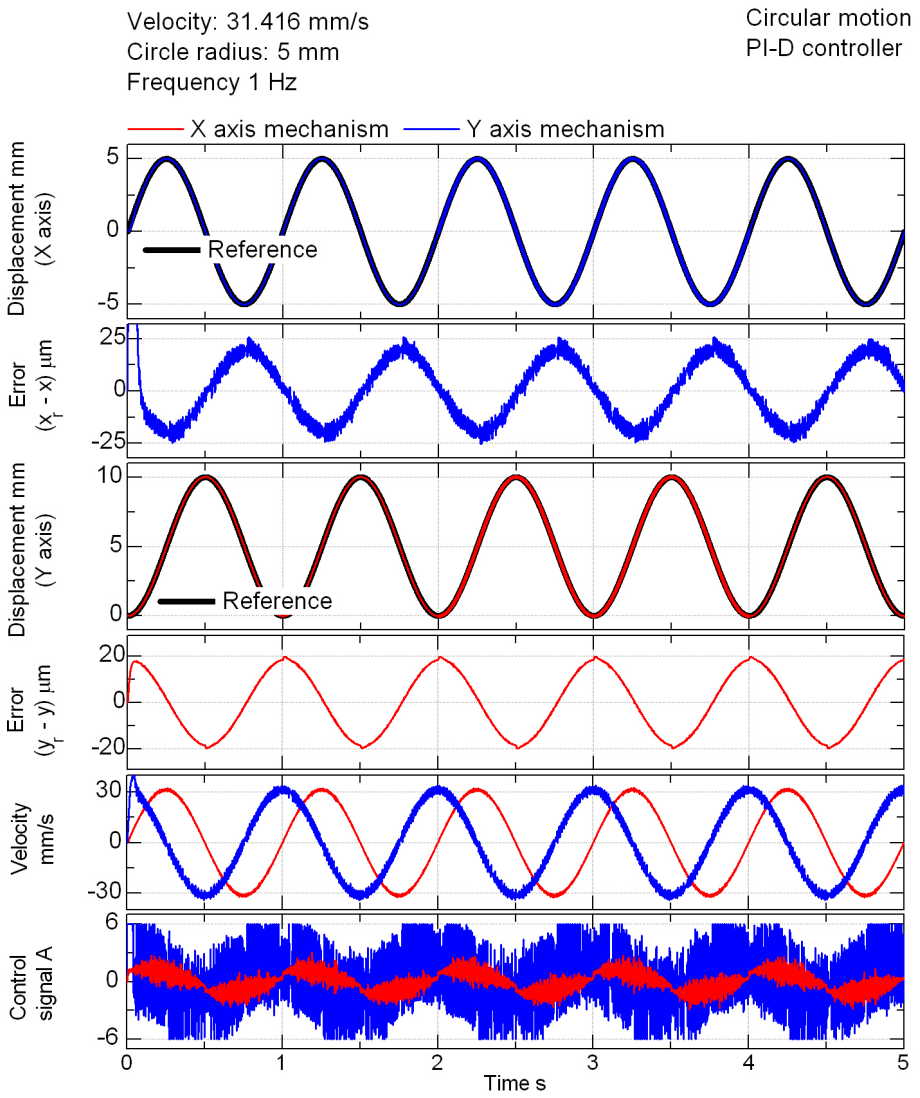

(a) Time response

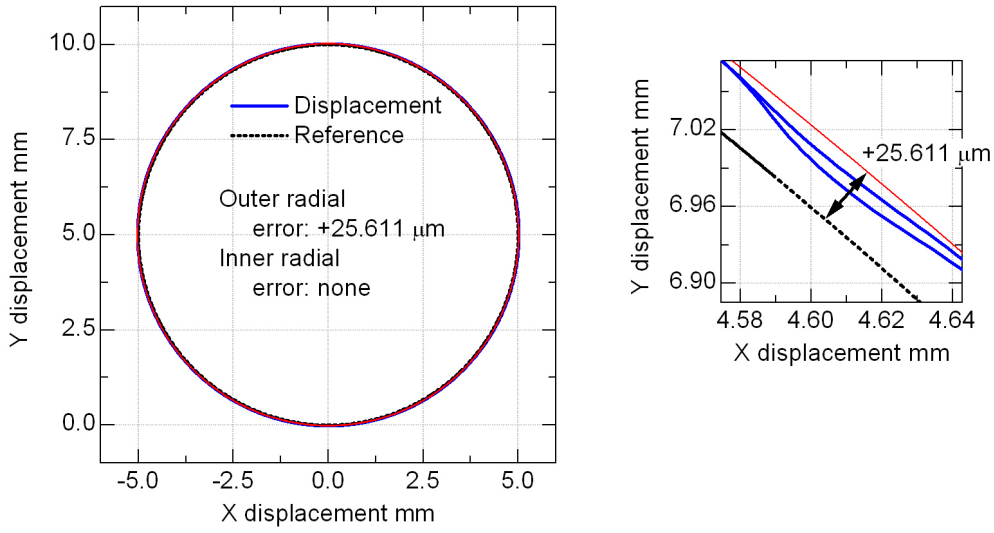

(b) Circular contour

Figure 6-9. PI-D controller: radius of 5mm and peripheral velocity of 31.416 mm/s.

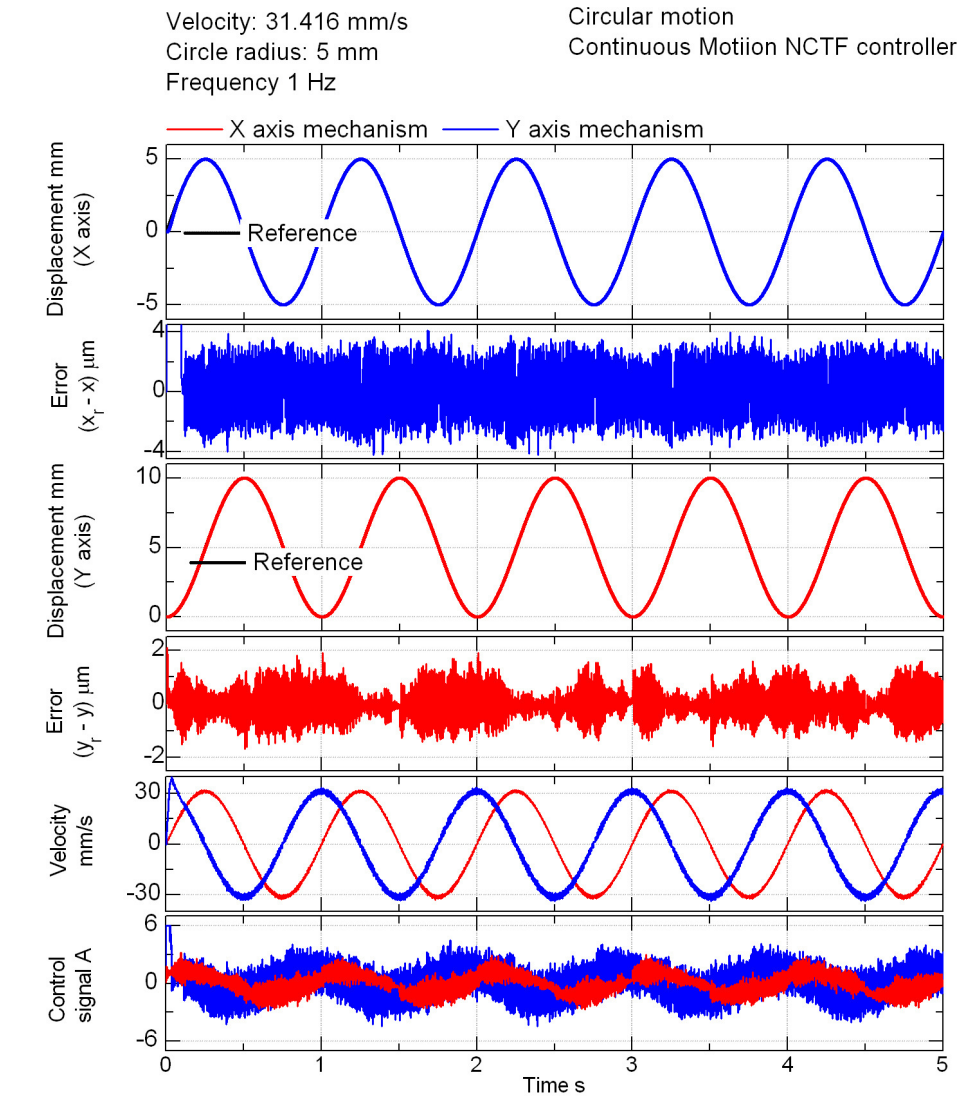

(a) Time response

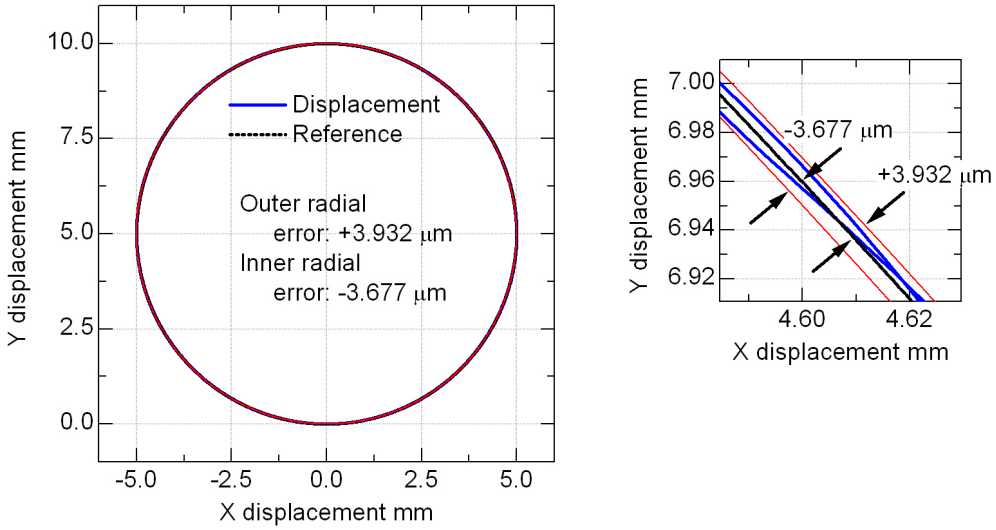

(b) Circular contour

Figure 6-10. Continuous Motion NCTF controller: radius of 5mm and peripheral velocity of 31.416 mm/s.

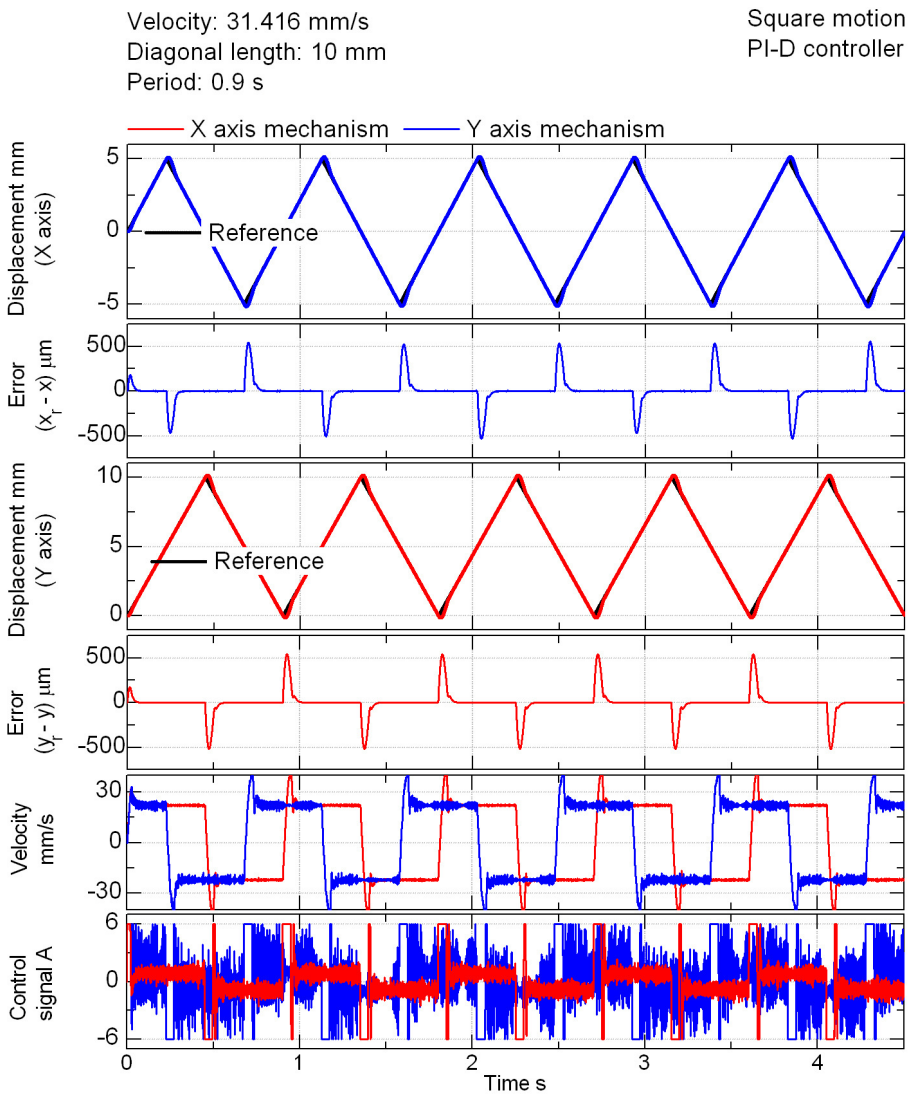

(a) Time response

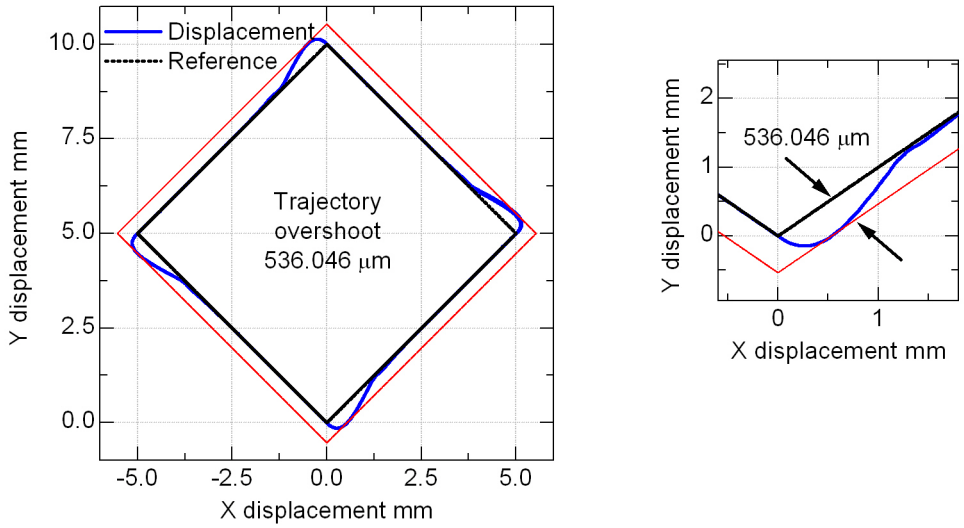

(b) Square contour

Figure 6-11. PI-D controller: diagonal length of 5mm and velocity of 31.416 mm/s.

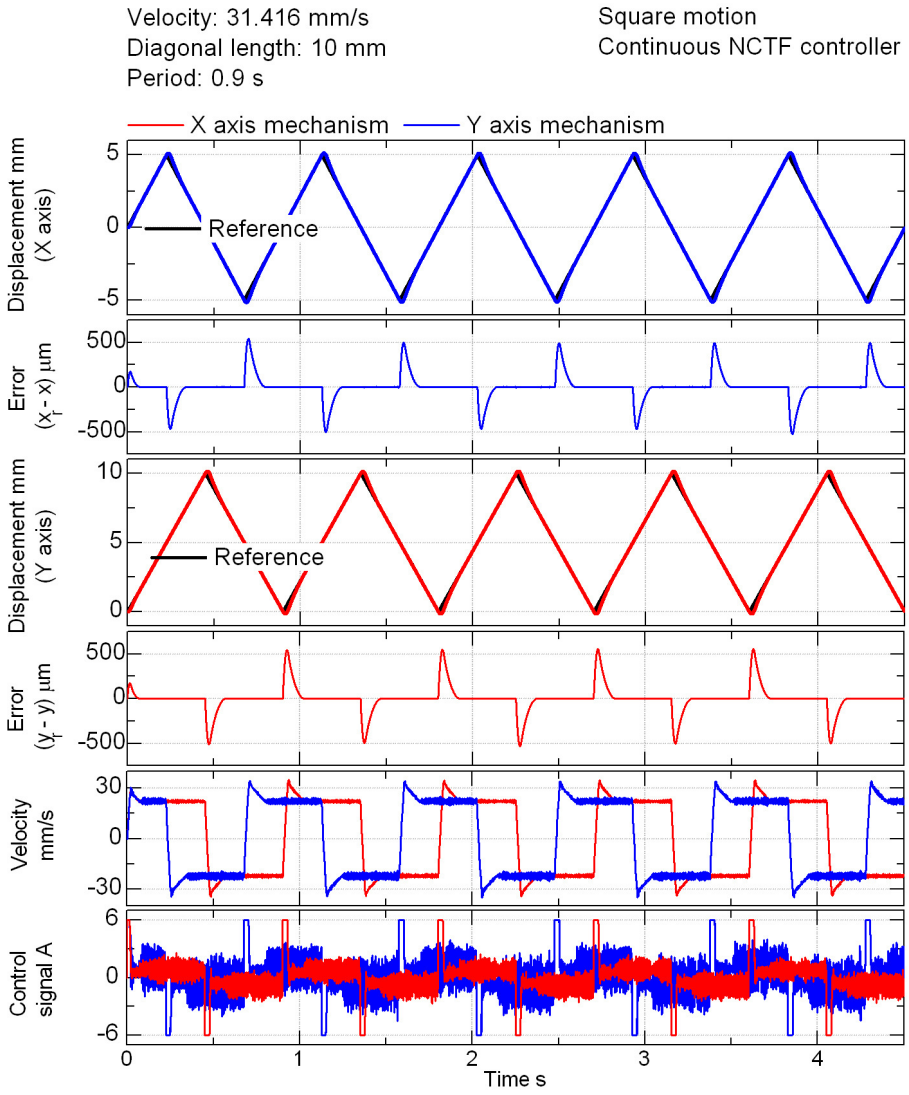

(a) Time response

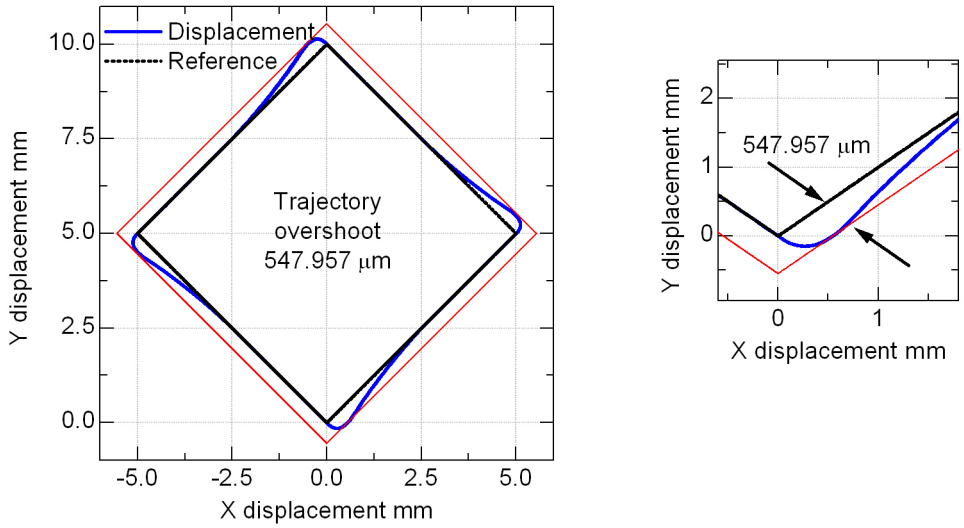

(b) Square contour

Figure 6-12. Continuous Motion NCTF controller: diagonal length of 5mm and velocity of 31.416 mm/s.

6.3.4 Velocity of 3.142 μm/s. PI-D Controller vs. Continuous Motion NCTF Controller.

Figures 6-13 and 6-14 show a comparison with a circular reference input of radius 1 μm and peripheral velocity of 3.142 μm/s (frequency of 0.5 Hz). It is easily seen from the PI-D response in Figure 6-13(b) that the maximum deviation occurs as protuberances around 30^0, 120^0, 210^0, and 300^0. The same tendency is observed with the Continuous Motion NCTF controller, and it seems to be attributed to the nonlinear friction of the mechanism [31]. The averaged errors are summarized in Table 6-4 and shows the superior performance of the Continuous Motion NCTF controller.

Table 6-4. PI-D vs. Continuous Motion NCTF. Averaged values of circular motion. (Figures 6-13 and 6-14)

Controller	$\max\|x_r - x\|$		$\max\|y_r - y\|$		Maximum radial error	
	Average (nm)	Standard deviation (nm)	Average (nm)	Standard deviation (nm)	Average (nm)	Standard deviation (nm)
PI-D	178.1	1.9	120.9	9.6	126.7	1.6
Continuous Motion NCTF	48.5	4.1	34.4	5.3	43.6	3.9

Figures 6-15 and 6-16 show the square motion with the same velocity of the circular motion case. From the summarized errors in Table 6-5, it is clearly seen that the Continuous Motion NCTF controller has better motion accuracy than the PI-D controller. The averaged errors of the Continuous Motion NCTF controller are around three times lower than those of the PI-D controller.

Table 6-5. PI-D vs. Continuous Motion NCTF. Averaged values of square motion. (Figures 6-15 and 6-16)

Controller	$\max\|x_r - x\|$		$\max\|y_r - y\|$		Trajectory overshoot	
	Average (nm)	Standard deviation (nm)	Average (nm)	Standard deviation (nm)	Average (nm)	Standard deviation (nm)
PI-D	266.0	3.2	204.7	3.9	237.8	4.4
Continuous Motion NCTF	88.7	3.6	79.5	3.7	87.7	3.5

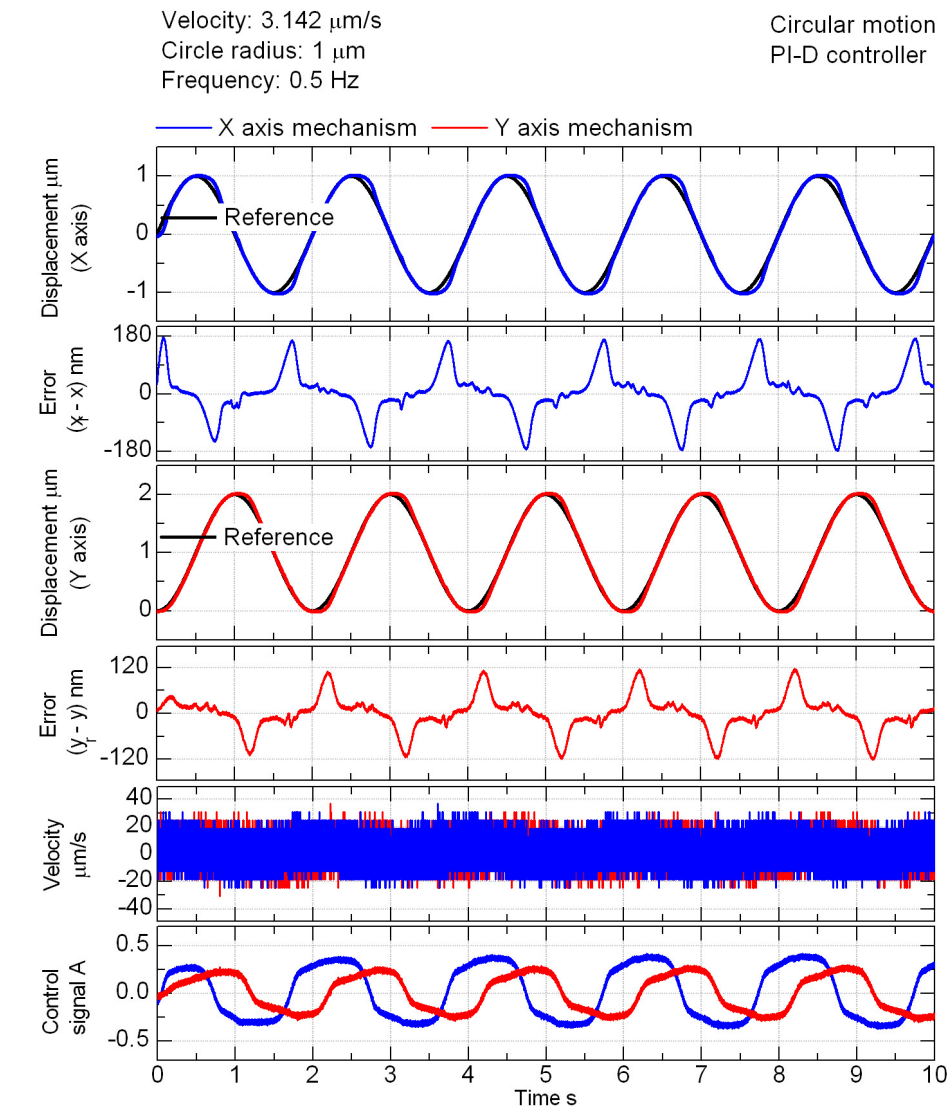

(a) Time response

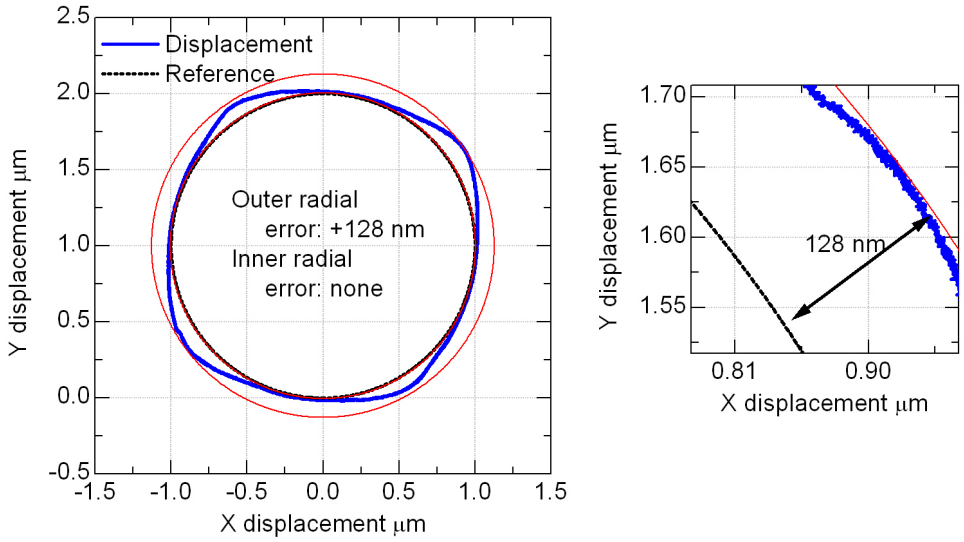

(b) Circular contour

Figure 6-13. PI-D controller: radius of 1 μm and peripheral velocity of 3.142 μm/s.

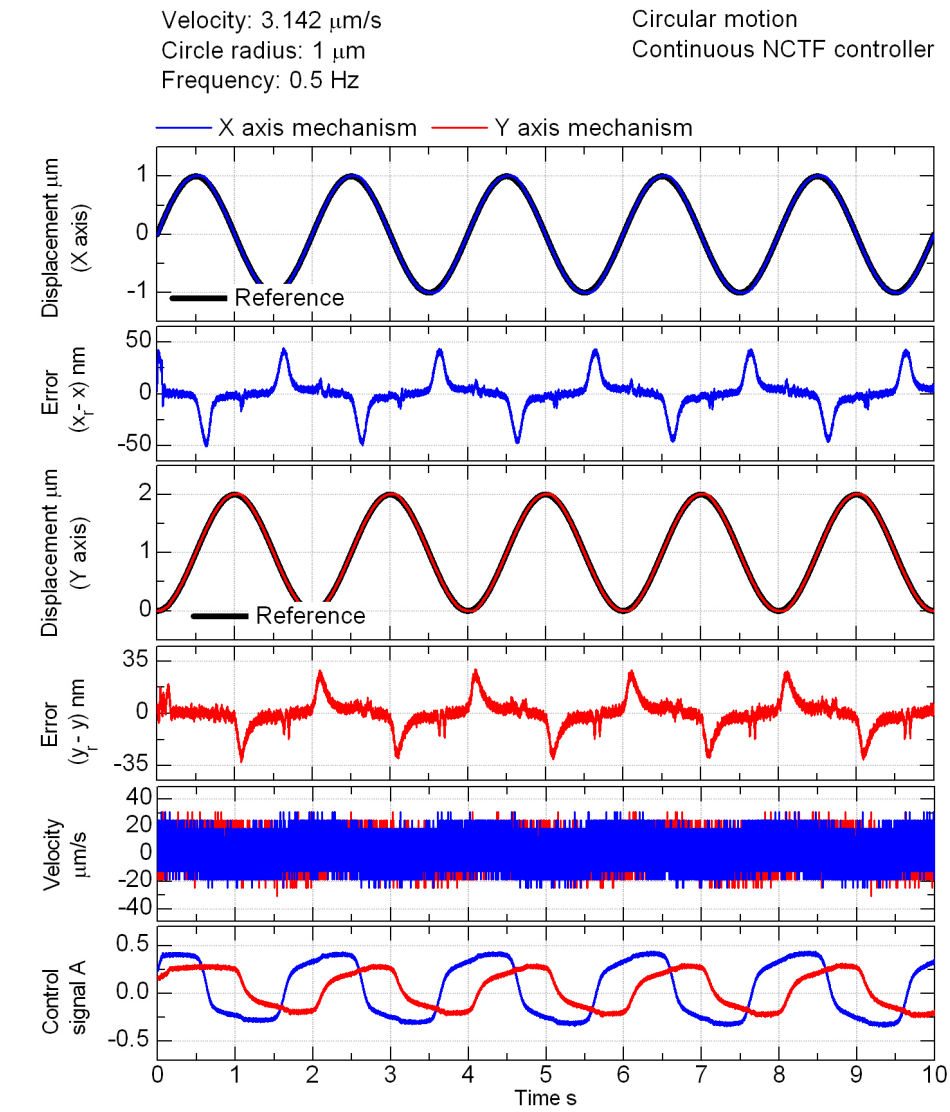

(a) Time response

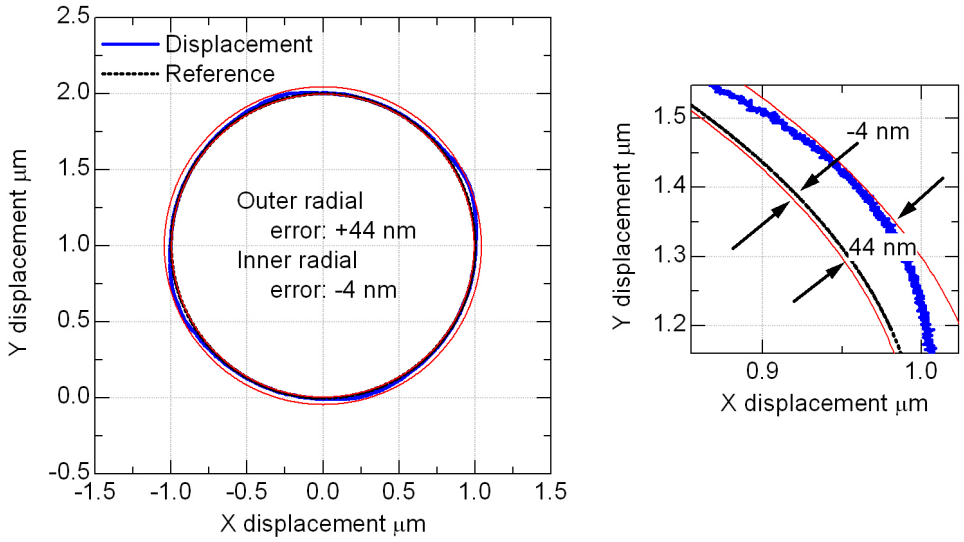

(b) Circular contour

Figure 6-14. Continuous Motion NCTF controller: radius of 1 μm and peripheral velocity of 3.142 μm/s.

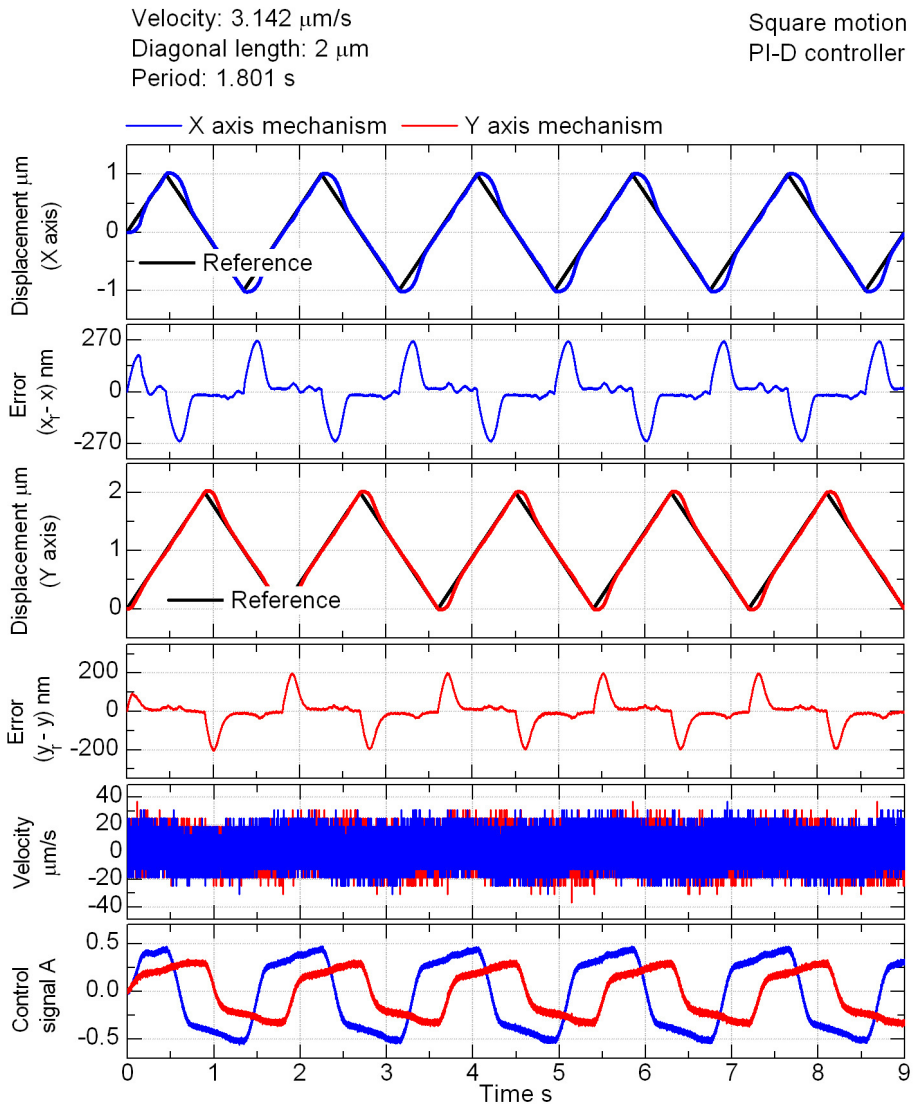

(a) Time response

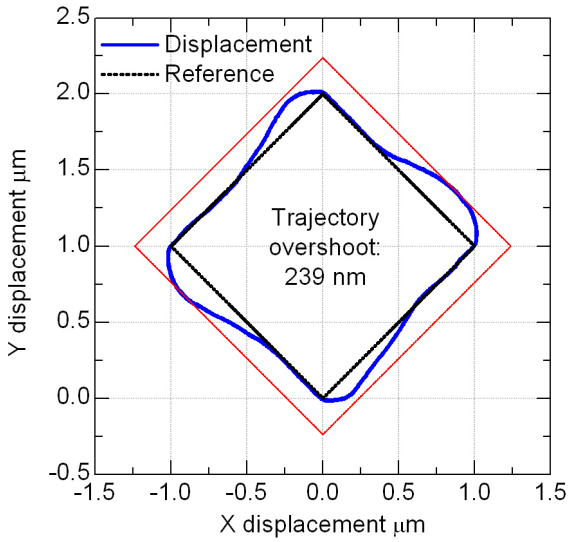

(b) Square contour

Figure 6-15. PI-D controller: diagonal length of 2 μm and velocity of 3.142 μm/s.

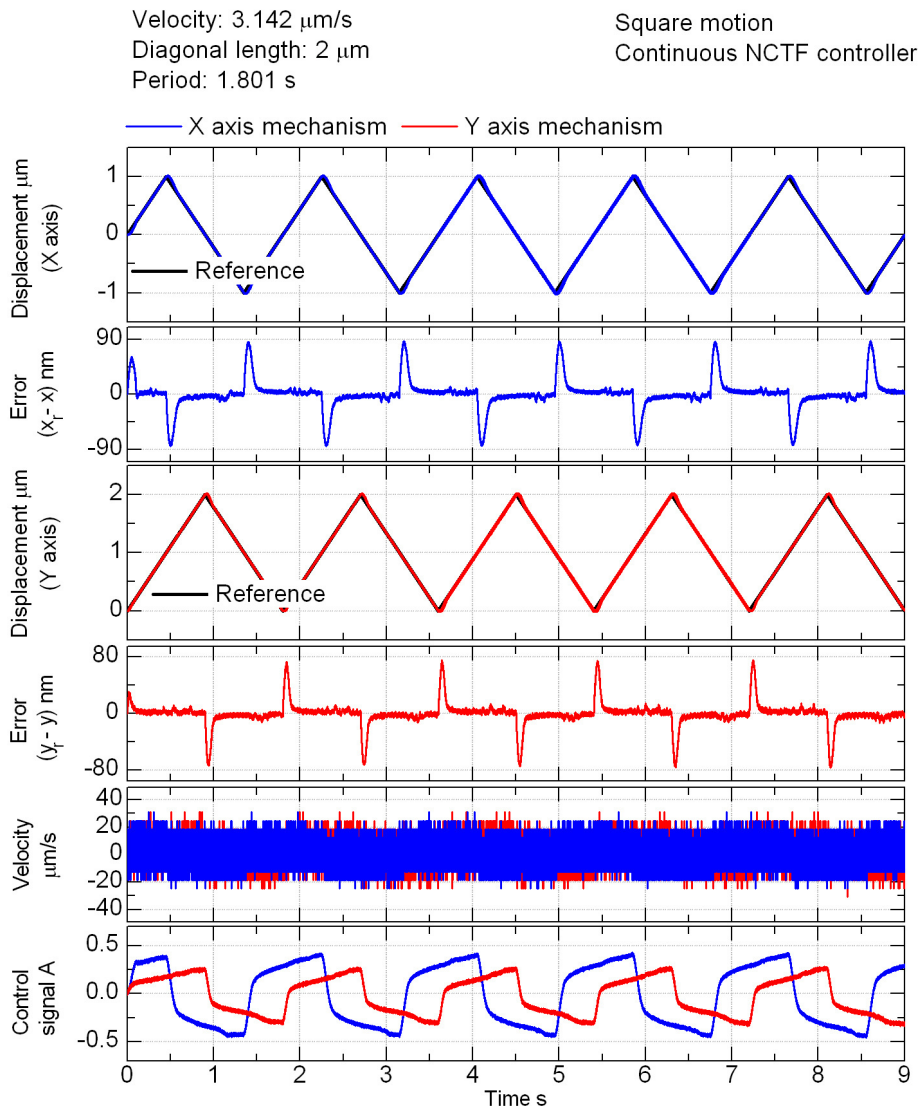

(a) Time response

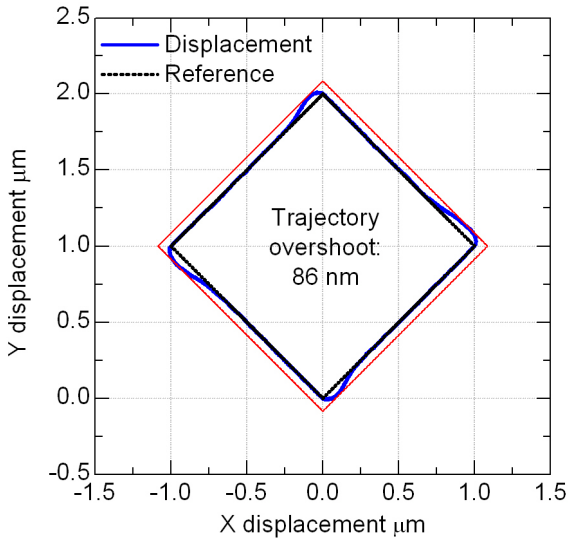

(b) Square contour

Figure 6-16. Continuous Motion NCTF controller: diagonal length of 2 μm and velocity of 3.142 μm/s.

6.3.5 Additional Experiments with the Continuous Motion NCTF Controller

As commented in subsection 6.3.3, Figures 6-8 and 6-10 show that a difference in velocity of two times has little effect in positioning characteristics of the Continuous Motion NCTF controller. In the next experiments, the effect of the motion frequency on positioning performance is evaluated.

A fixed velocity of 3.142 μm/s is used. Figure 6-17 shows the circular motion response of the Continuous Motion NCTF control with a radius of 5 μm and frequency of 0.1 Hz. Figure 6-18 shows the circular motion with a radius of 100 nm and frequency of 5 Hz. The averaged error measurements are summarized in Table 6-6. The results from Figure 6-14 (radius of 1 μm and frequency of 0.5 Hz) are also included in Table 6-6 for the sake of comparison. As the table shows, errors in both X and Y axis mechanisms increase as the frequency of motion increases. Comparing the results of the reference of 0.1 Hz (5 μm) and 0.5 Hz (1 μm), it is observed that the error increases despite of the same peripheral velocity. In the case of the 100 nm radius, the frequency of 5 Hz is higher than the bandwidth of the control system (refer to Figure 4-9(a)) and contour deviation (Figure 6-18 (b)) is visibly large. Therefore, the frequency of the sinusoidal reference affects the positioning performance more than the velocity of the mechanism motion.

Table 6-6. Continuous Motion NCTF controller. Velocity of 3.142 μm/s and different frequencies (Figures 6-14, 6-17, and 6-18)

Frequency of the sinusoidal reference (Radius of motion)	$\max\|x_r - x\|$		$\max\|y_r - y\|$		Maximum radial error	
	Average (nm)	Standard deviation (nm)	Average (nm)	Standard deviation (nm)	Average (nm)	Standard deviation (nm)
0.1 Hz (5 μm)	19.8	1.0	18.7	1.8	20.1	1.3
0.5 Hz (1 μm)	48.5	4.1	34.4	5.3	43.6	3.9
5 Hz (100 nm)	107.1	6.4	66.6	18.8	43.4	8.3

Finally, Figure 6-19 shows a circular motion of 100 nm and velocity of 0.157 μm/s (frequency of 0.25 Hz). By decreasing the frequency of the circular motion, positioning performance improves and ultra-precision motion control is achieved. This experiment confirms that the Continuous Motion NCTF controller is an ultra-precision controller, not only for PTP positioning but also for continuous motion control.

Table 6-7. Continuous Motion NCTF controller. Ultra-precision positioning (Figure 6-19)

Radius of circular motion	$\max\|x_r - x\|$		$\max\|y_r - y\|$		Maximum radial error	
	Average (nm)	Standard deviation (nm)	Average (nm)	Standard deviation (nm)	Average (nm)	Standard deviation (nm)
100 nm	10.5	1.0	9.7	1.4	10.0	1.0

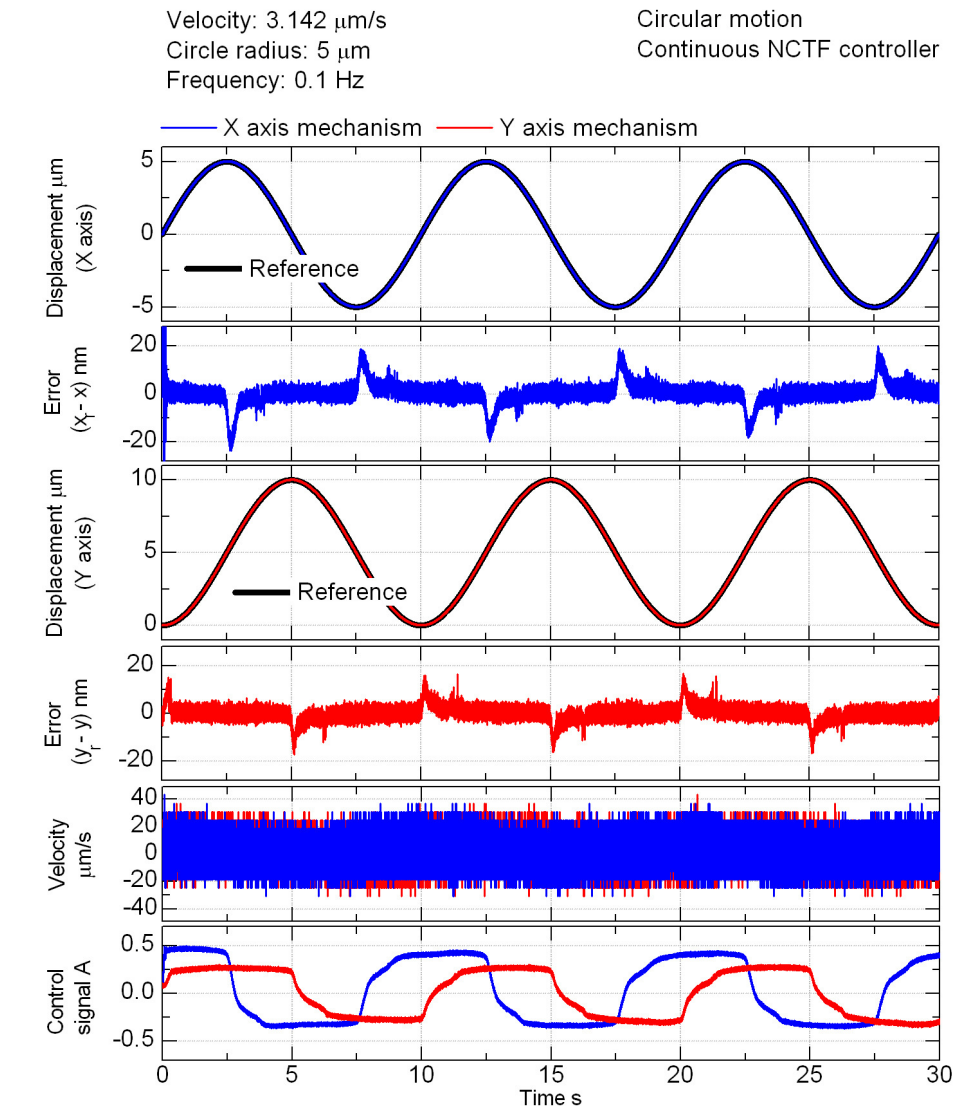

(a) Time response

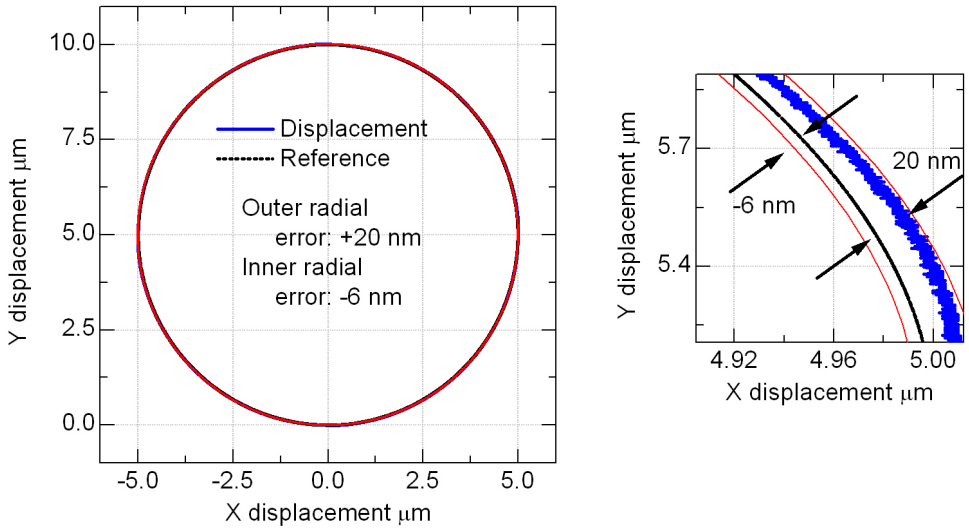

(b) Circular contour

Figure 6-17. Continuous Motion NCTF controller: radius of 5 μm and peripheral velocity of 3.142 μm/s.

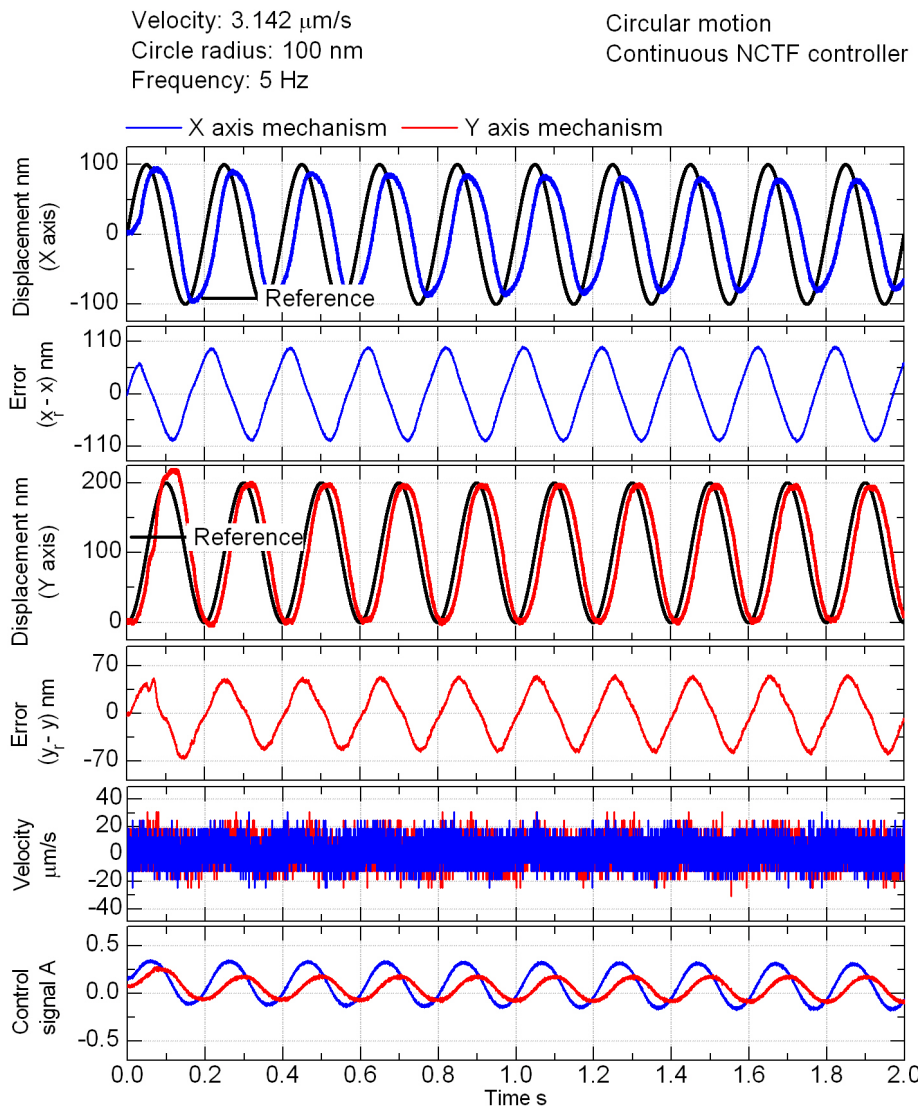

(a) Time response

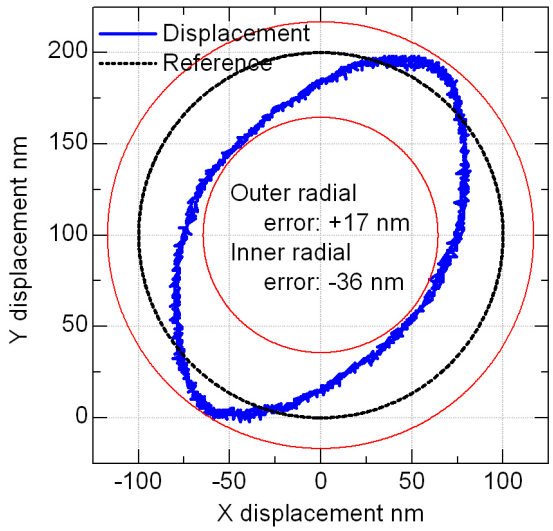

(b) Circular contour

Figure 6-18. Continuous Motion NCTF controller: radius of 100 nm and peripheral velocity of 3.142 μm/s.

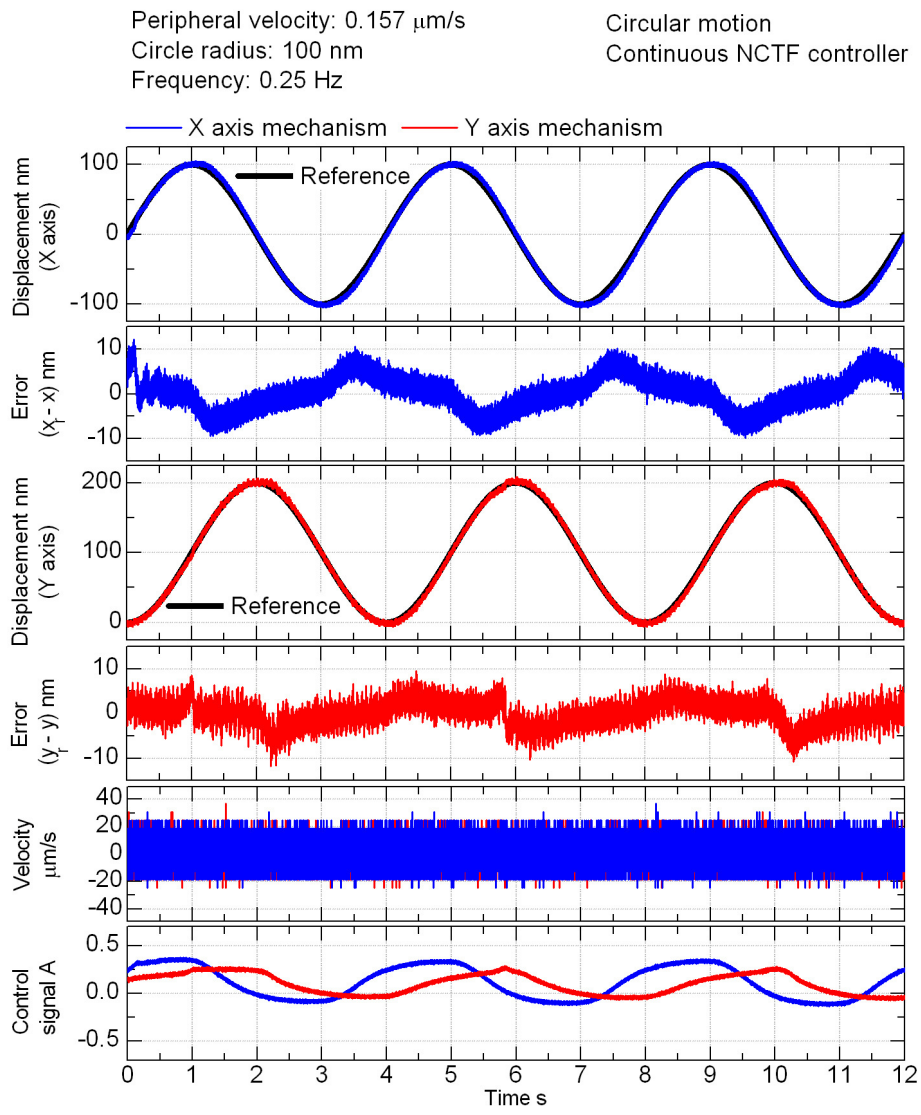

(a) Time response

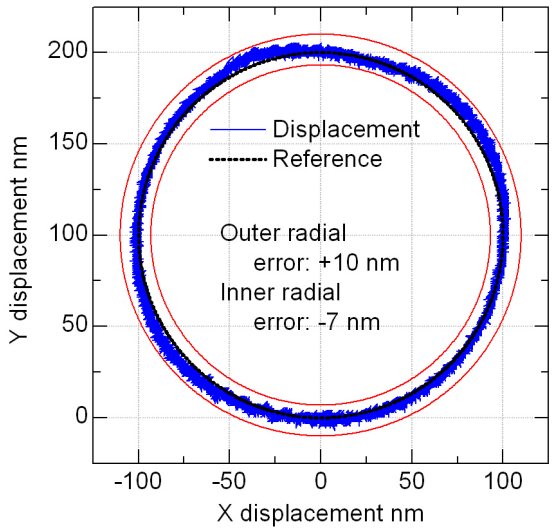

(b) Circular contour

Figure 6-19. Continuous Motion NCTF controller: radius of 100 nm and peripheral velocity of 0.157 μm/s.

CHAPTER 7 - EXTENSION OF THE NCTF CONTROLLER DESIGN METHOD

The purpose of this section is to examine the applicability of the NCTF controller design method – which means the procedure for the determination of the controller parameters – to another cases, different from the case described in Chapter 3. As the first case, an approximately pure inertia mechanism, which is a characteristic of friction free mechanisms, is considered. In the second case, a mechanism with large variation of Coulomb friction is evaluated. In the third case, different inclinations of the NCT are considered, which is useful if the designer wants to modify the NCT close to the origin.

For the three cases, the design procedure of the controller is the same as the one used for the actual mechanism, and described in Subsection 3.1.6. Briefly, the procedure consists in the construction of the NCT from an open-loop experiment and the determination of the parameters α and K. The practical stability limit is found by driving the mechanism with the proportional controller. The NCTF control stability limit is obtained by fixing a value of $\omega_n T$ and increasing ζ until instability is reached (with the compensator using the proportional and integral gains). The practical stability limit and the NCTF control stability limit are then compared. A close approximation of both stability limits proves that the design procedure is applicable.

For the first and second cases, the analyses are based on simulated results, since they are related to large variation of friction parameters, which is impossible to achieve with the real mechanism. In the third case, the analysis is based on experimental results.

7.1. CASE 1: CONTROLLER DESIGN UNDER DIFFERENT DAMPING CONDITIONS

The system in Figure 7-1 is used for simulations. This system allows the examination of the effects of damping variation. The object does not include nonlinear

friction. The subscripts "*c*" and "*obj*" refer to the controller and object (mechanism) parameters, respectively. The parameters α_c and K are the same ones used with the actual ballscrew mechanism (α_c = 505 s^{-1} and K = 32.3 mm/As). Four different damping values (α_{obj}) are examined:

. $\alpha_{obj,1}$ = 0.001 s^{-1} (approximately a pure inertia mechanism)

. $\alpha_{obj,2}$ = 250 s^{-1}

. $\alpha_{obj,3}$ = 505 s^{-1}

. $\alpha_{obj,4}$ = 750 s^{-1}

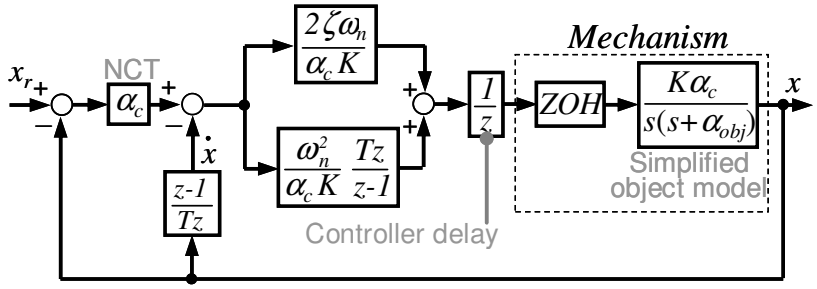

Figure 7-1. Sampled-data system used to evaluate the design procedure when α_{obj} changes.

The NCTF control stability limit is evaluated at the values $\omega_n T$ = 0.02, 0.1, 0.25, and 0.4 rad. The results in Figure 7-2 show that the practical stability limit for each damping condition approaches relatively close to the NCTF control stability limit. The average error of approximation between the practical stability limit and the NCTF control stability is 10 %. The difference between the stabilities is caused by the integral element of the NCTF controller. The integral element reduces the ultimate values of ζ. Therefore, it is recommended the use of a margin of safety (at least 10 % in this case) so that the NCTF control is designed under the safety area of the practical stability limit.

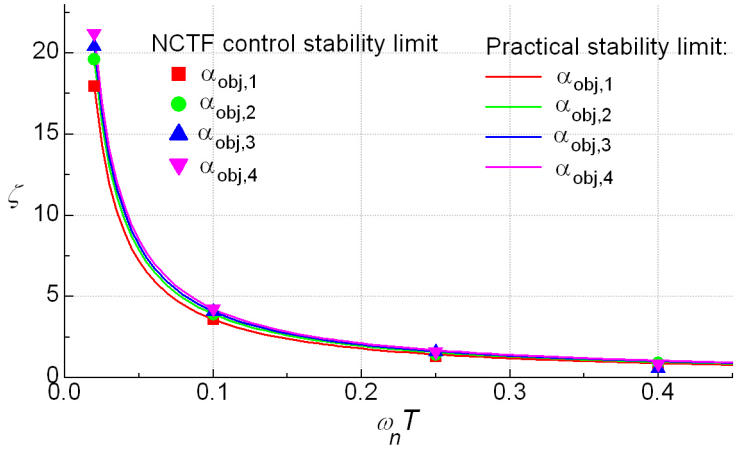

Figure 7-2. Practical stability limits under different damping conditions.

Fortunately, the NCTF control achieves good positioning characteristics at values much lower than ζ_{prac}. As an example, Figure 7-3 shows the simulated results of four control systems designed using the system in Figure 7-1. The object with $\alpha_{obj,4}$ was used and the value of $\omega_n T$ was fixed to 0.25 rad. Step inputs of 1 μm were used. The values of ζ were changed by different margins of safety. It is observed that for a good performance, the margins of safety should be larger than 30 %.

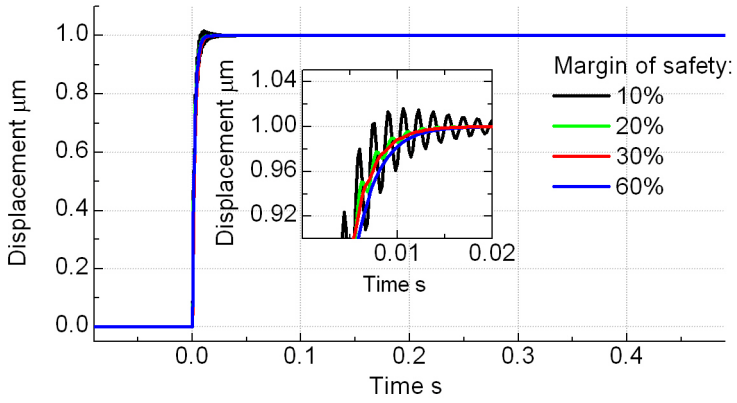

Figure 7-3. Effects of the margin of safety on relation to the control performance.

In the case of the ballscrew mechanism, Figure 3-7 shows that the optimum curve for the design of the controller is 60 % lower than ζ_{prac} (smaller values of margin of safety tend to deteriorate the performance). Therefore, as a practical rule, a margin of safety for the design is at least 30%. This value not only compensates approximation errors, but also indicates the region where the control performance is acceptable.

The practical stability limit can be used (considering a margin of safety) for mechanisms with different damping values, even if its variation is large. The result of the condition represented by $\alpha_{obj,1}$ is especially interesting, because it is an indication that ζ_{prac} is usable for friction free mechanisms.

7.2. CASE 2: CONTROLLER DESIGN UNDER DIFFERENT COULOMB FRICTION

In the second case, the nonlinear model of the mechanism in Figure 2-3(b) is used for simulations. The characteristic of the mechanism model is changed by setting different Coulomb friction values. Variation of Coulomb friction value occurs often, due to payload variation and lubrication condition; thus it is important to examine the feasibility of the practical stability limit in such case. The mechanism model is driven in closed-loop with the NCTF controller in order to find the practical stability limit and the NCTF control stability limit. Four Coulomb friction values (T_{fmax}) are examined:

.$T_{fmax,1}$ = 0 Nm
.$T_{fmax,2}$ = 0.023 Nm
.$T_{fmax,3}$ = 0.046 Nm (actual value of the leadscrew mechanism)
.$T_{fmax,4}$ = 0.138 Nm

The NCTF control stability limit is evaluated at the values $\omega_n T$ = 0.02, 0.05, 0.1, 18 0.2, 0.3, and 0.4 rad for the mechanism with $T_{fmax,3}$, and at the points $\omega_n T$ = 0.02, 0.1, 0.25 and 0.4 rad for the other cases.

The results in Figure 7-4 show the practical stability limit for each friction condition, as well as the markers representing the NCTF control stability. The average error of approximation in this case is 16 %. The error of approximation shows that the practical stability limit is useful as an indicator for the choice of the compensator gains. It does not exactly predict the boundary between the unstable and stable regions, but it certainly guarantees the stable gains are below ζ_{prac}, which greatly helps the designer

during the choice of the compensator gains. Thus, the practical stability limit is useful as an indicator for the NCTF controller design for mechanisms subjected to large Coulomb friction variation.

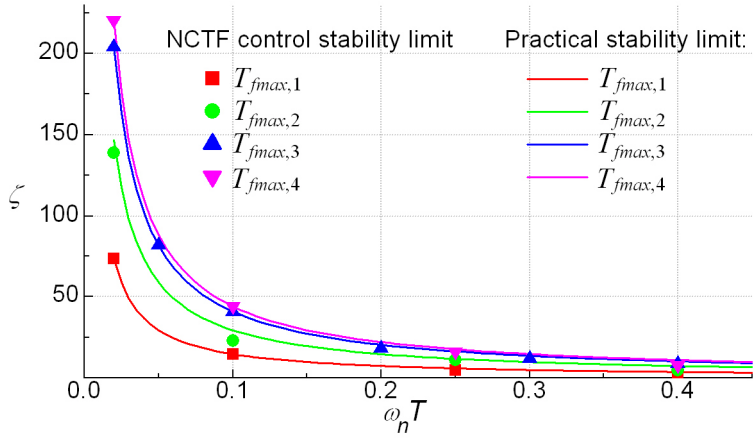

Figure 7-4. Practical stability limits under different Coulomb friction.

7.3. CASE 3: CONTROLLER DESIGN UNDER DIFFERENT NCT'S INCLINATIONS

In the third case, the inclination of the NCT close to the origin is changed. It is important to consider different inclinations of the NCT because the designer may want to modify the NCT in order to achieve better performance. The procedure explained in subsection 3.1.6 is repeated using the actual mechanism and different NCT's inclinations. The practical stability limit (ζ_{prac}) and the NCTF control stability limit are found experimentally and compared. Four NCT's inclinations (α_c) are examined:

.$\alpha_{c,1}$ = 250 s^{-1}

.$\alpha_{c,2}$ = 505 s^{-1} (original inclination)

.$\alpha_{c,3}$= 750 s^{-1}

.$\alpha_{c,4}$= 1010 s^{-1}

The NCTF control stability limit is evaluated at the values $\omega_n T$ = 0.02, 0.05, 0.1, 0.2, 0.3, and 0.4 rad for the controller with $\alpha_{c,2}$ and at the values $\omega_n T$ = 0.02, 0.1, 0.25 and 0.4 rad for the other cases.

As it can be observed from Figure 7-5, the curves of the practical stability limit fits relatively close to the NCTF control stability limit. The approximation error in this case is of only 6 %. These results prove that practical stability limit is feasible when the NCTF controller is used with different NCT's inclinations, thus allowing the designer to modify the NCT if necessary.

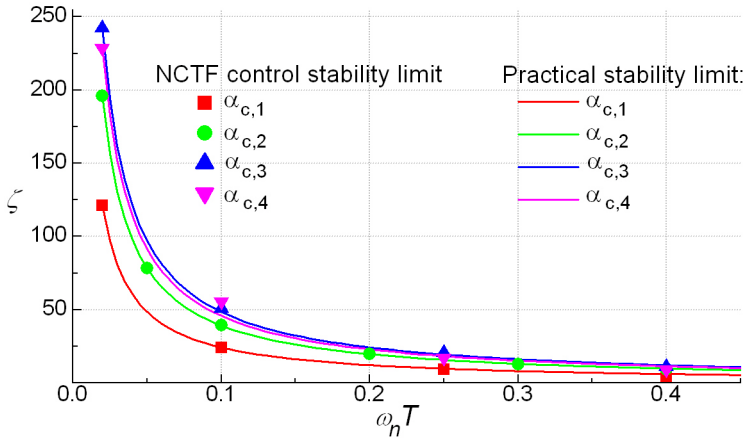

Figure 7-5. Practical stability limits using different inclinations of the NCT.

It is important to notice that, for the three cases considered, the NCTF controller design procedure was the same as the one described in Subsection 3.1.6. Therefore, the procedure for the controller parameter determination does not change. The same controller design procedure can be applied when: (1) the damping values change largely (including the case in which the mechanism is approximately a pure inertia mechanism), (2) Coulomb friction values change largely, and (3) different inclinations of the NCT are used.

CHAPTER 8 – CONCLUSIONS AND FUTURE WORKS

8.1. CONCLUSIONS

In this research, the NCTF control method was applied to a leadscrew mechanism achieving ultra-precision positioning. Under the lightweight condition, the controller was designed without any exact identification of parameters or modeling. The practical stability limit was used to restrict the choice of the design parameters ζ and $\omega_n T$ within the stable area. The designed control system achieves positioning accuracy of nanometers by using large integral values, which also causes excessive overshoot. The overshoot was reduced by using an antiwindup integrator which is easy to design. PTP positioning performance from 100 nm to 20 mm was evaluated. Accuracy better than 10 nm was achieved in all the cases. The positioning resolution of the control system is 5 nm even when friction changes.

Under the heavyweight condition, the mechanism presents residual vibration, which deteriorates the positioning accuracy. The conditional notch filter is robust to the frequency variation of residual vibration. The design is easy, requiring only a step input in open-loop. With the use of the conditional notch filter, the performance of the control system under the heavyweight condition achieves the same positioning accuracy and resolution as the mechanism under the lightweight condition. The results prove the high robustness of the NCTF controller with the conditional notch filter to payload variation. The payload is 4.9 times higher on the X axis mechanism than on the Y axis mechanism. Also, high robustness to friction variation is verified (two times larger in the X axis mechanism).

For fast PTP positioning, the procedure for the construction of the NCT was modified. The new phase-plane trajectory, named MFNCTS, has a profile that is similar to the MFNCT [28] when the mechanism motion is far from the origin (error larger than 1 mm). When the mechanism is close to the origin, the MFNCTS has a profile similar to the NCT, which is useful to avoid overshoot. From the averaged results of step inputs of 1,

10, and 20 mm, rise time and positioning time reduced respectively by 32% and 26% under the heavyweight condition. Under the lightweight condition, rise time and positioning time reduced respectively by 32% and 31%. In both payload conditions, overshoot did not change significantly (compared to the conventional NCT).

Continuous motion control is achieved by a minimum modification in the controller structure of the original NCTF controller used for PTP positioning. The proposed Continuous Motion NCTF controller has the same control law of the PTP NCTF controller when the reference rate is zero, thus it is usable for PTP positioning as well. The proposed controller shows superior performance when compared to a PI-D controller. Ultra-precision positioning accuracy is achieved at low velocities.

Finally, it was also shown in this research that the NCTF controller design procedure is feasible for three additional cases: (1) when the damping of the mechanism changes, (2) when the Coulomb friction of the mechanism changes, and (3) when the inclination of the NCT changes.

8.2. FUTURE WORKS

8.2.1 Improvement of Fast Point-to-Point Positioning for Short Steps

As shown in Figure 5-6, for short step inputs like 100 μm, the proposed NCTF controller with the MFNCTS improves the rise time without increasing overshoot. However, positioning time was not reduced significantly (in comparison with the conventional NCT). This is a limitation of the method caused by the similar profile between the MFNCTS and the conventional NCT close to the origin. Thus, it is desired the improvement of the method to achieve shorter positioning time for short step inputs (less than 1 mm).

8.2.2 Ultra-Precision Continuous Motion Control at Higher Velocities

As shown in Figure 6-19, the proposed Continuous Motion NCTF controller achieves circular motion with error of 10 nm at low velocity experiments. However, high speed is important not only in PTP but also continuous motion. Therefore, continuous motion control should be improved to achieve higher velocities while keeping the error less than 10 nm. In order to do so, the modification of the conventional NCT to a different profile could be examined. Also, the proposed solution aimed to not increase the complexity of the controller structure. Thus, no additional elements were included. However, the addition of a feedforward compensator may be considered. Feedforward techniques are usually effective in improving reference tracking performances.

APPENDIX - FAST FRICTION MEASUREMENT METHOD

In this research, the consideration of friction effects was of extreme importance in order to evaluate the robustness of the NCTF controller. However, the identification of friction parameters by traditional methods demands time and it is troublesome because friction parameters change according to the warm-up condition of the mechanism. Since innumerous measurements of friction parameters were required during this research, a fast method to measure the viscous and Coulomb friction values was implemented.

A.1. METHOD

The method consists in mapping the viscous and Coulomb friction of the X axis and Y axis mechanisms in relation to the displacements achieved after an open-loop step input. The mapped values are then used in a lookup table and a routine written in Matlab software is used for interpolations.

For the construction of the lookup table, the viscous and Coulomb values are identified by traditional means at different warm-up conditions of the mechanism. For each condition in which the friction parameters are identified, a step input of fixed value is applied and the final displacement is measured. The final displacements are used as the input of the lookup table and the friction values are used as the output. Once the lookup table is constructed, the routine is implemented according to the flow chart in Figure A-1.

The implemented routine has the following steps:

1. Apply an open-loop step input to the mechanism.
2. Measure the final displacement.
3. Use the final displacement as the input of the lookup table (notice that if the input value is not mapped, interpolation is used).
4. Update the model parameters with the viscous and Coulomb friction values outputted by the lookup table.
5. Use the model of the mechanism for simulations.

6. Compare the experimental and simulated data by overlapping both results in a single plot.

In the case the experimental and simulated results do not match, the mapped values need to be updated. Update may be required if the lubricant condition changes.

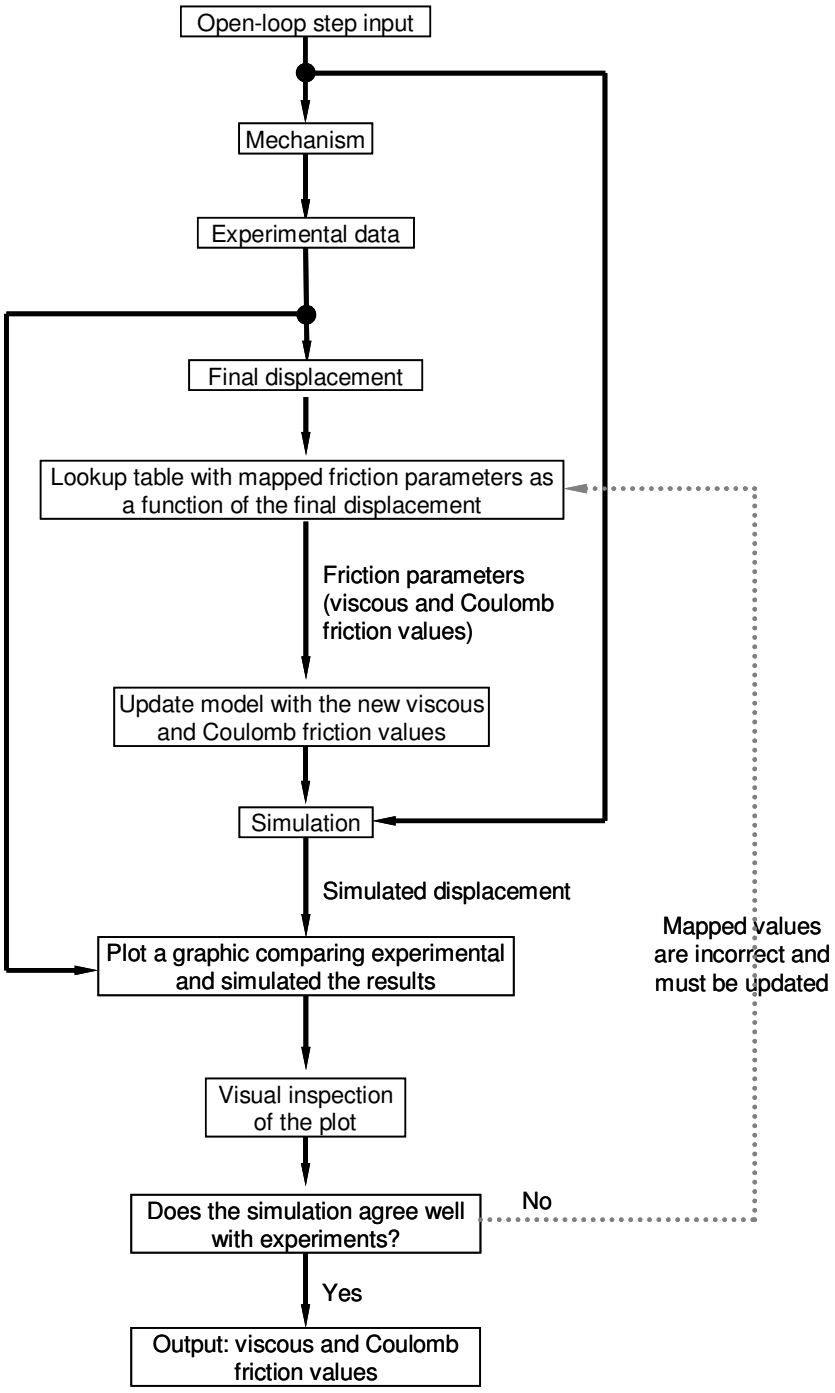

Figure A-1. Flow chart of the fast friction measurement method.

A.2. EXPERIMENTAL AND SIMULATED RESULTS

Figures A-2 and A-3 show the results from the fast friction measurement method of the X and Y axis mechanisms. Figures A-2(a) and A-3(a) are the results obtained before warm-up (the warm-up method is explained in Subsection 3.3). Figures A-2(b) and A-3(b) show the results after the warm-up. As it can be observed, the simulated results are close to the experimental ones, proving that the measured viscous and Coulomb friction values used for simulation were correctly identified.

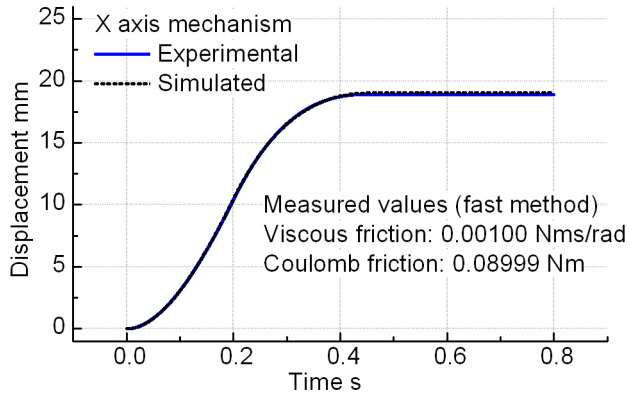

(a) X axis mechanism response before warm-up

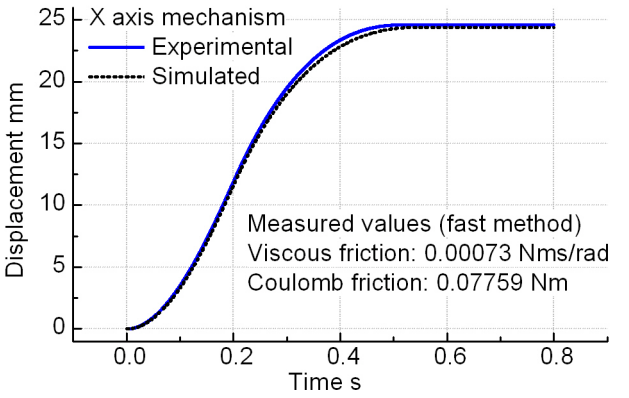

(b) X axis mechanism response after warm-up

Figure A-2. Experimental and simulated results using the X axis mechanism (simulated with the friction values measured by the fast method).

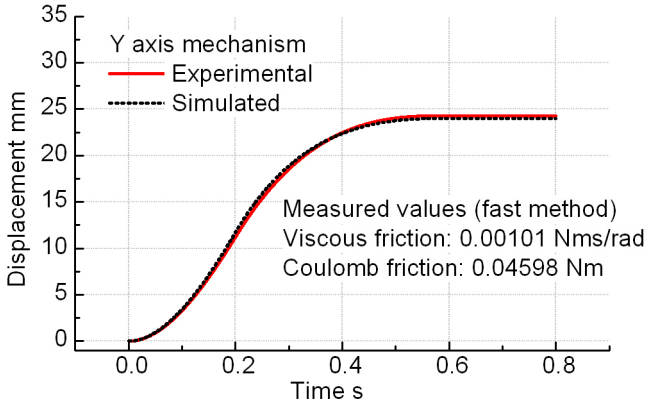

(a) Y axis mechanism response before warm-up

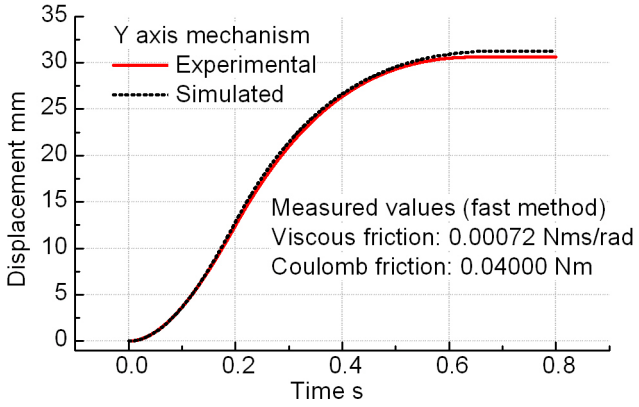

(b) Y axis mechanism response after warm-up

Figure A-3. Experimental and simulated results using the Y axis mechanism (simulated with the friction values measured by the fast method).

A.3. SOURCE CODE IMPLEMENTED IN MATLAB

```
% move to the directory where the friction measurement files are placed
wd = cd; cd C:\Mlab71\Friction_Measurement\

% Apply an open-loop step response in both axes and measure the displacement
        % Load the pre-compiled files to drive the mechanism with and open-loop step
        load(tgFriction,'friction') ;

start(tgFriction); %starts the experiment
   disp('...Wait while the frictional parameters are being updated...'); disp(' ');
```

```
   while tgFriction.Status == 'running'
   end
   disp('...Measuring the frictional characteristic and comparing the open-loop response with the model...');

clear Index            FinalPos LookUpX ViscousTableX  CoulombTableX Csdx2 Tfxmax2 Index   FinalPos
LookUpY ViscousTableY  CoulombTableY Csdy2 Tfymay2 %clear variables
disp('begin X and Y analysis'); ; disp(' ');

% Measure the final displacements
   IndexX = 0.4/DIOSampleTime;
   FinalPosX = abs (tgFriction.OutputLog(IndexX,1)); % get the position of the X axis at time 0.4 seconds
   IndexY = 0.8/DIOSampleTime;
   FinalPosY = abs (tgFriction.OutputLog(IndexY,6)); % get the position of the Y axis at time 0.8 seconds

% Look-up table with mapped frictional values

   % Last update 2006 07 14
% input X axis mechanism
   LookUpX =      [17      18.45541     18.65233137322     21.857963905     23.18826   25];
%output1
   ViscousTableX = [0.00105     0.00103      0.001          0.0008         0.00073    0.00070  ];
%output2
   CoulombTableX = [0.11        0.091        0.09           0.083          0.078      0.075]; %output1
    % Last update  2006 07 14
% input Y axis mechanism
   LookUpY =       [23          24.4867613790392   25.64780043    27.746422   29.858836     31.11692     33 ];
%output1
   ViscousTableY = [0.00104     0.001       0.00095       0.00087     0.00078       0.00070     0.00070  ];
%output2
   CoulombTableY = [0.04491    0.046        0.045         0.042         0.040         0.04        0.04   ];

% Interpolates the values and outputs the new friction parameters

   Csdx2   = interp1(LookUpX, ViscousTableX, FinalPosX, 'pcchip');
   Tfxmax2 = interp1(LookUpX, CoulombTableX, FinalPosX, 'pcchip');

   Csdy2   = interp1(LookUpY, ViscousTableY, FinalPosY, 'pcchip');
   Tfymax2 = interp1(LookUpY, CoulombTableY, FinalPosY, 'pcchip');

% Identification process finished.
% Simulating and plotting the results
disp('Frictional parameters of the X model')
```

```
if FinalPosX >= 5 % if the amplifier was off the table was not driven and frictional parameters are not
updated
   Csdx = Csdx2;
   Tfxmax = Tfxmax2;
   disp('========> X axis frictional parameters updated. Previous values erased')
else
   disp('========> X axis frictional parameters WERE NOT UPDATED. Previous parameters are being
used')
end

disp (sprintf('%s','Final Position (mm):'))
disp ( sprintf('%3.5f', FinalPosX ) ) ;
disp( sprintf('' ) )
disp (sprintf('%s','Viscous friction (Nms/rad):'))
disp ( sprintf('%3.5f', Csdx ) ) ;% disp( sprintf('\n\n' ) )
disp (sprintf('%s','Coulomb friction (Nm):'))
disp ( sprintf('%3.5f', Tfxmax ) ) ;%
disp( sprintf('\n' ) )

clear Index LookUpX ViscousTableX  CoulombTableX Csdx2 Tfxmax2

sim ('FrictionAnalyzerX_comparison.mdl') % Simulation of the dynamic model with the new friciton
parameters

% close all
        figure(444); grid on; hold on;
        subplot(2,2,1);  grid on; hold on;
        plot (tgFriction.TimeLog, -1e0*tgFriction.OutputLog(:,1), 'b', 'LineWidth', 1.5);       % position
        plot (AxisXSim.time, AxisXSim.signals.values(:,1), 'k', 'LineWidth',2);
        title('X axis Displacement. Black: Simulation')
        ylabel('Displacement mm')
        xlabel ('Time s')
        axis([0 0.8 -1 30] ); % position
        subplot(2,2,2);  grid on; hold on;
        plot (tgFriction.TimeLog, -tgFriction.OutputLog(:,2), 'b', 'LineWidth', 1.5);       % velocity
        plot (AxisXSim.time, AxisXSim.signals.values(:,2), 'k', 'LineWidth', 2) % velocity
        title('X axis Velocity., Black: Simulation')
        xlabel ('Time s')
        ylabel('Velocity mm/s'); xlabel('Time s')
        axis ([0 0.8 -10 100])
```

```
disp('Frictional parameters of the Y model')
if FinalPosY >= 5 % if the amplifier was off the table was not driven and frictional parameters are not
updated
   Csdy = Csdy2;
   Tfymax = Tfymax2;
   disp('========> Y axis frictional parameters updated. Previous values erased')
else
   disp('========> Y axis frictional parameters WERE NOT UPDATED. Previous parameters are being
used')
end

disp (sprintf('%s','Final Position (mm):'))
disp ( sprintf('%3.5f', FinalPosY ) ) ;
disp( sprintf('' ) )
disp (sprintf('%s','Viscous friction (Nms/rad):'))
disp ( sprintf('%3.5f', Csdy ) ) ;% disp( sprintf('\n\n' ) )
disp (sprintf('%s','Coulomb friction (Nm):'))
disp ( sprintf('%3.5f', Tfymax ) ) ;%
disp( sprintf('\n\n' ) )
clear Index             LookUpY ViscousTableY  CoulombTableY Csdy2 Tfymax2
sim ('FrictionAnalyzerY_comparison.mdl')
        subplot(2,2,3);  grid on; hold on;
        plot (tgFriction.TimeLog, -1e0*tgFriction.OutputLog(:,6), 'r', 'LineWidth', 1.5);       % position
        plot (AxisYSim.time, AxisYSim.signals.values(:,1), 'k', 'LineWidth',2) % position
        title('Y axis Displacement.  Black: Simulation'); axis([0 0.8 -10 40] );
        ylabel('Displacement mm'); xlabel('Time s')
        subplot(2,2,4);  grid on; hold on;
        plot (tgFriction.TimeLog, -1e0*tgFriction.OutputLog(:,7), 'r', 'LineWidth', 1.5);       % position
        plot (AxisYSim.time, AxisYSim.signals.values(:,2), 'k', 'LineWidth',2) % position
        title('Y axis Velocity. Black: Simulation');  axis([0 0.8 -10 120] );
        ylabel('Velocity mm/s'); xlabel('Time s')

clear X_Exp;
X_Exp(:,1)= tgFriction.TimeLog(1: (0.8/DIOSampleTime) );
X_Exp(:,2)= -tgFriction.OutputLog((1: (0.8/DIOSampleTime) ),1); %disp
X_Exp(:,3)= -tgFriction.OutputLog((1: (0.8/DIOSampleTime) ),2); %vel
clear X_Sim;
X_Sim(:,1)= AxisXSim.time;
X_Sim(:,2)= AxisXSim.signals.values(:,1);
X_Sim(:,3)= AxisXSim.signals.values(:,2);
save Data/X_Exp.dat X_Exp -ascii -tabs
save Data/X_Sim.dat X_Sim -ascii -tabs
```

```
clear Y_Exp;
Y_Exp(:,1)= tgFriction.TimeLog(1: (0.8/DIOSampleTime) );
Y_Exp(:,2)= -tgFriction.OutputLog( 1:(0.8/DIOSampleTime),6); %disp
Y_Exp(:,3)= -tgFriction.OutputLog( 1:(0.8/DIOSampleTime),7); %vel
clear Y_Sim;
Y_Sim(:,1)= AxisYSim.time;
Y_Sim(:,2)= AxisYSim.signals.values(:,1);
Y_Sim(:,3)= AxisYSim.signals.values(:,2);
save Data/Y_Exp.dat Y_Exp -ascii -tabs
save Data/Y_Sim.dat Y_Sim -ascii -tabs

cd(wd) % go back to initial directory



set(gcf,'position', [1 170 1024 520])

% Visual inspection of the plot
disp('Press any key to close the plots from the friction measurement')
pause
close(444);
```

REFERENCES

[1] W. T. Townsend, J. Kenneth Salisbury, The effect of coulomb friction and stiction on force control, IEEE International Conference on Robotics and Automation; 4 (1987) 883-889.

[2] B. Armstrong, Friction: experimental determination, modeling and compensation, in: Proceedings of IEEE International Conference on Robotics and Automation, Vol. 3, 1988, pp. 1422-1427.

[3] B. Armstrong, P. DuPont, C. Canudas de Wit, A survey of models, analysis tools and compensation methods for the control of machines with friction, Automatica; 30 (7) (1994) 1083-1138.

[4] C. Canudas de Wit, H. Olsson, K. J. Astrom, P. Lischinsky, A new model for control of systems with friction, IEEE Transactions on Automatic Control; 40 (3) (1995) 419-425.

[5] P. I. Ro, P. I. Hubbel, Nonlinear micro-dynamic behavior of a ball-screw driven precision slide system, Precision Engineering; 14 (4) (1992) 229-236.

[6] J. Otsuka, T. Masuda, The influence of nonlinear spring behavior of rolling elements on ultraprecision positioning control systems, Nanotechnology; 9 (1998) 85-92.

[7] J. Mao, H. Tachikawa, A. Shimokohbe, Precision positioning of a DC-motor-driven aerostatic slide system, Precision Engineering; 27 (2003) 32-41.

[8] T. Y. Lin, Y. C. Pan, C. Hsieh, Precision-limit positioning of direct drive systems with the existence of friction, Control Engineering Practice; 11 (2003) 233-244.

[9] J. Swevers, F. Al-Bender, C. G. Ganseman, T. Prajogo, An integrated friction model structure with improved presliding behavior for accurate friction compensation, IEEE Transactions on Automatic Control; 45 (4) (2000) 675-686.

[10] M. Iwasaki, T. Shibata, N. Matsui, Disturbance-observer-based nonlinear friction compensation in table drive system, IEEE/ASME Transactions on Mechatronics; 4 (1) (1999) 3-8.

[11] P. I. Ro, W. Shim, S. Jeong, Robust friction compensation for submicrometer positioning and tracking for a ball-screw-driven slide system, Precision Engineering; 24 (2000) 160-173.

[12] C. L. Chen,M. J. Jang, K. C. Lin,Modeling and high-precision control of a ball-screwdriven stage, Precision Engineering; 28 (2004) 483-495.

[13] H. Wang, D.-H. Lee, Z.-G. Lee, J.-W. Ahn, Vibration rejection scheme of servo drive system with adaptive notch filter, in: 37th IEEE Power Electronics Specialists Conference, 2006, pp. 18-22.

[14] L. Y. Pao, C. La-orpacharapan, Shaped time-optimal feedback controllers for flexible structures, Journal of Dynamic Systems, Measurement, and Control; 126 (2004) 173-186.

[15] W. J. Book, Controlled motion in an elastic world, Transactions of the ASME; 115 (1993) 252-261.

[16] P. H. Chang, J. Park, A concurrent design of input shaping technique and a robust control for high-speed/high-precision control of a chip mounter, Control Engineering Practice; 9 (2001) 1279-1285.

[17] N. C. Singer, W. P. Seering, Preshaping command inputs to reduce system vibration, ASME Journal of Dynamic Systems. Measurement, and Control; 112 (1) (1990) 76-82.

[18] J. Otsuka, Nanometer level positioning using three kinds of lead screws, Nanotechnology; 3 (1992) 29-36.

[19] J. Otsuka, S. Ichikawa, T. Masuda, K. Suzuki, Development of a small ultraprecision positioning device with 5 nm resolution, Measurement Science and Technology; 16 (2005) 2186-2192.

[20] Wahyudi, K. Sato, A. Shimokohbe, Characteristics of practical control for point-topoint (PTP) positioning systems. Effect of design parameters and actuator saturation on positioning performance, Precision Engineering; 27 (2003) 157-169.

[21] Wahyudi, A. Albagul, Performance improvement of practical control method for positioning systems in the presence of actuator saturation, in: Proceedings of the 2004 IEEE International Conference on Control Applications, Taipei, Taiwan, 2004, pp. 296-302.

[22] K. Sato, Robust and practical control for PTP positioning, in: The 1st International Conference on Positioning Technology, Hamamatsu, Japan, 2004, pp. 394-395.

[23] Wahyudi, K. Sato, A. Shimokohbe, Robustness evaluation of new practical control for PTP positioning systems, in: International Conference on Advanced Intelligent Mechatronics Proceedings, IEEE/ASME, Como, Italy, 2001, pp. 843-848.

[24] Wahyudi, Robustness evaluation of two control methods for friction compensation of PTP positioning systems, in: Proceedings of 2003 IEEE Conference on Control Applications, 2003, pp. 1454-1458.

[25] Wahyudi, K. Sato, A. Shimokohbe, Robustness evaluation of three friction compensation methods for point-to-point (PTP) systems, Robotics and Autonomous Systems; 52 (2005) 247-256.

[26] K. Sato, K. Nakamoto, A. Shimokohbe, Practical control of precision positioning mechanism with friction, Precision Engineering; 28 (2004) 426-434.

[27] K. Sato, Wahyudi, A. Shimokohbe, Practical control for two-mass positioning mechanism, in: Proceedings of the 1st Korea-Japan Conference on Positioning Technology, Taejon, Korea, 2002, pp. 206-211.

[28] Wahyudi, New practical control of PTP positioning systems, Ph.D. thesis, Tokyo Institute of Technology, 4259-G2-17 Nagatsuta, Midori-ku, Yokohama, 226-8502, Japan (March 2002).

[29] G. F. Franklin, J. D. Powell, M. L. Workman, Digital Control of Dynamic Systems, 2nd Edition, Addison Wesley, 1990.

[30] R. C. Dorf, R. H. Bishop, Modern Control Systems, 10th Edition, Prentice Hall, 2005.

[31] Y. Ihara, Contouring accuracy performance of machine tools with recent conventional numerical controller, in: Proceedings of the LEM21, Vol. 2, 2005, pp. 465-468.

ACKNOWLEDGEMENT

I would like to express my gratitude to Associate Professor Dr. Kaiji Sato, who supervised my research in his laboratory during the last three years. He not only taught me theoretical aspects of control engineering, but he also taught me *how* to use the control engineering knowledge. Being always available to teach, discuss and advice me, whenever I had problems, was fundamental for the accomplishment of this research. I am proud I was able to make part of his research group.

I am grateful to all the members of the Sato Kaiji Laboratory as well. I express my thanks to assistant professor Dr. Kazutoshi Okutsu for being always available to help me with the research matters and for his teachings about Japan and its language. I acknowledge all the students I had contact since my period as a research student, for their kindness and friendship. I specially appreciate the efforts Masahiko Nishimura did to help me whenever I had to write in Japanese. I express my thanks to Chong for sharing with me her deep knowledge in control engineering and random issues of foreigner's life in Japan. I would like to express my gratitude to the laboratory members Takeshi Saito, Takehiko Yamaguchi and Toshikazu Arima, whose help and friendship were very important during the hard times of research.

I express my gratitude to the professors of the Department of Mechano-Micro Engineering for their classes during my first year as a master student. I specially thank Professor Dr. Yukio Kosugi for his always kind attention and support.

I would like to gratefully acknowledge the Ministry of Education, Culture, Sports, Science and Technology, whose financial support during three years made possible my life and research in Japan.

Finally, I express my gratitude to my parents. They always put the education of their children as one of the most important priorities. Their kindness, affection, and love made me the person I am today. Thanks to them, I have had opportunities to stand on the shoulders of giants.